Faculdade de Engenharia da Universidade do Porto

Instituto de Ciências Biomédicas Abel Salazar

Uncovering the molecular mechanisms of Ataxin-3 interaction with nanobodies: clues to discover new approaches to treat Machado-Joseph Disease

Sofia Jorge Calvet de Magalhães Fernandes dos Santos

Dissertação realizada no âmbito do

Mestrado Integrado em Bioengenharia

Biotecnologia Molecular

Orientador: Doutora Sandra Ribeiro

Co-orientador: Doutora Alexandra Silva

04/07/2021

This MSc. research project was funded by (i) the European Regional Development Fund (ERDF) through the COMPETE 2020—Operational Programme for Competitiveness and Internationalisation (POCI), Portugal 2020, and Portuguese funds through FCT—Fundação para a Ciência e a Tecnologia (FCT/MCTES) in the framework of grants POCI-01-0145-FEDER-031173 and by (ii) the Twinning project PhasAGE (this project has received funding from European Union's Horizon 2020 research and innovation programme under grant agreement No 952334).

Abstract

Machado-Joseph disease (MJD), also known as Spinocerebellar Ataxia Type 3 (SCA3) is an autosomal dominant neurodegenerative disorder characterized by an expansion in the number of CAG repeats (coding for glutamine) within the *ATXN3* gene located on chromosome 14 (14q32.1). This gene encodes for the protein ataxin-3 (Atx3) and the expansion of the polyglutamine tract leads to Atx3 amyloid self-assembly and accumulation in specific neuronal cells with consequent neurodegeneration associated to the onset of MJD. Presently, there is still no three-dimensional (3D) structure of the full-length Atx3 which delays the development of effective MJD therapies.

Nanobodies (Nbs) are small camelid heavy-chain only antibodies that can tightly bind antigens and, among other applications, can be used as aggregation modelling agents and as protein crystallization chaperones. These features could be explored for the development of MJD treatments, seeking to modulate/inhibit the aggregation of Atx3 and, additionally, obtain its 3D structure.

The aim of this work was to a) reproduce an *in vivo* model of MJD in *Drosophila melanogaster*, b) characterize a set of new Nbs regarding their effect on Atx3 aggregation *in vitro* and c) explore Nbs as Atx3 chaperones to solve the crystal structure of the Atx3:Nb complexes.

From the proposed objectives, an *in vivo* model of MJD in *Drosophila m.* was reproduced in the laboratory, the characterization of a group of Nbs showed NB06, NB15 and NB16 significantly delay Atx3 aggregation and reduce the amount of protofibrils. Crystallization conditions for Atx3:NB02 and Atx3:NB20 complexes were optimized, but to crystals were obtained to date. The great amount of data collected during this project will be valuable for the identification of the most promising Nbs as anti-aggregation agents and neuroprotective molecules for future application in MJD therapies.

Resumo

A doença de Machado-Joseph (DMJ), também conhecida como Ataxia Espinocerebelosa Tipo 3, é uma doença neurodegenerativa autossómica dominante, caracterizada por uma expansão do número de repetições CAG (que codificam glutamina) no gene *ATXN3* localizado no cromossoma 14 (14q32). Este gene dá origem à proteína ataxina-3 (Atx3) com um domínio poli-glutamina expandido. A Atx3 expandida é propensa a agregar *in vivo*, formando espécies tóxicas e fibras semelhantes a amiloide. Ainda não se conhece integralmente a estrutura tridimensional da proteína e não há tratamentos estabelecidos para a doença.

Nanobodies (Nbs) são pequenos anticorpos apenas de cadeia pesada de camelídeos que conseguem ligar-se fortemente a antigénios e, entre outras aplicações, podem ser usados como agentes modeladores da agregação e como estabilizadores para cristalização de proteínas. Estas características poderiam ser exploradas para o desenvolvimento de tratamentos para a DMJ, procurando modelar/inibir a agregação de Atx3 e, adicionalmente, obter sua estrutura 3D.

O objetivo deste trabalho foi a) reproduzir um modelo in vivo de DMJ em *Drosophila melanogaster*, b) caracterizar um conjunto de novos Nbs quanto ao seu efeito na agregação da Atx3 *in vitro* e c) explorar Nbs como estabilizadores da Atx3, para obter cristais e resolver a estrutura cristalina dos complexos Atx3: Nb.

A partir dos objetivos propostos, um modelo in vivo de DMJ em *Drosophila m*. foi reproduzido em laboratório e a caracterização de um grupo de Nbs mostrou que o NB06, NB15 e NB16 atrasam significativamente a agregação de Atx3 e reduzem a quantidade de protofibras. As condições de cristalização para os complexos Atx3: NB02 e Atx3: NB20 foram otimizadas, mas não foram formados cristais até o momento. A grande quantidade de dados gerados durante este projeto permitirá identificar os Nbs mais promissores como agentes anti-agregação e moléculas neuroprotetoras, para futura aplicação em terapias DMJ.

Agradecimentos

Gostaria de agradecer à Doutora Sandra Ribeiro por me ter recebido no grupo de investigação que lidera com abertura e simpatia. Pela partilha de conhecimento e pela oportunidade de trabalhar com um grupo que produz e funciona num ambiente acolhedor.

Em seguida agradecer à Doutora Alexandra Silva por todo o acompanhamento e tempo disponibilizado quer a nível laboratorial, quer a nível teórico. Foram uns bons e exigentes meses que me ensinaram realmente “a fazer”. Obrigada, principalmente pelo bom e relaxado ambiente proporcionado.

Aos restantes membros do grupo, em especial à Doutora Joana Fraga pela paciência e pela introdução ao laboratório e ao grupo. Ainda por ter demonstrado o que é a eficiência em pessoa. Ao Chico e à Zsuzsa, por todas as ajudas.

Aos meus pais, por todas as oportunidades que me deram e que contribuíram para a minha formação. Pelo apoio que me dão sempre e por serem os críticos construtivos de todos os meus trabalhos. Por serem o “truque na manga” que ajuda a melhorar os resultados.

Agradecer por último à Ciência, que é das coisas mais bonitas, e à aleatoriedade que este mundo nos apresenta, mostrando-nos constantemente que estamos vivos.

Index

List of Figures

List of Tables

Abbreviations

Abs	Absorbance
APR	Aggregation-prone region
Atx3	Ataxin-3
CAG	Cytosine-adenine-guanine
CD	Circular dichroism
cDNA	Complementary DNA
CDR	Complementarity-determining region
DUBs	Deubiquitinating proteases
ELAV	Embryonic lethal abnormal visual system
GMR	Glass multiple promoter
HCAb	Heavy Chain Antibody
HD	Huntington's disease
HRP	Horseradish Peroxidase
IMAC	Immobilized metal affinity chromatography
IPTG	Isopropyl β- d-1-thiogalactopyranoside
JD	Josephin Domain
MFP	Mixed folded protein
MJD	Machado Joseph Disease
mRNA	Messenger RNA
MW	Molecular Weight
Nb	Nanobody
NES	Nuclear exporting signal
NIIs	Neuronal intranuclear inclusions
NLS	Nuclear localization signal
NMR	Nuclear Magnetic Resonance
ON	Overnight

PAGE	Polyacrylamide gel electrophoresis
PCR	Polymerase Chain Reaction
PEG	Polyethylene Glycol
PMSF	Phenylmethylsulfonyl fluoride
polyQ	Polyglutamine
RT	Room temperature
SAXS	Small Angle X-Ray Spectroscopy
SCA	Spinocerebellar Ataxias
sdAb	Single-domain antibody
SDS	Sodium dodecyl sulphate
SDS-PAGE	Sodium dodecyl sulphate polyacrylamide gel electrophoresis
SEC	Size-exclusion chromatography
SNP	Single nucleotide polymorphism
STR	Short Tandem Repeats
TEM	Transmission Electron Microscopy
ThioT	Thioflavin T
UAS	Upstream activation Sequence
Ub	Ubiquitin

Chapter 1

Introduction

1.1. Context and Motivation

Machado Joseph disease or Spinocerebellar ataxia type 3 (MJD/SCA3) is an autosomal degenerative disease. It is considered a rare disorder (0.3 to 2.0 per 100,000), but the most common type of spinocerebellar ataxia worldwide. Azores' Flores Island, in Portugal, is the place with highest incidence worldwide (1 per 239). It is characterized by progressive ataxia, chronic progressive external ophthalmoplegia (CPEO) pyramidal and extra pyramidal symptoms comprising dysarthria, dysphagia, dystonia, and distal muscular atrophies. MJD belongs to the group of polyglutamine (polyQ) diseases with an altered causative protein, ataxin-3 (Atx3), which expanded form tends to aggregate *in vivo*. There is no current cure or treatments established for MJD, but intense research is done in the field of polyQ diseases. One of these research areas is related with the use of nanobodies in modulating and inhibiting protein aggregation, something that is verified in polyQ diseases.

Nanobodies (Nbs) are small heavy-chain only antibodies able to recognize antigens with high specificity. Among multiple applications, they can be used, as mentioned, as anti-aggregation agents and as crystallization chaperones. As therapeutic agents, Nbs could slow down the aggregation process and reduce cytotoxicity in MJD and give the patient more quality years of life. Additionally, Nbs can stabilize flexible proteins facilitating crystallization to obtain 3D structures.

Several standardized *in vitro* assays have been created by the scientific community to evaluate and test therapeutic agents for neurodegenerative and polyQ diseases and uncover chaperones for crystallization. These assays can be applied to Nbs to infer their applicability as therapeutic agents and as contribute to better understand disease pathogenesis which involves knowing three dimensional structures of proteins. To study the potential of Nbs *in vivo, Drosophila melanogaster* models of MJD were already established and serve as good scaffolds to run experiments. Since they are cheap, reproduce quickly and have a short life cycle allowing fast results, flies are widely used as *in vivo* models. Other than that, multiple genetic tools have been developed making it relatively simple to produce transgenic flies with DNA of interest, in a tissue specific manner.

Specifically directed to MJD, this dissertation proposes to study the potential of Nbs as aggregation modulating agents of Atx3, to ease the crystallization of this protein to uncover its 3D structure, and establish a strong MJD *Drosophila* model to study the improvement of phenotype of MJD flies expressing Nb. By doing this, it is expected to

produce more knowledge about MJD pathogenesis and its molecular mechanisms and hopefully develop a therapeutic nanobody agent.

1.2. Objectives

As a follow-up of the work developed in the host lab, the main aim of this project was to:

1) Screen for new anti-Atx3 aggregation molecules among the available library of ataxin3-targeting nanobodies.
2) Evaluate the neuroprotective impact of nanobodies previously validated *in vitro* in a *Drosophila m.* model of MJD.
3) Use the Atx3-targeting nanobodies as crystallization chaperones of Atx3 to obtain its 3D structure.

1.3. Contributions

The main contributions of the work are:

- Characterization of a group of Nbs regarding their effect on aggregation of Atx3;
- Establishment of a MJD *Drosophila m.* model, a platform for the study of the ability of molecules, among which Nbs, to protect against degeneration and act as neuroprotective agents;
- Production of crystallizations plates with optimized conditions for the protein complexes Atx3 13Q:NB02 and Atx3 13Q:NB20.

1.4. Document Structure

The document here present is structured as follows: In Chapter Two, a theoretical presentation and summed state of the art is given for MJD, Atx3, Nanobodies, Crystallization and Drosophila m. *in vivo* model. Following, Chapter Three with present the methods utilized in the laboratory and in the last sections results and consecutive discussion are addressed.

Chapter 2

Literature Review

This Chapter encompasses an analysis of all important main subjects necessary to understand MJD disease and the developed laboratory work.

2.1. An overall look at Machado-Joseph disease (MJD):

Spinocerebellar ataxia type 3 or Machado Joseph disease (SCA3/MJD) is a rare, autosomal degenerative disease, dominantly inherited. Among Spinocerebellar Ataxias it is the most common type worldwide. From the first patients analysed, different designations for the disease were given such as nigro-spino-dentatal degeneration with nuclear ophtalmoplegia [1], autosomal dominant striatonigral degeneration [2] or Azorean disease [3]. Later it was realized that all the different reports referred to the same disease, attributing the disease's name to the first reported kindred cases (Machado and Joseph families) of Portuguese origin – Machado Joseph disease. The age of disease onset, symptoms and severity over time is variable among patients, even within members of the same family.

2.1.1. Epidemiology

Overall, SCAs are considered rare disorders (0.3 to 2.0 per 100,000) and MJD is the most frequent form of ataxia around the globe, having a mean prevalence of 1–5 per 100,000 [4][5]. Nonetheless, the geographical distribution of MJD is not homogeneous, neither globally, nor within certain countries, having a higher prevalence in Portugal, Brazil, Japan, Netherlands and mainland China. In Portugal a geographical heterogeneous distribution of the disease can be observed: 1 per 100,000 in the mainland, 1 per 1000 in "Ribatejo" [6] and 1 per 239 in the Azores Islands (Flores island) where there is the highest incidence worldwide [7].

2.1.2. Etiology

Short Tandem Repeats (STRs) are simple repetitions of DNA motifs (repeat units ranging from 2 to 7 base pairs in length), microsatellites that occur at different and multiple locations within the human genome. These regions have a high mutation rate and a lot of genetic diversity is seen within humans. As for MJD, the causative gene has a STR of three nucleotides (CAG - cytosine-adenine-guanine), coding for glutamine (Q). A cDNA library screening of the human brain revealed genes with CAG repeats, among which the originally designated *MJD1a*, responsible for MJD. In fact, in MJD patients, an expansion of the number of CAG repeats in the ATXN3 gene, located at the long arm of the chromosome 14 (14q32.1) was observed [8]. ATXN3 contains a region with CAG repeats, which repeat-number varies within normal

individuals (12-44) and is expanded (60-87) in case of individuals with the disease [9][10]. Alleles of intermediate size have also been reported, although they are not very common [11]–[13]. These repeats are present in the coding region of the mRNA, giving rise to the ataxin-3 protein (Atx3) with a polyglutamine (polyQ) tract. The expanded Atx3 forms neuronal intranuclear inclusions resulting in neuronal degeneration and dysfunction.

2.1.3. Machado Joseph disease as a polyglutamine disease

MJD belongs to the group of diseases arising from polyglutamine repeat expansions. One would be familiar with other diseases belonging to the group: Huntington's disease (HD), spinocerebellar ataxias type 1, 2, 6, 7 and 17, spinal and bulbar muscular atrophy and dentatorubral-pallidoluysian atrophy [14]–[20]. All these diseases contain an unstable glutamine expansion in the coding region of their corresponding causative genes. The proteins involved share this polyglutamine tract, but have no homology outside it [21]. As explained, MJD develops from a mutation in the gene ATXN3 and although the genetic cause for the disease is well mapped, it is a heterogeneous disease with underlying complex pathogenic mechanisms that are yet unknown and scarcely described. This also happens for the other polyQ diseases as well. While the different corresponding proteins share a polyQ tract, they have different properties inside the organism: different structure, size, function, protein partners, subcellular localization and activity. This suggests that other factors may play a role in disease progression, pathogenesis and manifestation, making it hard to establish parallel treatments [22], [23]. Different parts of the brain are affected in the different diseases and although some symptoms are common, there are differences in disease manifestation [23]–[25]. Overall, these diseases are of late onset and progress over the course of 15 to 20 years leading to death. The relationship between the length of the polyQ and the age of onset of the disease is not linear but there is evidence that longer stretches correlate with earlier age of onset [23].

2.1.4. Clinical presentation and Anatomopathology

Patients with MJD have heterogeneous phenotypes even when sharing similar polyQ repeat-sizes. Modifier factors contribute to this heterogeneity: patient's gender, genetic background, duration of the disease and factors of molecular nature (protein interactors, cellular environment, modifying genes, gene polymorphisms [26], among others) [27], [28]. Main clinical presentations are progressive ataxia (lack of muscle control) and chronic progressive external ophthalmoplegia - CPEO (gradual loss of ability to move eyes and eyebrows), pyramidal and extra pyramidal signs comprising dysarthria (motor speech disorder), dysphagia (swallowing difficulties), peripheral neuropathy (damage to peripheral nerves) dystonia with rigidity (muscles contract uncontrollably) and distal muscular atrophies [29]. The mean age of onset is around 40 years (with reported extremes of 4 and 70 years) and the survival expectancy of about 21 years (ranging from 7 to 29 years) after disease onset [30]–[32]. Gait ataxia is the most reported first symptom. At an advanced stage, the patient is usually wheelchair bound and has severe speech disorder and trouble swallowing, needing

nursing. Since this disease is highly pleomorphic in terms of age onset and severity of the symptoms, an effort was done to establish different types of the disease (Type I, II and III) so it would be simpler to diagnose and categorize patients (Table 1). Patients homozygous for ATXN3 mutant alleles have earlier age-of-onset and more severe phenotypes than heterozygous patients. As mentioned, a relationship between the size of the Atx3 polyQ tract and the onset of the disease exists and longer polyQ expansions result in earlier onset and a more severe clinical presentation.

Table 1 *- Classification of the different MJD types: type I, type II and type III and corresponding age of onset and symptoms.*

	Age of onset	**Symptoms**
Type I	10-30 years	Limb and gait ataxia, severe dystonia, pyramidal signs, progressive external ophthalmoplegia (PEO) and a relatively faster progression of symptoms.
Type II	20-50 years	Symptoms similar to type I but slower disease progression. Cerebellar ataxia associated with peripheral alterations.
Type III	40-70 years	Loss of muscle mass (amyotrophy) due to inflammation and peripheral neuropathy. Slowly progressive parkinsonism, inability to coordinate movement. The progression is the slowest of the three types

The Atx3 mutant protein is expressed ubiquitously throughout the body, but specific populations of neurons are vulnerable and eventually die [33], [34]. In fact, different regions of the brain and spinal cord are affected in MJD, but the disease is generally characterized by neuronal loss. The substantia nigra and the dentate nucleus of the cerebellum are the main affected areas accounting for the Parkinsonian and ataxic symptoms. Neuronal loss is also present at the dentate nucleus. Brain stem damage in motor nuclei (cluster of neurons) leads to disturbance in ocular motility and weakness of the tongue. Atrophy of the basis pontis can happen and intranuclear inclusion bodies are found in the pontine grey nuclei. Defects of basal ganglia, thalamus, spinal cord, dorsal root ganglia, and sensory peripheral nerves are more variable. The spinal cord has total or subtotal neuronal loss in the dorsal nuclei, variable degeneration of the long tracts and dorsal root ganglia show neuronal destruction, proliferation of satellite cells, and residual nodules (Figure 1). Peripheral phenotypes might indeed result from direct influence of the Atx3 mutant protein in the peripheral tissues [35].

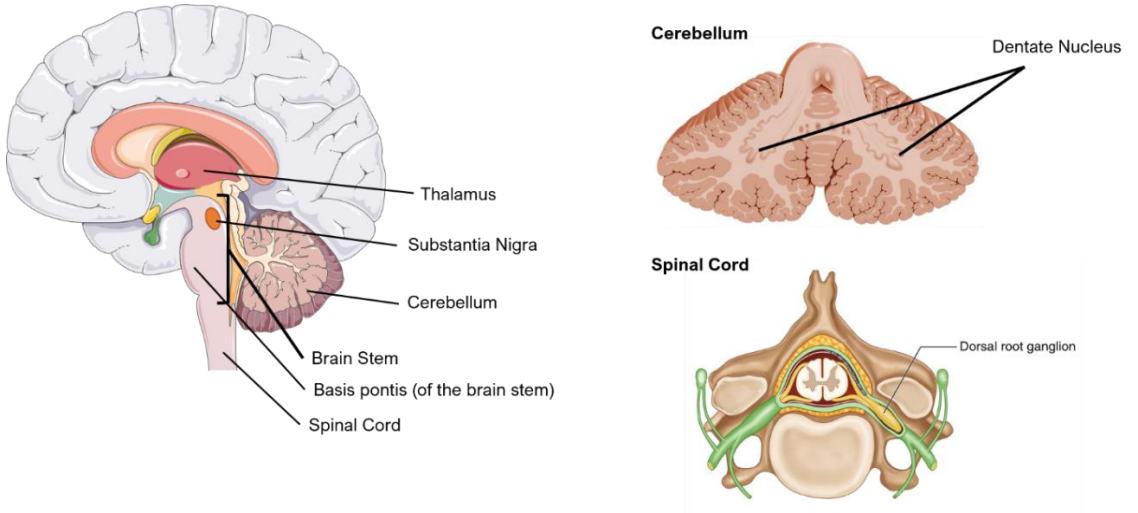

Figure 1 *- Anatomic representation of the brain stem and its basis pontis, the spinal cord, the dentate nucleus of the cerebellum and the dorsal root ganglion, important structures related with MJD anatomopathology.*

2.2. Ataxin-3

Ataxin-3 (Atx3) is a 42kDa protein that contains a globular N-terminal Josephin domain [36], highly conserved among species, and a flexible C-terminal tail containing two ubiquitin-interacting motifs (UIMs) followed by the polyQ tract (Figure 2). However, depending on the splice variant of the mRNA transcript, a third UIM can be found downstream the polyQ tract [37] (Figure 2). This 3UIM variant is the most common isoform of Atx3 found in the human brain and also in intranuclear neuronal aggregates, with 361 amino acids (UniProt P54252) [38].

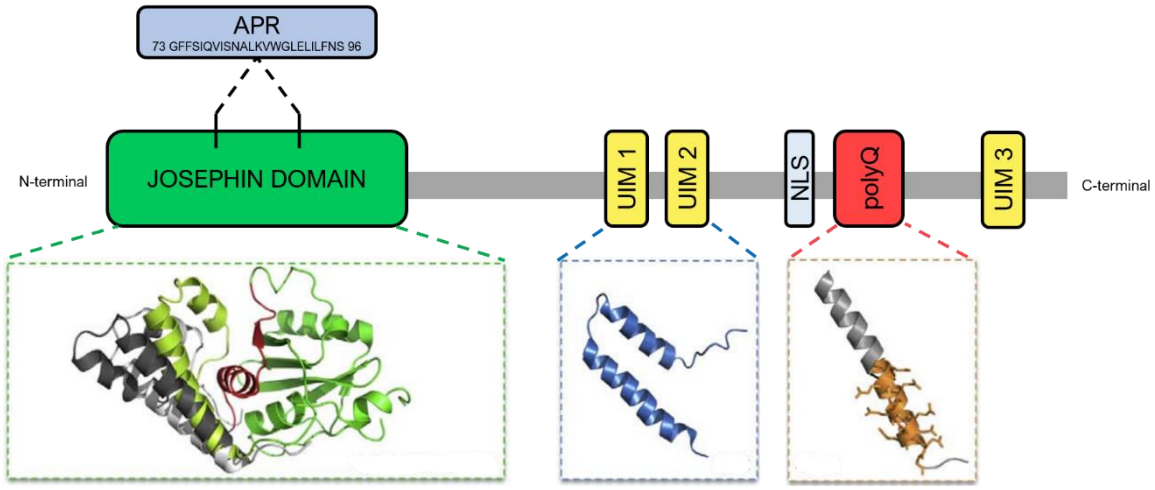

Figure 2 *- Schematic representation of Atx3 and 3D characterized structures of known domains. In green is the Josephin domain structure and in blue the UIM1 and 2 structure when bound to ubiquitin, the linker is between both helical structures and the polyQ tract. Adapted from* [21] *with permission.*

Solving the 3D structure of the full-length Atx3 protein has been a challenge. It is very difficult to obtain ordered crystals of the full-length protein so the structure can be solved by crystallography. Nonetheless the structure of isolated Atx3 domains has been solved by crystallography and other alternative techniques, namely Nuclear

Magnetic Resonance (NMR) and cryo-Electron Microscopy, but with inherent technical limitations, starting from the fact that Atx3 is a mixed folded protein (MFP) with both globular and intrinsically disordered regions, prone to aggregate, making it difficult for both crystallization and acquisition of NMR data sets [39]. The solution structure of the Josephin Domain has been structurally characterized by NMR showing it has a papain-like fold with mainly two subdomains: a globular C-terminal β-sheet catalytic subdomain and a N-terminal α-helical subdomain with a hairpin [36]. The C-terminus region of Atx3 has features of an intrinsically unfolded or partially structured system, but also regions with strong helical propensity. The latter happens within the three UIMs (residues 224–240, 244-263, and 331–348). The three UIMs are α-helical structures, characterized by NMR [39]. UIM1 and UIM2 are separated by a short flexible linker and this unit (UIM1 and 2) binds to ubiquitin (Ub) [40]. A region preceding the polyQ tract (residues 278–289) also exhibits high helical conformation in solution [39]; Small Angle X-Ray Spectroscopy (SAXS) can aid as a complementary technique while the full 3D structure of Atx3 is not determined, providing a low-resolution insight into the molecule's architecture [41]. Low-resolution molecular envelopes have been presented for both normal [42] and expanded Atx3 [43].

Atx3 in neurons is found mainly in the cytoplasm, but the expanded form tends to be in the nucleus. The subcellular localization of Atx3 appears to be regulated by different regions in its structure: a presumed nuclear localization signal (NLS) (residues 282–285) upstream the polyQ tract and two nuclear-exporting signals (NES) (residues 77–99 and 141–158) located within the JD [44]–[47]. Investigating localization signals in Atx3 is important to unveil the molecular mechanisms responsible for Atx3' intracellular localization and distribution, giving insight on pathogenesis.

In terms of function, Atx3 has been found to act within different pathways and plays an important role in many cellular processes. It is yet still unknown the reason for the disease's pathogenesis, whether it comes from a gain of toxic function or from a loss of normal function. What is observed is that many pathways are deregulated in the disease's scenario. Atx3 belongs to the family of deubiquitinating proteases (DUBs) that cleave ubiquitin from proteins, in this case, preferably polyubiquitin chains of at least four subunits [48], [49]. Ubiquitin regulates protein degradation via the proteosome and the lysosome, helps proteins to be localized intracellularly, activates and inactivates proteins and participates in protein-protein interactions. Consequently, DUBs are able to control all of these processes by cleaving the peptide or isopeptide bond between ubiquitin and its ligand [50]. Interestingly, normal Atx3 has a role of protecting the cell against the harmful effects of polyQ proteins and other neurodegenerative-disease-associated proteins [51]. With advances in research, new interacting partners are being constantly described for Atx3, allowing to understand what roles this protein plays within the cell and what pathways could be affected in a disease scenario [42], [52]–[55].

2.2.1. Aggregation

The aggregation pathway for Atx3 is not yet fully understood, however, different descriptions have been presented, some more accepted than others [56]–[60]. Both normal and expanded Atx3 have the inherent propensity to aggregate *in* vitro, mediated by an aggregation-prone region (APR) within the core of the globular Josephin Domain (JD) and independently of the polyQ length, forming sodium dodecyl sulphate (SDS)-soluble aggregates. The difference is that the expansion of the polyQ region leads to a second step in the aggregation process with the formation of long SDS-insoluble mature fibrils [57]. *In* vitro studies also showed the ability of the JD alone to form amyloid-like aggregates and the influence of the different protein domains on the aggregation kinetics, indicating that the polyQ tract is not the only responsible for Atx3 aggregation and toxicity [61]–[63]. Although the polyQ length influences the kinetics of the self-assembly process, the Atx3 aggregation process in a generalized manner is similar to what happens with other polyQ proteins [21], [56], [57], [59], [60], [64]: starting from monomers (Figure 3A) a conformationally altered monomer or dimer is formed (Figure 3B) and acts as nucleation spot for the addition of monomers; oligomers of higher molecular weight appear (Figure 3D) that continue to elongate into protofibrils (Figure 3E). From there on, expanded Atx3 undergoes further changes involving hydrogen bonding among side-chains in the polyQ region resulting in the appearance of amyloid-like mature fibrils [65] (Figure 3F).

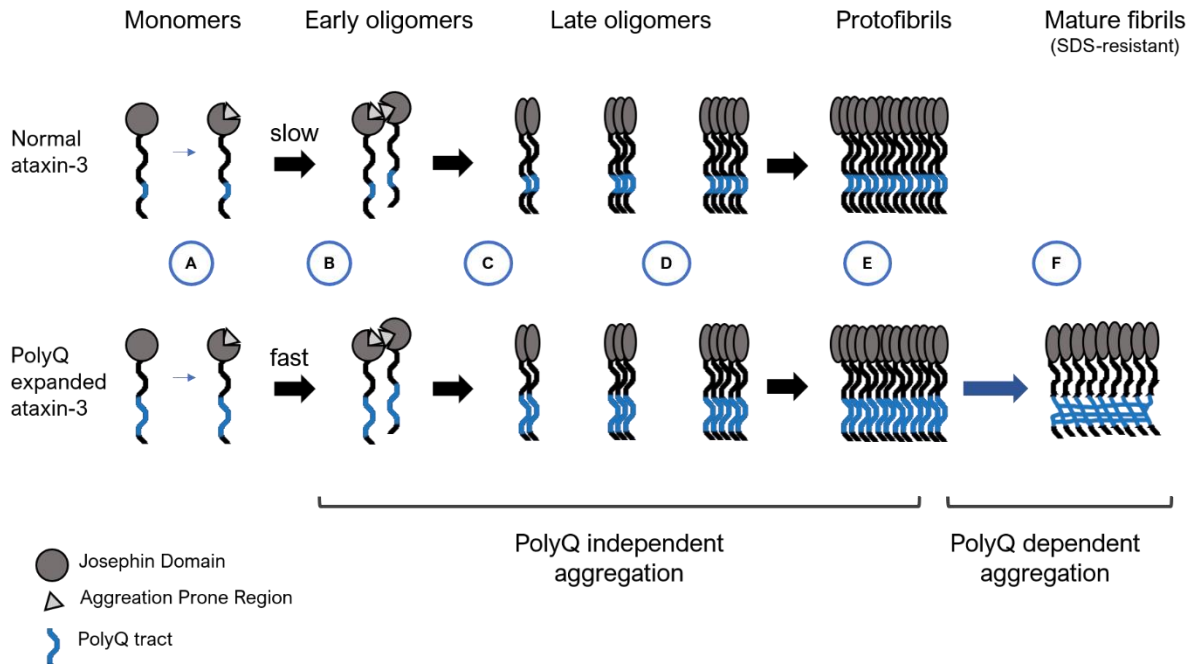

***Figure 3** - Atx3 aggregation steps. Difference in aggregation process between normal and expanded Atx3 where in the latter an additional step occurs with the establishment of mature amyloid-like fibrils, in a polyQ dependent manner.*

Formation of amyloid aggregates is routinely assessed by Thioflavin-T (Thio-T) fluorescence analysis, circular dichroism (CD) spectra, TEM and resistance to SDS. Amyloid fibril - β-rich structures - formation correlates with a shift of secondary structure from α-helix to β-sheet, a phenomenon that is observed in different polyQ

neurodegenerative diseases, suggestive of conversion to amyloid-like structures [43]; CD (circular dichroism) spectra show that truncated N-terminal (containing the JD) and normal Atx3 undergo an increase in β-sheet content and decrease in α-helix over the course of aggregation [57].

Thio-T fluorescence increases upon binding to β-rich structures. Thio-T assays have shown that formation of ThioT-positive species occurs faster in the expanded form of Atx3 when compared to non-expanded and truncated N-terminal forms [56], [57]. Further studies combining mass spectrometry and limited proteolysis propose that the difference in the first steps of aggregation results from an altered conformational dynamics that enhances the exposure of an aggregation prone region (residues 73-96) in the JD, possibly induced by long-range effects of the longer polyQ tail [59], [66], [67]. The tail may hold JD in an aggregation-prone conformation for longer periods of time, increasing the chance of non-native intermolecular interactions or it can provide an environment that lowers the energy barrier for the adoption of an aggregation-prone conformation all leading to a faster process of aggregation, when compared with normal Atx3 [59].

2.2.2. Factors leading to disease

The pathogenic mechanisms of expanded polyQ Atx3, whether the protein leads to a toxic gain of function [68], to a loss of normal function or both, are not fully understood [69]. Why neurons are specifically affected when Atx3 is expressed ubiquitously is not yet fully understood, but neurons may be more sensitive to misfolded proteins and aggregates, abnormal protein interactions, and other molecular features can be responsible or contribute for this neuronal specificity (interaction with vital transcription factors) [70], [71]. It is well established that expanded Atx3 aggregates as neuronal intranuclear inclusions (NIIs) and was initially hypothesized that inclusions could mediate neurodegeneration. NIIs are found across many polyQ diseases as a neuropathological hallmark. The pathological role of these NIIs however is still unclear even if there is any. Some studies point that the formation of NIIs can simply be a neuronal response to barrier abnormal proteins into a non-toxic structure [72], [73]. There has been a growing stand that supports that the toxic species in polyQ diseases are soluble oligomers and intermediate forms of aggregation rather that the amyloid-like fibrils [74]–[77]. However, since the longer polyglutamine tracts are linked with a faster disease progression, higher severity of symptoms and decrease in age of disease onset, it is hard to deny that expanded polyQ tracts lay behind disease pathogenesis.

Nowadays it is accepted that for any given polyQ disease, many mechanisms and neurotoxic species should contribute to neuronal dysfunction and cell death rather that one single entity being responsible for pathogenesis [71]. Possibilities are:

- Disfunction of alternative splicing - alternative splicing disfunction has been raised as a possible cause for certain diseases [78]–[80]. Alternative splicing and single nucleotide polymorphisms (SNPs) are responsible for the

presence of at least three isoforms of Atx3 in the human organism, termed Atx3c, Atx3aL and Atx3aS [37].

- Fragments containing the polyQ tract - the proteolytic cleavage of mutant Atx3 generates smaller soluble fragments containing the polyQ tract that seem to be highly cytotoxic and aggregation-prone [81]–[84]. Several *in vivo* and *in vitro* observations conclude these fragments are more toxic and more susceptible to aggregation than full-length Atx3 [85]–[88].

- Deleterious protein interactions - the expanded polyQ proteins may adopt a misfolded conformation or aggregate into a structure forming a substrate for abnormal protein interactions, where the resulting protein complexes whether gain new functions or interfere with native functions, can contribute to pathogenesis [71], [89], [90].

- RNA toxicity - studies in *Drosophila m.* showed short RNAs, microRNAs and RNA containing polyQ information to be toxic and to induce neuronal dysfunction and progressive degeneration. Additionally, neurons were found to be selectively sensitive to RNA toxicity [69], [91], [92].

- Mitochondrial disfunction - mitochondrial disfunction can result from higher levels of free-radicals and oxidative species, a scenario that is verified in polyQ diseases coming from a reduced level of anti-oxidant enzymes [93]. Mitochondrial DNA damage was also verified in MJD transgenic mice [94]. An impaired mitochondria has its activity compromised being unable to scavenge free radicals also contributing to an increase in oxidative stress in the cell. In turn, oxidative stress hampers the normal cellular functions potentially leading to neuronal death. Mitochondrial dysfunction could then play a role in the pathogenesis of MJD [95], [96].

2.3. Nanobodies

Let us take off from a figure illustrating the conventional structural features of a mammalian IgG antibody (Figure 4). Immunoglobulins are “Y” shaped proteins, composed of two-copies of a heavy-chain and two-copies of a light-chain. Each heavy-chain (H) has four domains, whilst the light-chains (L) have two domains (this is true for IgG, IgA and IgD; five domains are present in the H-chains of IgM and IgE – being these the different classes of immunoglobulins). Both N-terminal domains of H and L chains (VH and VL, respectively) are variable – the variable fragment (Fv) of an antibody. These are the portions of the protein that constitute the paratope which specifically binds to the epitope on an antigen [97].

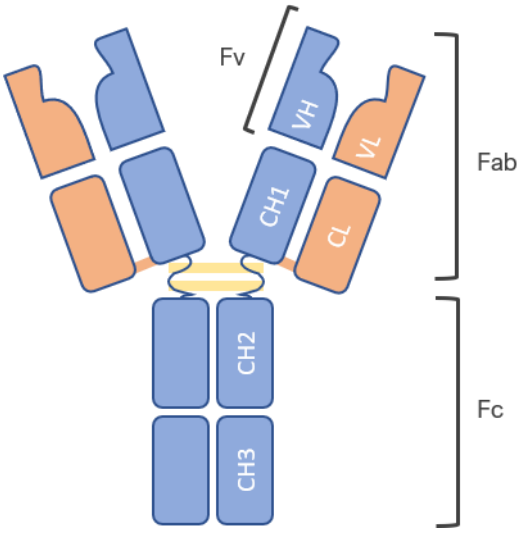

Figure 4 *- Schematics of a conventional antibody (IgG1) composed of two heavy (H) chains (composed of the VH, CH1, hinge, and CH2 and CH3 domains) and two light (L) chains (the VL and CL domains).*

2.3.1. Heavy-Chain Antibodies in Sera of Camelids

It was found that in animals belonging to the family Camelidae, in addition to the conventional IgG antibodies, there were other interesting entities, heavy-chain only antibodies (HCAbs) (Figure 5A). This family comprises camels (one-humped *Camelus dromedarius* and two-humped *Camelus bactrianus*), llama (*Lama glama* and *Lama guanicoe*), and vicugna (*Vicugna vicugna* and *Vicugna pacos*) [97], [98].

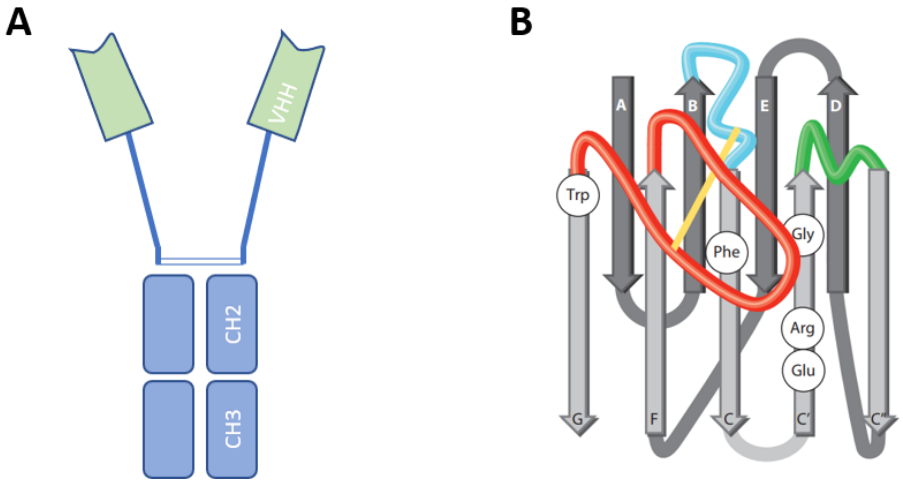

Figure 5 *– Schematic representation of a HCAb and the secondary structure of a VHH domain* ***(A)*** *HCAbs contain only H chains; each H chain contains a VHH, hinge, and CH2 and CH3 domains. Different subtypes of HCAbs happen, with different hinge lengths.* ***(B)*** *Secondary structure of the VHH domain. A, B, E, and D are the β-strands of one sheet in the back and the G, F, C, C', and C'' strands are in the front sheet. Complementarity-determining region 1 (CDR1) in blue, CDR2 in green and CDR3 loop in red.*

HCAbs are homodimeric proteins lacking the L-chain and devoid of the first constant domain (CH1). The N-terminal heavy domain, VHH, is a variable domain responsible for cognising the antigen. One can say that VHH is the structural and functional correspondent to the Fab (antigen binding) portion of the conventional antibody. It is the VHH that is referred to as a nanobody (Nb) or single-domain antibody

(sdAb). Nanobodies are smaller than antibodies (molecular weight of 12-15 kDa rather than 150 – 160 kDa) [99] and more compact, making them stealthier and able to reach targets in poorly accessible tissues. The folded VHH comprises nine β-strands (A,B, C, C', C'', D, E, F and G) (Figure 5B) arranged as a four-stranded β-sheet (A, B, D and E) and a five-stranded β-sheet (C, C', C'', F and G) linked by loops and a conserved disulfide bond (Figure 5B - shown in yellow) [97]. The nanobody recognizes the antigen by the three hypervariable loops (H1-H3) instead of six as in the Fab of a conventional antibody (Figure 5B). H1 to H3 are the loops that connect the B-C, C'-C'' and F-G strands, respectively making this the complementarity-determining region (CDR) [100]. For a good accommodation of the antigen the loops in nanobodies are naturally longer than in antibodies [101]. In camel VHHs, the flexibility generated from these longer loops is constrained with a disulfide bond – interloop disulfide bond – in the absence of the antigen [102]. The paratope of a nanobody is normally convex, advantageous to interact with cavities of antigens, but can also adopt a flat surface or even be concave.

2.3.2. Generation of antigen-specific nanobodies

Nanobody banks can be generated by three ways: immune, naïve, and synthetic. An immune library consists in the immunization of a young camelid adult (commonly a camel, dromedary, llama or alpaca) done by, over the course of ~2 months, injecting the animal four to eight times with the relevant antigen along with a standard adjuvant (an average cocktail of 10 proteins and also DNA can be administered)[103]–[105]. The amount of immunogen administered depends on the molecular weight (MW) of the molecule but also the toxicity/immunogenicity. Usually more than one animal is immunized such that in the end one can choose the best corresponding Nb to the epitope of interest from a higher diversity pool, since no two animals have the exact same immune response. 50-100mL of blood are harvested from the animal to prepare lymphocytes (~10^7 cells in the sample) and extract the mRNA (messenger RNA) which is then converted into complementary DNA (cDNA). From cDNA, amplification of the VHH gene regions is done by Polymerase Chain Reaction (PCR). This amplification can be done in two ways: one-step PCR based on the uniqueness of the sequence of the hinge in VHHs **(**Figure 6A**)** or a nested PCR procedure **(**Figure 6B**)**. The hinge region of HCAbs has the most sequence differences among IgG isotypes. For nested PCR, comprising the use of two sets of primers, the first set uses a primer that anneals to a conserved region of all constant γ genes and another that binds to the leader sequence signal of VH and VHH exons – the H chain of IgGs is amplified from the leader sequence to a conserved region in the CH2 exon leading to two PCR products that differ in length: "VH-CH1-hinge" (~900bp) for conventional IgG and "VHH-hinge" for HCAbs (~600bp). The smaller product is standardly purified after agarose gel electrophoresis yielding the cDNA template for the second PCR. Nested primers are then used to amplify the VHH region and include restriction enzyme sites for cloning reasons [106], [107]. Selection protocols are employed to retrieve antigen-specific Nbs either by panning or direct colony screening; a variety of techniques have been established but the most common is phage-display [108], [109].

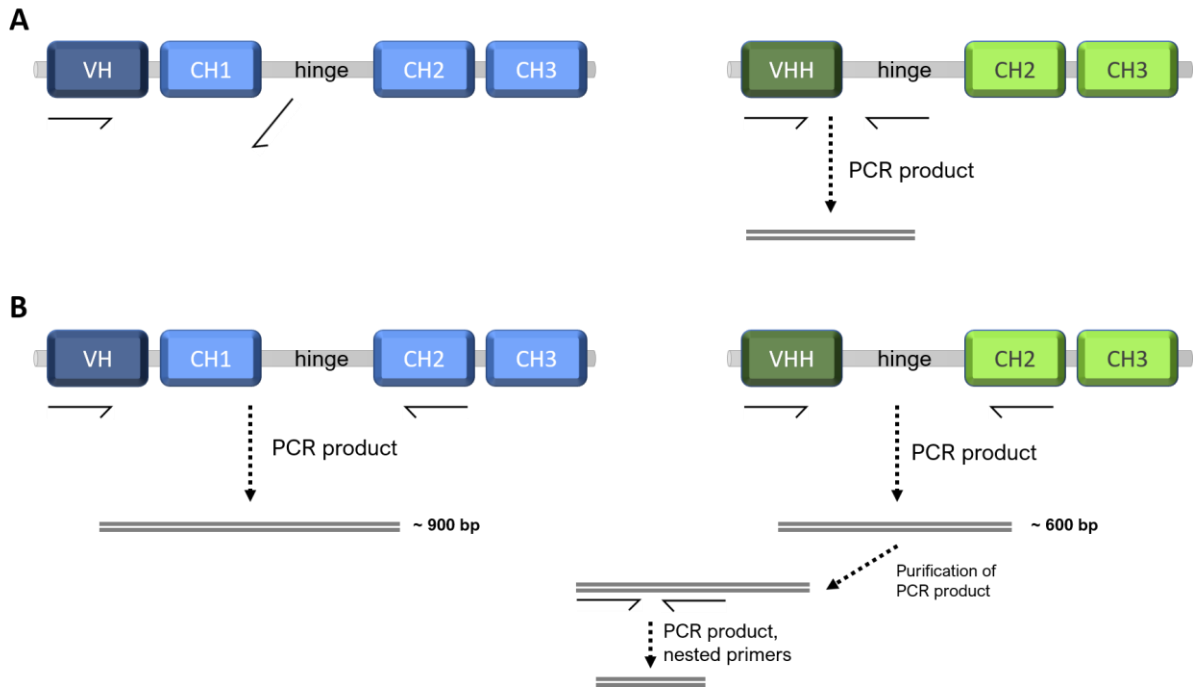

***Figure 6** - Amplification procedures to clone the VHHs from immunized animals. (A) one-step PCR procedure (B) nested PCR with purification of PCR product after agarose gel electrophoresis.*

Besides the ethics behind purposely injecting an animal with immunogens, some antigens might not elicit an HCAb response or be too harmful and toxic for the animal. In those cases, other strategies are sought: naïve libraries [110], [111] – build out of non-immunized animals – and synthetic libraries [112] – made from synthesized DNA constructs.

2.3.3. Expression and purification of recombinant nanobodies

Nanobodies can be expressed in a variety of microorganisms, including plants [113]–[116]. Using bacteria as expression systems is very common if the aim is to produce milligram quantities of nanobodies for different studies. The DNA vector containing the Nb sequence also holds a promoter that is sensible to IPTG, inducing a targeted and enhanced expression of the Nb. The yield of expression per liter of culture is very satisfactory (5 to 10 mg per liter). In addition, the Nb is cloned after a secretion signal such that it ends up in the periplasmic portion of the cell. Upon osmatic shock, which forces the proteins in the periplasmic region to be extracted and remain soluble, the protein extract is far less contaminated than observed for proteins expressed in the cytoplasm. The insertion of a C-terminal 6-Histidine tag to the Nb will allow it to be easily purified through immobilized metal affinity chromatography (IMAC) proceeded by size exclusion chromatography to separate and store the monomeric Nb. If the histidine tag is not ideal to have in the Nb, depending on the application, purification by ligation to protein A or a wide range of other proteins can be utilized to successfully separate the Nbs [117], [118].

2.3.4. Biochemical and biophysical properties of nanobodies

Nanobodies are small (~15kDa), highly stable proteins, they have a long shelf-life period allowing scientists to carry out assays throughout a long period of time. They have been successfully stored at -4°C, -20°C, -80°C (stable for months) or even at 37°C (stable for weeks) while maintaining antigen-binding capability [119]. They are quite resistant to thermal and chemical denaturation, denaturing temperatures ranging ~60-80°C [120]. Tunning the Nb sequence, leading to the formation of an additional dissulfide-bond renders the Nbs resistant to oral administration and panning phage-display libraries under harsh conditions has also allowed to find Nbs resistant to other denaturing conditions, such high urea concentrations [120]–[123]. Upon purification, Nbs can be stored in a monomeric state, remaining stable in solution even at concentrations of 10mg/mL [124]. These molecules do show some weaknesses having a short blood half-life and rapidly being cleared by the kidneys which might be a place where they would accumulate and possibly be toxic. When designing a strategy to tune the nanobody as a therapeutic agent, it must be taken into account that it must achievethe desired target in sufficient amount to exert a positive effect. Overall, Nbs are well expressed in bacterial systems, are soluble and stable in different conditions, show high affinity to its corresponding antigen and can reach epitopes that conventional antibodies might not have been able to.

2.3.5. Improving nanobody characteristics

Although several properties of nanobodies are well characterized, such as solubility, affinity and stability, a good model of the disease in study should be developed at the cellular level to present the nanobody with the closest possible scenario it would encounter in a diseased individual. These models are important templates to cyclically tune and perfect the nanobody [125]–[127]. Binding kinetics of the nanobodies to their targets is controllable, on and off rates are subject to manipulation by engineering the nanobody to achieve the desired therapeutic function [128]. Fusing a nanobody to another, designed against albumin, has shown to increase blood half-life up to 10 days [129]. Other strategies have fused Fc human fragments to introduce the ability to bind specific receptors inside the host and lead the complex to targeted sites or even allow interaction and activation of specific cellular populations [130], [131].

2.3.6. Nanobody applications

Several research fields, namely in neurodegenerative diseases, are exploring the potential of Nbs as intracellular signalling molecules, disease biomarkers, helpers to understand protein-protein interactions, inactivators, diagnostic tools, crystallization chaperones and therapeutic agents, such as anti-aggregation agents [128], [132]–[139]. Our focus should remain on the last two cases.

In terms of therapeutics, therapeutic proteins are emerging as a new class of drugs, recently approved by the Food and Drug Administration (FDA). Among these are antibodies which have been widely used in research and some already approved and commercialized treatments rely on these molecules. Antibodies are subject of great

investment and research in the field of neurodegenerative diseases [140], [141]. Already commercialized antibody exists for Alzheimer's disease (Aducanumab, BIIB037 – Biogen). Nonetheless, antibodies have certain limitations among which their larger size which might prevent them from accessing essential epitopes and sites inside the organism. That is where nanobodies come in play. The small size of nanobodies allows them to reach targets in less vascularized and poorly accessible tissues [142], [143]. Specifically addressing neurodegenerative disorders and polyQ diseases, nanobodies instinctively seem promising, knowing they act as intrabodies and protein accumulation occurs intracellularly. Targeting the initial misfolding of the causative polyQ proteins could show effects of disease management, slowing down the onset of disease and alleviating symptoms. It is proposed that Nbs could act by impeding nuclear localization of these pathological proteins, turning over settled fibrils or preventing unwanted interactions with abnormal protein partners [128], [144], [145]. From studies on Huntington's Disease (HD) and the polyQ protein huntingtin (HTT) it was recognized that some nanobodies designed to bind the polyQ region of this protein may not be ideal and could increase the size of the aggregates and possibly toxicity [146], [147]. As of that, designing Nbs to other regions and domains (the polyP flanking region for huntingtin [146]) of this group of proteins could be another interesting approach. To date, some Nb-based therapeutics have passed phase-I or phase-II tests [97]. Regarding MJD, Nbs could act as Atx3 aggregation modulators. Slowing down the aggregation process and reducing cytotoxicity and giving the patient more quality years of life starts by posing the first function of Nbs as therapeutic agents. It would be ideal to have a regression of phenotype by dissociating established mature fibrils, however, it is more likely that by dissociating the mature fibrils, all those assembled intracellular molecules would be very toxic. Nbs could help stabilize the disease, stopping or decreasing the formation of aggregates and act as a preventive treatment specifically for individuals who bear the mutation but have not developed symptoms yet.

As crystallization chaperones, their use aims to aid challenging proteins (concept will be explained below) to crystalize ultimately resulting in diffracting crystals of protein:Nb complexes. Nanobodies are substituting antibody fragments (Fabs, Fvs, scFvs) that were hampered by their bigger size and heterodimeric constitution. Nanobodies have the molecular features optimal to provide a good scaffold for crystal development. It is possible that the presence of additional β-strands is induced by the nanobody's interaction with the molecule of interest increasing the organization of the complex [132], [148]–[151].

2.4. Crystallization

Crystallization is the process of atoms or molecules arranging into an ordered, well-defined, crystal lattice, to find a minimum energetic state. Protein crystals have been around from quite some time now, being the first recorded those of haemoglobin, around 1840. It was only in the 1910s that protein crystals were found to diffract X-ray

beams [152]. From there, X-Ray crystallography was developed aiming to solve protein 3D structures [153]. The crystallization process itself, although being very simple in theory, has multiple variables that play a role in determining the generation of well-ordered crystals, critical for determination of 3D structures by X-ray crystallography. When trying to find conditions that lead to crystal formation, one can either find clear drops, the formation of other insoluble species rather than crystals (precipitates or liquid/oil like species). That being, optimization of crystal conditions is for sure the most time-consuming part of the process. Nowadays, a researcher might choose from commercial crystallization kits that are ready to use and are useful for a fast screening of a wide range of crystallization conditions.

Crystallization is a phenomenon of phase-transition starting from nucleation followed by growth. The goal is to lead the protein solution to supersaturation, create conditions to exceed its solubility limit, resulting in the formation of crystals which can be represented in a phase diagram (Figure 7). To design a phase diagram the solubility curve for a globular protein needs to be measured experimentally [154]. From literature it can be summarized that the solubility is measured by placing protein crystals in a protein-free solution (with the conditions at study), mixing and measuring the concentration while the crystal melts away gradually overtime and finding out at which concentration an equilibrium is reached. Of course, if you are trying to form crystals for a protein that you have not yet succeeded, solubility cannot be measured in this way. On the contrary, it can be measured by the supersaturation of a solution upon the formation of crystals. It must be borne in mind that the solubility equilibrium may be mistaken with the impossibility of further crystal formation, which can happen if the crystal surface has impurities or if it improperly oriented, not allowing the continuation of crystal growth [155], [156].

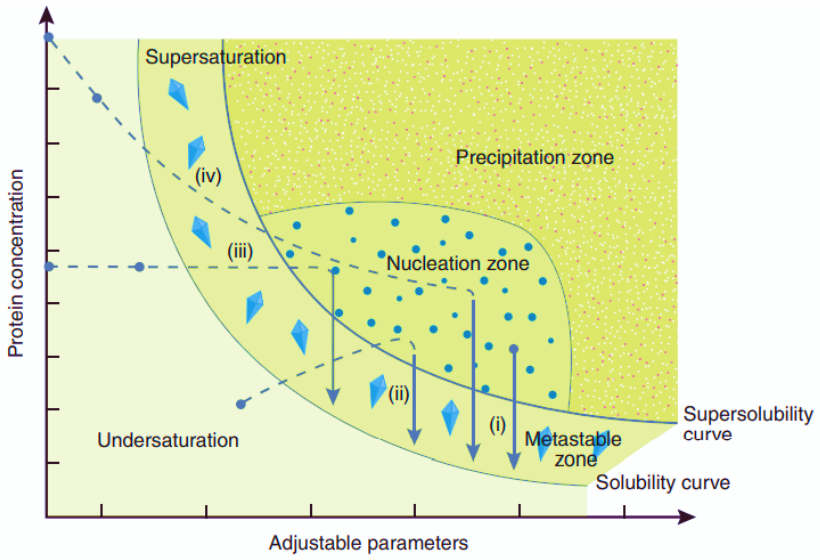

Figure 7 - *Crystallization phase diagram highlighting the solubility curve, Adapted from* [157]

Solution supersaturation involves three possible zones demonstrated in the phase diagram: metastable zone, nucleation or labile zone and precipitation zone (Figure 7). Supersaturation needs to be large, as the nucleation rate depends on the amount of supersaturation, the ability and rate at which the energy barrier to the formation of the nucleus is overcome. It is from this small cluster of proteins that the crystal will develop from. The nucleation rate can therefore be to slow for a protein crystal to develop over a satisfactory and useful period of time. In the phase diagram, this description corresponds to the metastable area (Figure 7). Supersaturation when large enough allows for spontaneous nucleation. However, if it is too large, the formation of aggregates and precipitate (which form faster than crystals) will happen – precipitation zone. These qualitative boundaries between zones are useful when searching or tunning crystallization conditions.

Among all crystallization methods, in the aspect of this work, focus on vapor diffusion shall be given, more specifically, sitting vapor diffusion. The way it works is straight forward: the drop with the protein or protein complex is placed under vapor-liquid equilibrium with the crystallization solution in the reservoir (Figure 8). The drop holds lower reagent concentration, forcing water to evaporate from the drop to reach equilibrium. This process results in an increase in relative supersaturation of the drop, hopefully leading to the formation of crystals.

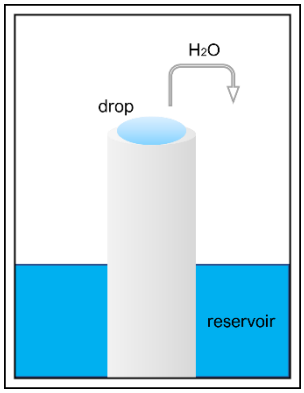

Figure 8 *- Schematics of sitting vapor diffusion process.*

It is to note that salt crystals might develop in the protein crystallization setups. When observing a crystal under the microscope one can look out for certain aspects before being thrilled about possibly having a protein crystal. Salt crystals can form when the crystallization solution contains magnesium, calcium, zinc, cadmium, or even when the purification process of the target biological molecule resorted to buffers containing phosphate. Combinations such as magnesium and ammonium, calcium and citrate, sodium fluoride in Polyethylene Glycol (PEG), ammonium sulfate and phosphate can also favour the formation of salt crystals. It is possible to address birefringence of a crystal coupling a polarizing filter to the optical microscope. Protein crystals, unless there are cubic, will exhibit weak birefringence while salt crystals show a strong birefringence. Protein crystals are also more easily crushed than a salt crystal; they can absorb dyes and be destroyed by fire, unlike most salt crystals. The most

significant way to test crystal's nature is through analysing its X-Ray diffraction pattern [158]–[161].

X-Ray crystallography has been for a long time the most recurred to and helpful technique in obtaining structural characterization of biological macromolecules. The 3D structure of a macro-bioactive molecule is of extreme importance towards gaining insight on its biological role and mechanisms of action. Complementary techniques may be used for analysis of protein structures in solution, such as Nuclear Magnetic Resonance (NMR) and Small Angle X-Ray Scattering (SAXS), and the determination of the 3D structure of proteins by cryo-electron microscopy has shown an impressive increase. The first step towards obtaining a molecular structure by X-ray diffraction crystallography is forming good protein crystals, for which preparation of highly pure protein sample is critical. Additionally, conformationally heterogeneous mixtures of proteins, such as those typically associated with proteins containing intrinsically disordered regions, critically hamper the growth of ordered crystals.

As mentioned above, nanobodies can be helpful tools in aiding the formation of protein crystals that are natively difficult to generate, as happens for Atx3, a protein with large unstructured regions. Nanobodies might also help reduce the conformational flexibility of the protein one is studying [162]. Previously, crystals for different proteins were produced by using nanobodies as chaperones and, although it is a fairly recent method, it is gaining prestige for its simplicity and good results [132], [163]. They are very stable and soluble and can reach clefts inside proteins which were not accessible to full antibodies or other fragments. Nanobodies can be crystallized alone, if possible, to use that information to aid in the determination of the structure of the protein-Nb complex. Knowing the nanobody's 3D structure can give an idea to its corresponding ligand form.

2.5. Drosophila as a MJD Model

In vivo models of MJD have been successfully established in organisms ranging from invertebrate models such as the round worm - *Caenorhabditis elegans* - or the fruit fly – *Drosophila melanogaster* - to mammalian organisms such as the mouse and even a primate model (non-human). *In vivo* models are extremely important to study and understand disease pathogenesis, obtain information about diagnosis, and ultimately develop a treatment. Establishing a robust model of a disease, that resembles or has some phenotypic behaviour as seen in humans is very important, as clinical human trials follow up experiments in invertebrate and mammals. Histopathological brain samples that can be obtained according to disease progression and in different timepoints in animals substitute human brain samples that can only be obtained *post-mortem*, revealing only the final stage of the disease. Besides humans, no naturally occurring MJD affected animals exist, meaning that animal disease models must be generated by classical transgenic methods, transfection with a viral construct or by

modification (knock-in) of the endogenous ATXN3 orthologue integrating an expanded polyglutamine repeat with surrounding sequence.

Drosophila m. has been extensively used as a model organism in research. Several characteristics contribute to the flies' recurrent use: these are cheap and easy to maintain in the laboratory, reproduce quickly and have a short life cycle allowing fast results, place the embryos externally, which permits to genetically modify them. Furthermore, as it is considered a simple organism, there are not many ethical obstacles or much regulation about its use and experiments with a high number of specimens can be conducted. After the presentation of the sequence of the *Drosophila* m. genome (year 2000) [164] and the human genome (year 2001), it was possible to verify that there was a similarity of about 75% between the genes causing diseases in humans and their counterparts in the fruit fly, confirming that this organism was a good model for studying disease mechanisms. In the specific case of MJD, however, there is no orthologue gene for *ATXN3* in *Drosophila m. .* Multiple genetic tools have been developed for *Drosophila m.*, making it relatively simple to produce transgenic flies bearing DNA that activates or inhibits the expression of individual genes of interest and this can be throughout the organism or in a defined tissue. *Drosophila m.* has four chromosome pairs, the first being the sex chromosomes, and the three remaining autosomes. It undergoes a four-stage life cycle: egg (embryo), larva, pupa, and fly (Figure 9). It takes about 10 days for a fly to hatch. Females become sexually mature 8-10 hours after eclosion and can put up to 100 eggs per day for up to 20 days [165]. Embryogenesis is a complex and elaborate process, involving multiple variables that need to be working together perfectly to generate a living being. Disrupting any of the processes underlying embryo development may lead to deformities in the adult animal, infertility or even death. Since there are no licencing laws nor thorough regulation for the use of *Drosophila m*. it is permitted to genetically manipulate the embryos, at the researcher's discretion.

Handling the flies is simple, as they can be anaesthetized without danger with carbon dioxide. This is routinely done either by inserting a tip inside the tubes or bottles where the flies are growing or by using porous pads connected to a source of carbon dioxide [166]. They are handled with a soft brush or clamp and seen over a magnifying glass (Figure 10).

2.5.1. GAL4-UAS system

The GAL4-UAS system is extensively used in the fruit fly to study and manipulate gene expression and function. It contains the GAL4 gene, which encodes the yeast transcription activator protein Gal4, and an enhancer, UAS (Upstream Activation Sequence) to which Gal4 binds to activate gene transcription. These yeast proteins allow the expression of genes from any organism in *Drosophila m.* in a tissue and temporal specific manner [167]. The plasmid pUAST is widely utilized for GAL4-inducible expression of transgenes in *Drosophila m.* [168], [169]. It has multiple cloning sites with a variety of convenient restriction sites to allocate the gene of interest. To generate flies carrying GAL4 and pUAST constructs, early syncytial *Drosophila m.*

embryos are injected with the DNA of interest which will integrate the genome by P element-mediated transformation [170]. One of the sexes of flies (male or female) carries the UAS-gene-of-interest vector and the other, the GAL4 regulatory sequences. Only the offspring of this genetic cross will express the coding sequence downstream of the UAS, which is spatially and temporally activated by the promoter fused to GAL4.

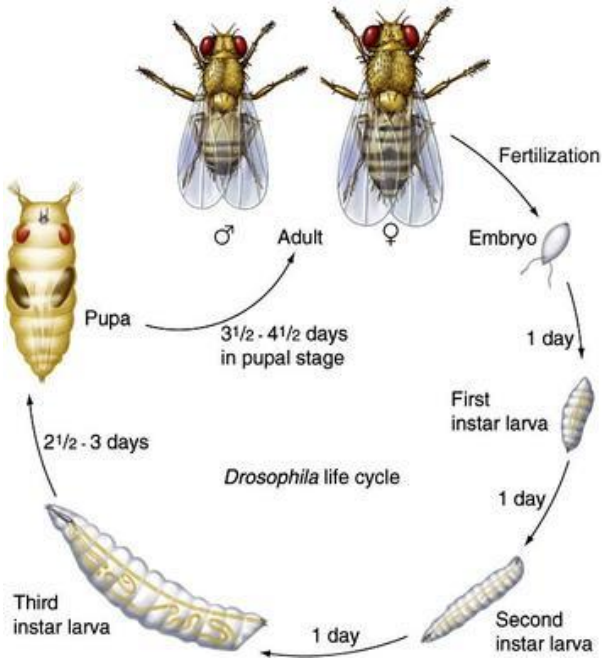

Figure 9 *- Drosophila m. life cycle. Adapted from Creative-Diagnostics*

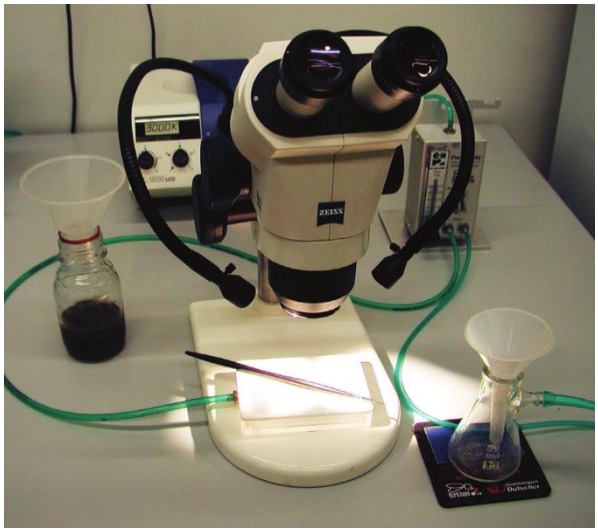

Figure 10 *- Typical workbench when dealing with Drosophila m.. A magnifying glass or stereomicroscope, a carbon dioxide pad, a fly morgue containing ethanol, a brush and a light source. Adapted from* [166].

The fly's adult eye as long been used as a reporter system to identify and understand how certain genes/proteins affect its morphology and functionality, specifically in the neural cells of the eye. To promote gene expression specifically to

the eye, a targeted expression is done by fusing an eye-specific promoter – GMR (Glass multiple promoter) to Gal4 [171]. GMR is therefore what would be referred to as a driver, conducting gene expression specifically and exclusively to the eye, including photoreceptor neurons as well as accessory pigment cells [172]. As GMR, there are other multiple drivers that have been discovered, like ELAV. *Elav* gene (embryonic lethal abnormal visual system) is expressed throughout the brain and is active in neurons making the ELAV protein a standardly used neural-specific marker [173]. The expression of *elav* at both the RNA and protein levels has been shown to be exclusive (newer studies have shown that there is ectopic activation of *elav* enhancer, in other tissues an cell populations, but it does not lead to detectable protein expression [174]), continuous, and ubiquitous in both the central and peripheral nervous system (CNS and PNS) neurons [175]. The expression of GAL4 stays under the control of the tissue-specific enhancers. The transgene to be expressed in the fly model is cloned downstream of a UAS sequence, for expression in the same tissue-specific pattern as the GAL4 activator (Figure 11). As mentioned, the transcriptional activator, GAL4, and the UAS transgene carrying are held in different parental lines having no lethality to the parental stocks [176].

Figure 11 *- GAL4UAS system representation. The GAL4 is driven in a defined spatial pattern either by a specified promoter or by an enhancer. The GAL4 protein binds to the UAS binding site activating the transcription of the gene of interest.*

2.5.2. *Drosophila m.* model of Machado Joseph Disease

Drosophila m. models for different and multiple neurodegenerative diseases have been established and have helped understand and bit by bit uncover important players in disease pathogenesis [177]–[182]. This applies to MJD as well; overall, GMR and ELAV drive the expression of ATXN3 with different polyQ sizes and account for most *Drosophila m.* models established for MJD (Figure 12).

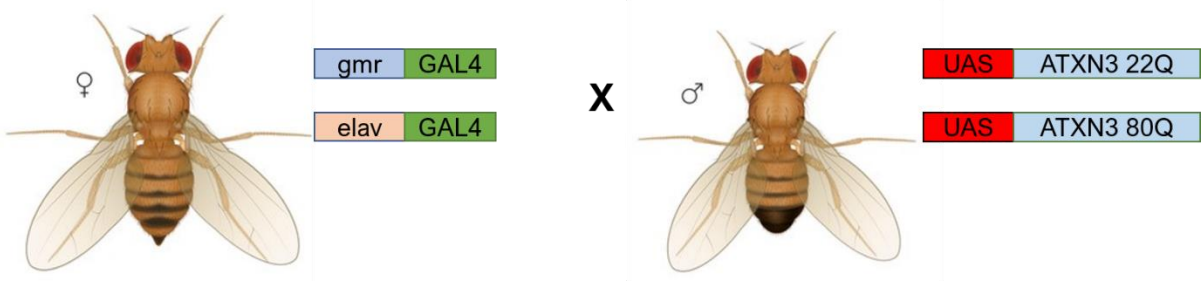

Figure 12 – *Exemplification of the set of flies carrying the UAS-gene-of-interest vector and the GAL4 regulatory sequences. The image shows defined sexes, but it can be the opposite. Upon crossing, the offspring will start to express the gene of interest derived from GAL4, in a specific tissue.*

A phenotype in the eye is seen when the GMR driver is used with UAS-*ATXN3* containing 77 to 80 glutamine repetitions, resulting in eye degeneration, with severe effects on morphology and pigmentation (Figure 13), observable under the stereomicroscope or magnifying glass and then confirmed by histological sections [183]–[185]. There can be loss of pigmentation, collapse of the eye, loss of cells beneath the eye's external surface and disorganization of bristles and overall eye structure [172]. Standard control lines express 22Q, 27Q and 28Q repeats. When using the ELAV driver, earlier death of the flies containing pathological polyQ stretches is the most noticeable outcome. Loss of photoreceptor morphology is also verified in cross-sections of the eye. The fact that there is such a strong and distinct phenotypic manifestation allows us to use these models to investigate and test the effect of compounds or molecules on disease modulation, by reversion or enhancement of the phenotype.

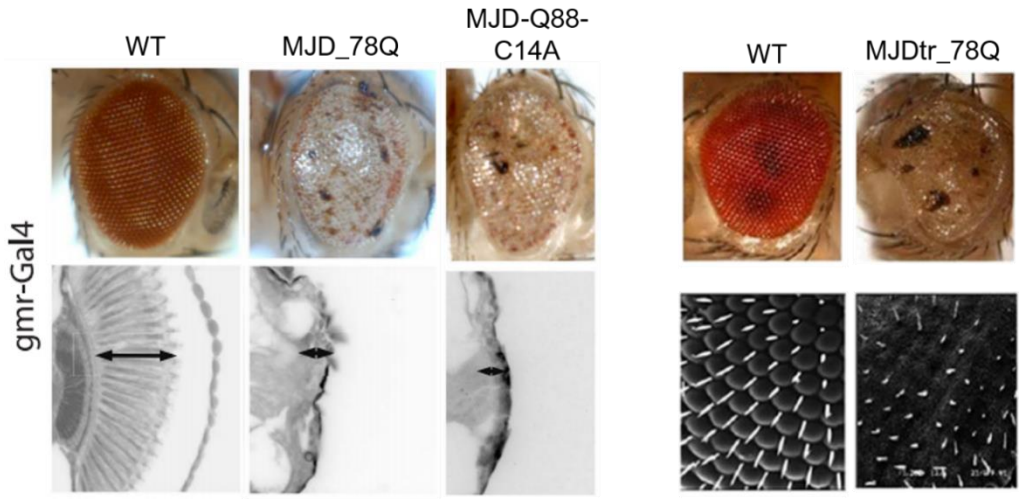

Figure 13 *- First group of images on the left show the phenotypic and histological comparison between the wild-type (WT) eye and the degeneration seen in flies expressing full ataxin3_78Q (MJD_78Q) and expressing a truncated form that renders the protein uncapable of performing its UBS activity (MJD-Q88-C14A). Adapted from* [184]*. On the right, dissecting microscope and electron microscope images allow for the comparison between WT and a truncated form of Atx3 (MJDtr_78Q) Adapted from* [183]*.*

Chapter 3

Materials and Methods

3.1. Materials

3.1.1. Reagents

For the expression of Nanobodies:

Terrific Broth (TB)	1.2% (w/v) tryptone
	2.4% (w/v) yeast extract
	0.4% (w/v) glycerol
	0.23% (w/v) potassium phosphate monobasic (KH2PO4)
	1.64% (w/v) potassium phosphate dibasic (K2HPO4)

For the expression of Atx3 variants:

Luria broth without NaCl (LBON)	1% (w/v) tryptone
	0.5% (w/v) yeast extract
	(autoclave at 120°C, 20min)
Luria broth without NaCl plates (LBON plates)	15g/L LB (without NaCl)
	20g/L Agar
	ddH2O
	(autoclave at 120°C, 20min) Add Ampicillin (100mg/L) to the medium when not too warm

Nanobody Purification:

Nb Buffer A	500mM NaCl
	50mM $NaPO_4$ pH 7.5
Nb Buffer B	50mM $NaPO_4$ pH 7.5
	500mM NaCl
	300mM imidazole
Nb SEC Buffer	50mM $NaPO_4$ pH 7.5
	150mM NaCl

Atx3 variants Purification:

Atx3 Buffer A	20mM $NaPO_4$ pH 7.5
	500mM NaCl
	20mM Imidazole
	2.5% Glycerol
Atx3 Buffer B	20mM $NaPO_4$ pH 7.5
	500mM NaCl
	500mM imidazole
	2.5% Glycerol
Atx3 SEC Buffer	20mM $NaPO_4$ pH 7.5
	150mM NaCl
	5% (v/v) glycerol
	2mM EDTA
	(on the day of use add) 1mM DTT

Complex Crystallization (Atx3:NB) :

Complex repurification buffer	20mM HEPES pH 7.5
	150mM NaCl
	5% (v/v) glycerol
	2mM EDTA
	1mM DTT

Aggregation assay (ThioT, SEC):

Aggregation Buffer	20mM $NaPO_4$ pH 7.5
	150mM NaCl
	1mM DTT

Filter Retardation assay buffers:

TES Buffer	50 mM Tris-HCl pH 7.5
	150 mM NaCl
TES Buffer w/ 0.1% SDS	50 mM Tris-HCl pH 7.5
	150 mM NaCl
	0.1% (w/v) SDS
TES Buffer w/ 2% SDS	50 mM Tris-HCl pH 7.5
	150 mM NaCl
	2% (w/v) SDS
TBS-T	50 mM Tris pH 7.5
	150 mM NaCl
	0.1% (w/v) Tween 20

Dot-Blot:

TBS-T	50 mM Tris pH 7.5
	150 mM NaCl
	0.1% (w/v) Tween 20

SDS-PAGE:

Running Buffer	25 mM Tris
	192 mM glycine
	0.1% (w/v) SDS
	Final pH of 8.3

NATIVE-PAGE:

Running Buffer	25 mM Tris
	192 mM glycine
	Final pH of 8.3
Sample Running Buffer (2X)	62.5 mM Tris-HCl pH 6.8
	40% glycerol
	0.01% Bromophenol Blue

3.1.2. Antibodies

Primary Antibody	Host	Dilution	Incubation
Anti-Atx3 1H9 (MAB5360, Millipore)	Mouse	1:10 000 in TBS-T w/ 3% BSA	1h, RT
Anti-Amyloid Fibrils OC[136] (AB2286, Millipore)	Rabbit	1:50 000 in TBS-T w/ 3% BSA	ON, 4ºC
Anti-Amyloid Oligomer A11[137] (AB9234, Millipore)	Rabbit	1:1000 in TBS-T w/ 3% BSA	1h, RT

Secondary Antibody	Dilution	Incubation
Anti-Rabbit-HRP (A6154, Sigma-Aldrich)	1:10 000 in TBS-T w/ 3% BSA	1h, RT
Anti-Mouse-HRP (A4416, Sigma-Aldrich)	1:10 000 in TBS-T w/ 3% BSA	1h, RT

3.1.3. Bacterial Strains

Bacterial Strain	Application	Genotype
E. coli DH5α (Invitrogen)	Plasmid replication	F- endA1 glnV44 thi-1 recA1 relA1 gyrA96 Φ80dlacZΔM15 deoR Δ(lacZYA-argF) U169 nupG, hsdR17(rK- mK+), λ–
E. coli BL21-SI (Stratagene)	Protein expression (Atx-3)	F- ompTlon $hsdS_B$ (r_B-, m_B-) gal dcm endA1 proUp::T7 RNAP::malQ-lacZ (Tet^S)
E. coli WK6 (su-) (Instruct)	Protein expression (NB)	Δ lac-proAB), galE, strA/F' $lacI^q$,lacZΔM15, $proA^+B^+$]

3.1.4. Plasmids

Atx3-13Q	pDEST17_TevG_Atx-3 13Q	Induction: 2xLB; 3M NaCl Resistance: Ampicillin
Atx3-77Q	pDEST17_TevG_Atx-3 77Q	
Nbs	pMESy4 GenBank KF415192	Induction: 1mM IPTG Resistance: Ampicillin

3.1.5. Ataxin3 Variants

The schematics and sequence of the Atx3 variants utilized are presented bellow as well as several protein properties.

Atx3 13Q

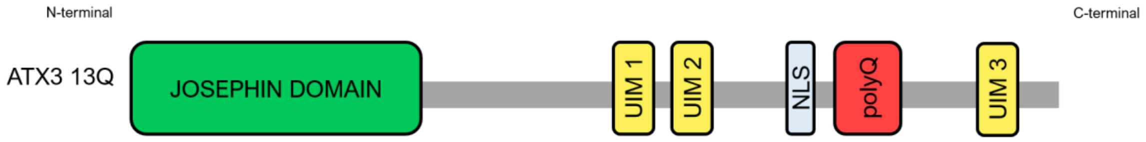

Sequence:

MSYYHHHHHHLENLYFQGMESIFHEKQEGSLCAQHCLNNLLQGEYFSPVELSSIAHQLDEEERMRM AEGGVTSEDYRTFLQQPSGNMDDSGFFSIQVISNALKVWGLELILFNSPEYQRLRIDPINERSFICNYKEHW FTVRKLGKQWFNLNSLLTGPELISDTYLALFLAQLQQEGYSIFVVKGDLPDCEADQLLQMIRVQQMHRPK LIGEELAQLKEQRVHKTDLERVLEANDGSGMLDEDEEDLQRALALSRQEIDMEDEEADLRRAIQLSMQGS SRNISQDMTQTSGTNLTSEELRKRREAYFEKQQQKQQQQQQQQQQGDLSGQSSHPCERPATSSGALG SDLGDAMSEEDMLQAAVTMSLETVRNDLKTEGKK

MW – 43582.58 Da
Theoretical pI – 4.86
Ext. coefficient - 31650
Abs 0.1% (=1 g/l) - 0.726, assuming all pairs of Cys residues form cystines

Atx3 77Q

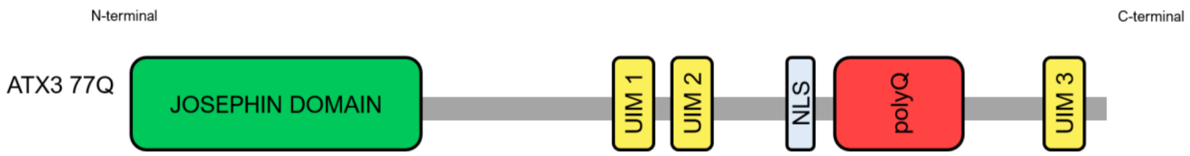

Sequence:

MSYYHHHHHHLENLYFQGMESIFHEKQEGSLCAQHCLNNLLQGEYFSPVELSSIAHQLDEEERMRM AEGGVTSEDYRTFLQQPSGNMDDSGFFSIQVISNALKVWGLELILFNSPEYQRLRIDPINERSFICNYKEHW FTVRKLGKQWFNLNSLLTGPELISDTYLALFLAQLQQEGYSIFVVKGDLPDCEADQLLQMIRVQQMHRPK LIGEELAQLKEQRVHKTDLERVLEANDGSGMLDEDEEDLQRALALSRQEIDMEDEEADLRRAIQLSMQGS SRNISQDMTQTSGTNLTSEELRKRREAYFEKQQQKQQQQQQQQQQQQQQQQQQQQQQQQQQQQ QQQQQQQQQQQQQQQQQQQQQQQQQQQQQQQQQQQQQQQQQQQQQQQQRDLSGQSSHPCERP ATSSGALGSDLGDAMSEEDMLQAAVTMSLETVRNDLKTEGKK

MW – 51882.08 Da
Theoretical pI – 4.9
Ext. coefficient - 31650
Abs 0.1% (=1 g/l) - 0.610, assuming all pairs of Cys residues form cystines

Legend:
HHHHHH – 6xHistidine tag
ENLYFQG – TEV cleavage site
GFFSIQVISNALKVWGLELILFNS – Josephin domain aggregation-prone region
QQQKQQQQ...QQQQQQ – PolyQ region

3.2. Methods

3.2.1. *Escherichia coli* Cell Transformation

Distinct *Escherichia coli* (*E. coli*) strains were transformed with the plasmid of interest for plasmid DNA amplification or recombinant protein expression.

a) *E. coli* DH5α cells were used for plasmid DNA replication.
b) *E. coli* BL21-SI cells were used for the expression of Atx3 variants (pDEST17 plasmid expressing 6His-Atx3 (full length Atx3 13Q and expanded Atx3 77Q)).
c) *E. coli* WK6(su-) cells were used for the expression of Nbs (pMESy4 plasmid expressing 6His-Nb).

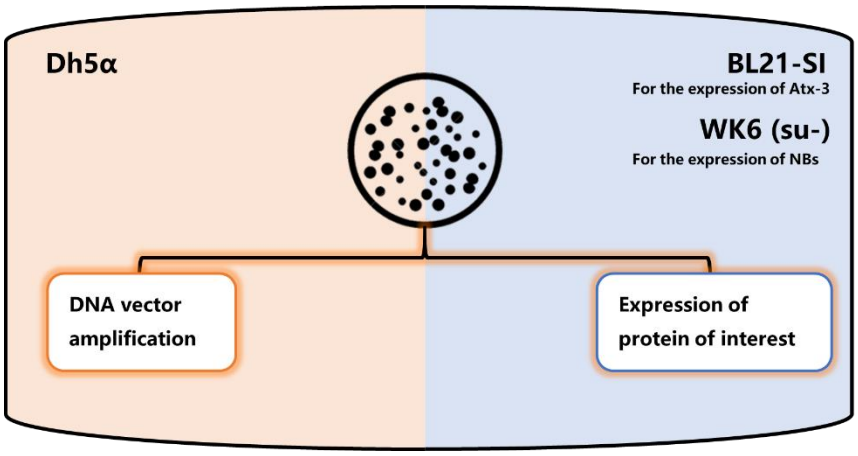

Figure 14 *- Cells used for expression of protein and plasmid DNA amplification.*

The plasmid, 1µL (50-100 µg/mL), was incubated with 50 µL of competent cells for 30 min on ice. Transformation trough heat shock was done for 45 sec at 42°C. Afterwards, cells were incubated on ice for 10 min. Following, 500 µL of medium (LB_{ON} for BL21-SI and Dh5α and TB for WK6 (su-) and incubated for 1h at 37°C, 180rpm. After centrifugation (1min, 11000rpm, RT) and resuspension in 100 µL of corresponding medium cells were plated in the corresponding plates (LB_{ON} plates supplemented with ampicillin (Sigma-Aldrich, USA) for DH5α and BL21-SI and LB plates supplemented with 100µg/mL of ampicillin, 0.1% glucose and 1 mM $MgCl_2$ for WK6 (su-)). The plates were incubated overnight (ON) at 37°C (INCU-line, VWR).

3.2.2. Plasmid DNA replication/amplification

An isolated colony of the transformed cells is inoculated in 25mL of LB liquid medium and incubated overnight at 37°C, 180rpm (Shaker, IKA). Cells are then pelleted at 3500rcf for 10 min (Avanti J-26 XP - Rotor J-LITE JLA 8.1000, Beckman-Coulter) and the plasmid purification was done using a NZYTech Miniprep (MB010) or Midiprep (MB27901) Kit (depending on the desired amount of vector) following the protocol.

Final plasmid concentration was determined by measuring the absorbance at 260 nm using the Nanodrop (Thermo Fisher Scientific). To account for possible mutations during the replication process, nucleotide sequences of Nbs were confirmed by direct sequencing of the plasmids (LightRun, GATC biotech).

3.2.3. Recombinant Protein Expression

3.2.3.1. Ataxin-3 variants

A pre-inoculum was done by picking 4 to 5 colonies of the transformed *E. coli* BL21-SI cells from the plate and resuspending them in 150mL of LB_{ON} supplemented with 100 µg/mL of ampicillin and letting them grow overnight (ON) (37°C, 180rpm). Cells were then inoculated by adding 20mL of homogenized pre-inoculum to 500 mL LB_{ON} medium supplemented with 100 mg/L ampicillin and 0.4% (w/v) glucose, in baffled Erlenmeyers (2 L), and grown at 37°C, 180 rpm until the OD_{600} (optical density measured at 600 nm) reached 0.6-0.8. The culture was then cooled to 30°C and protein expression induced with 300 mM NaCl while the growth medium was supplemented with ampicillin (100 µg/mL). After 3 hours of expression, the cells were harvested by centrifugation at 4000 rpm, 25 min, 4°C (Avanti J-26 XP - Rotor J-LITE JLA 8.1000, Beckman-Coulter), resuspended in ice-cold Buffer A (50 mL for each 3 L of culture) and stored at -20°C.

3.2.3.2. Nanobodies

A pre-inoculum was done by picking 4 to 5 colonies of the transformed WK6 (su-) cells from the plate and resuspending them in 150mL of LB_{ON} supplemented with 100µg/mL of ampicillin, 0.1% glucose, 1mM $MgCl_2$ and letting them grow ON (37°C, 180 rpm). Cells were inoculated by adding 10mL of homogenized pre-inoculum to 500 mL TB medium supplemented with 100 µg/mL ampicillin, 0.1% (w/v) glucose and 1mM $MgCl_2$, in baffled Erlenmeyers of 2L, and grown at 37°C, 180 rpm until the OD_{600} reached 0.8-1. The Nb overexpression was then induced with isopropyl β-D-1-thiogalactopyranoside (IPTG) at a final concentration of 1 mM while the growth medium was further supplemented with 100 µg/mL of ampicillin. After 4h expression at 37°C, the cells were harvested by centrifugation at 4000 rpm, 25 min, 4°C (Avanti J-26 XP - Rotor J-LITE JLA 8.1000, Beckman-Coulter) resuspended in TES Buffer (30 mL/1.5L of cell culture) and stored at -20°C.

3.2.4. Recombinant Protein Purification

3.2.4.1. Ataxin-3 variants

The *E. coli* (Bl21-SI) cellular suspension was thawed, supplemented with 0.02 mg/mL DNase I (from bovine pancreas, Sigma-Aldrich), 1 mM MgCl2 and 1 mM

phenylmethylsulphonyl fluoride (PMSF) and lysozyme (concentration not specified) and stirred for 1h in an Erlenmeyer on ice, for smooth cell lysis. Afterwards, the suspension was centrifuged at 17000 rpm, 4°C for 45 min (Avanti J-26 XP, Rotor J-LITE JA 25.50, Beckman-Coulter).

The supernatant was filtered and loaded into Ni^{2+}-charged HisTrap column (GE Healthcare Life Sciences) pre-equilibrated with Nb buffer A at a flowrate of 2 mL/min and recirculated 2 times on the column. Protein was eluted with a gradient of 50mM, 250mM and 500mM of imidazole. The protein fractions eluted with 250mM of imidazole were injected on a HiPrep 26/60 Sephacryl S-300 HR column (GE Healthcare Life Sciences) pre-equilibrated with Atx3 SEC Buffer to separate Atx3 from contaminants. Elution was done at a rate of 2mL/min. Fractions of Atx3 (contaminants can persist) were pooled and concentrated in an Amicon Ultra-15 centrifuge filter (cut-off of 10 kDa, Millipore) to around 20 mg/mL. After concentration, Atx3 was centrifuged to remove possible aggregates (10min, 13200 rpm, 4ºC), frozen in liquid nitrogen and stored at -80ºC. To assess each step of the purification process and Atx3 purity samples were collected throughout the experiment and analysed by SDS-PAGE (as detailed below).

3.2.4.2. Nanobodies

A crushed pill of ethylenediaminetetraacetic acid (EDTA)-free protease inhibitor cocktail was added to each 50 mL of cellular suspension (corresponding to 1.5 L of cell culture) which was then shaken for 1h at 4ºC. Subsequently, the same volume of TES/4 buffer (TES diluted 4x) was added to the suspension that was shaken for at least more 45 min at 4ºC to cause an osmotic shock and release the proteins from the periplasmic space to the extracellular space. The suspension was centrifuged at 17000 rpm, 45min, 4ºC. The supernatant was filtered (0.22 µm PVDF filter) and loaded into Ni^{2+}-charged Histrap column (GE Healthcare Life Sciences), pre-equilibrated with Nb Buffer A, at a flow rate of 2mL/min and 2x recirculated. Nanobodies were eluted with a single elution step with 300mM of imidazole. Corresponding fractions were collected, pooled and concentrated in an Amicon Ultra-15 centrifuge filter (cut-off of 10 kDa, Millipore) up to a volume of 500 µL, loaded into a Superdex 75 10/300 GL column, pre-equilibrated with Nb SEC buffer, and eluted at a rate of 0.5 mL/min. Protein concentration was measured in the NanoDrop before injection to prevent saturation of the column. Fractions with pure nanobody were pooled and concentrated in an Amicon Ultra-15 (cut-off of 3 kDa) centrifuge filter (Millipore) to around 20 mg/mL. After concentration, protein was centrifuged to remove possible aggregates (10min, 13200 rpm, 4ºC), frozen in liquid nitrogen and stored at -80ºC. To assess each step of the purification process, and Nbs purity, samples were collected throughout the experiment and analysed by SDS-PAGE (as detailed below).

3.2.4.3. Ataxin3:Nanobody complex

The proteins of interest were thawed and centrifuged to remove possible aggregates (10min, 4ºC, 132000 rpm). The Atx3 variant was mixed with the selected Nb at a molar

ratio of 1:2 and incubated 1h on ice in a low-binding Eppendorf. To purify the Atx3:Nb complex, the samples were filtered by centrifugation (2 min, 4ºC, 10000 rpm) using centrifugal filters 0.22 μm (Ultrafree, Millipore), injected into a Superdex 75 10/300 GL column pre-equilibrated in complex repurification buffer and eluted at a rate of 0.5 mL/min. Fractions corresponding to the Atx3:Nb complex were pooled and concentrated in an Amicon Ultra-15 (cut-off of 30kDa) centrifuge filter (Millipore) to around 20 mg/mL. After concentration, the sample was centrifuged to remove possible aggregates (10min, 13200 rpm, 4ºC), diluted to the final desired concentration of 17 mg/mL and used directly in the crystallization assay or frozen in liquid nitrogen and stored at -80ºC.

3.2.5. SDS-PAGE analysis

Throughout the process of expression and purification, and ultimately, other experiments and procedures, samples are collected to study the protein expression levels and the presence of possible contaminants by sodium dodecyl sulphate polyacrylamide gel electrophoresis (SDS-PAGE) analysis. Gels are prepared following the recipe below (Table 2) based on the molecular weight of the proteins we want to analyse (Table 3). Sample preparation is done by diluting the protein sample into SDS sample loading buffer (5X) and denaturing for 5 min at 100°C, usually in a total volume of 10μL. For each gel, a running voltage of 30mV is applied. Unstained SDS-PAGE protein ladder standards with the corresponding molecular weight from Bio-Rad were used (Figure 15).

Table 2 *- SDS-PAGE gel recipe of different percentages for a total amount of 2 gels. Resolving and Stacking gel composition.*

Resolving Gel						**Stacking Gel**	
	8%	**10%**	**12.5%**	**15%**			**4%**
H_2O	4.7 mL	4.09 mL	3.5 mL	2.7 mL		H_2O	2.34 mL
1.5M Tris pH 8.8	3.45 mL	3.45 mL	3.45 mL	3.45 mL		0.625M Tris pH 6.5	937.5 μL
40% acrylamide	2.1 mL	2.6 mL	3.3 mL	3.9 mL		40% acrylamide	450 μL
10% SDS	210 μL	210 μL	210 μL	210 μL		10% SDS	75 μL
10% AMPS	105 μL	105 μL	105 μL	105 μL		10% AMPS	37.5 μL
TEMED	10.5 μL	10.5 μL	10.5 μL	10.5 μL		TEMED	3.5 μL

Table 3 *- Gel percentage according to the molecular weight range (in kDa) of the proteins under study.*

Gel percentage	**5%**	**7.5%**	**10%**	**12.5%**	**15%**
Molecular Weight range resolved (kDa)	100-250	40-200	30-150	20-120	10-100
	18%	**4-15%**	**4-20%**	**8-16%**	**10-20%**
	6-50	20-250	10-200	6-70	10-100

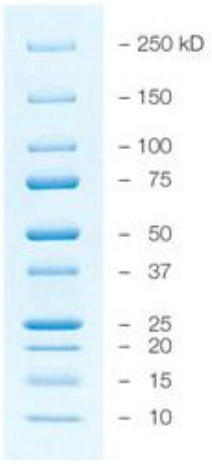

Figure 15 *- Precision Plus Protein™ Unstained Protein Standards, Bio-Rad #1610363*

3.2.6. Protein concentration

Protein concentration was determined by measuring the absorbance at 280 nm with a Nanodrop 1000 spectrophotometer (Thermo Fisher Scientific) and using the protein extinction coefficient determined from the amino acid sequence (values for Atx3 and Nbs are displayed in Appendix II.).

3.2.7. Determination of the Nbs' Melting Temperature (T_m)

Protein thermal stability can readily be assessed with inexpensive and non-time-consuming assays that rely on fluorescent dyes and their tight detection. This type of screening is usually done to understand which buffer conditions favour protein stability. This can be useful to establish optimal protocol settings when dealing with proteins, for example in recombinant expression of a protein followed by purification. As a protein unfolds, which naturally occurs with increasing temperature, hydrophobic regions are exposed. The fluorescent dye used, SYPRO Orange is highly fluorescent in non-polar environments and sees its fluorescence quenched when in aqueous solution. The dye binds to the hydrophobic areas of the protein and the unfolding process is assessed by increasing fluorescence intensity. In this experiment, a thermal shift assay in the presence of SYPRO Orange dye was conducted to explore the thermal stability of the nanobodies NB03 to NB17 by determining their T_m (the temperature at which concentrations of folded and unfolded protein are equivalent). The results give indications of what path to proceed to temper with a protein's stability, if intended.

The SYPRO Orange (Invitrogen) 5000x concentrated in dimethyl sulfoxide (DMSO) was diluted in the Nb SEC buffer prior to mixing it with the protein. Solutions of 25 µL (1.2 mg/mL) of Nb and 25 µL (10x) of SYPRO Orange (in corresponding buffer) were loaded in a white 96-well PCR plate (Bio-Rad). For all the conditions three replicates were prepared. The thermalshift assay was performed in an iCycler iQ5 Multicolor Real

Time PCR detection system (Bio-Rad) running the following protocol: heating from 25°C to 85°C with a 30s hold time every 0.5°C, followed by a fluorescence reading using Cy3 dye filter (excitation/emission, 545/585). Melting curves were analysed using the CFX Manager software (Bio-Rad) to calculate melting temperature (Tm) from the maximum value of the first derivative curve of the melting curve.

3.2.8. Native Gel Analysis

Proteins carry an overall net charge. The separation of molecules is sought with the application of an electric field, causing charged molecules to move. For proteins, the rate at which they move against the electrode of opposite charge, depends on several factors: intrinsically on the physical characteristics of the protein (size, shape and charge) and also on all participants in the electrophoresis system (the buffer and its concentration, pH, temperature, etc)[186]. Contrarily to SDS-PAGE, Native-PAGE analyses proteins in their native, folded state. Since each protein has a characteristic migration rate, this can be exploited for purposes of separation. The interaction between Nbs and Atx3, potentially leading to complex formation, can be detected by this assay. If a shift in the characteristic band (or bands – resulting from different conformations of the protein) of Atx3 appears when incubated with the Nb, one can assume that an interaction is occurring between the two proteins and that the Nb binds to a monomeric form of Atx3.

Native gels were prepared following the recipe below (Table 4) and stored at 4°C. Sample preparation was done by diluting 1-part sample with 1-part native sample loading buffer (Bio-Rad #161-0738). Gels were ran at 100mA and then stained with Blue-Safe (NZYTech).

***Table** 4 - Native Gel recipe for preparing four gels. Running and Stacking gel composition.*

Running Gel 8%			**Stacking Gel 4%**	
Acrylamide 40%	2.7 mL		Acrylamide 40%	1 mL
1.5M Tris.HCl pH 8.8	3.2 mL		1.5M Tris.HCl pH 8.8	3.2 mL
10% APS	133 µL		10% APS	100 µL
TEMED	13.3 µL		TEMED	10 µL
H_2O miliQ	8.3 mL		H_2O miliQ	5.7 mL

3.2.9. Thioflavin-T Aggregation Assay

Thioflavin T (ThioT) (Figure 16) is widely used to detect the presence of amyloid fibrils, characteristic of several diseases. The binding of this molecule to fibrils provides strong fluorescence signal at approximately 482 nm when excited at 450 nm [187]. Fluorescence of ThioT is correlated with the concentration of amyloid present. The effect that ThioT has on aggregation kinetics depends on the protein under study, but it should have no influence on low concentrations (for example 20 µM or lower for proteins Aβ40 and Aβ42, related with Alzheimer's disease) [188]. It has been recognized that truncated forms, normal and expanded Atx3 variants form ThioT

positive aggregates [56], [57]. The assay intends to study the kinetics of the formation of aggregates to understand how the presence of additional participants, as the Nbs, modulates aggregation. Standard ThioT assay profile shows a curve with three sequential phases: lag phase, elongation phase and stationary phase. During the lag-phase, with the presence of monomers and dimers (small oligomers), there is no report from the fluorophore, making the first steps of aggregation not noticeable (concentration bellow detection limit). With the elongation of oligomers into protofibrils, the corresponding elongation phase has an exponential fluorescence signal increase. At the stationary phase, the aggregation process has reached its endpoint with an equilibrium of the amount of fibrils and stabilization of signal.

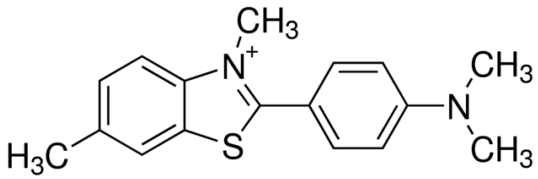

Figure 16 *- Structure of TioflavinT*

Thawed aliquots of purified Atx3 (13Q or 77Q) were centrifuged to remove possible precipitated aggregates (13200 rpm, 10 min at 4 ºC - Himac CT 15 RE, VWR). The protein was filtered in 0.22 µm filters - Ultrafree, Millipore (2 min, 13000 rpm at 4°C) and repurified in an analytical SEC Superpose 12 column (GE Healthcare Life Sciences) equilibrated in Aggregation Buffer. The concentration of the fractions corresponding to Atx3 was determined by measuring the absorbance at 280 nm (NanoDrop 1000) and the protein was filtered to remove possible aggregates (0.22 µm filters - Ultrafree, Millipore). Atx3 was diluted to a final concentration of 5 µM and Nbs were at a final molar ratio of either 1:1 (5 µM), 1:2 (10 µM), 1:5 (25 µM) or 1:10 (50 µM). 30µM of ThioT (SIGMA Aldrich) were added to a total volume of 50 µL in Aggregation Buffer (at least three replicates for each condition). The 50 µL samples were loaded in a low protein-binding Corning® Thermowell™ 96-well polycarbonate PCR microplate (Costar, Tewkesbury, MA, USA, Ref. 134371710A) and centrifuged (Sorvall ST 40, ThermoFischer Scientific) to eliminate possible air bubbles (1200 rpm, 2 min, RT). Each well was overlaid with 20µL of parafinn oil (Molecular Dimensions) to prevent sample evaporation. The Atx3 amyloid self-assembly was monitored on a FluoDia T70 microplate fluorimeter (Photon Technology International, Edison, NJ, USA) by measuring the Thio-T fluorescence at 480 nm (440 nm excitation) every 30 min, preceded by 3 seconds of low intensity butterfly sample mixing, over a period of 60-120 hours at 37°C.

3.2.10. Dot Blot Assay

Immunoblotting is a fast way to detect and specifically characterize the presence and state of proteins in a sample by exploiting antigen-antibody recognition. Although this technique is widely used in conjunction with polyacrylamide gel electrophoresis

(PAGE), in the case of Dot-Blot, samples are not separated by electrophoresis but rather placed dropwise directly onto a nitrocellulose membrane and analysed. The membrane is incubated with the primary antibody designed for a specific target followed by the second antibody conjugated with an enzyme – horseradish peroxidase (HRP). Anti-Amyloid Oligomer A11 antibody binds specifically to conformational amyloid oligomers. It recognizes an epitope that is present in amyloid oligomers, but not in native proteins, amyloidogenic monomer or mature amyloid fibrils [189], [190]. Anti-Amyloid Fibrils OC antibody recognizes generic epitopes present in many amyloid fibrils and protofibrils, but not native proteins or prefibrillar oligomers. Finally, Anti-Atx3 1H9 antibody binds to the epitope at E214-L233 residues of Atx3, meaning that it is useful to qualitatively establish the amount and presence of Atx3 in a sample.

Samples from the corresponding Thio-T assay endpoint were collected for a dot-blot immuno-assay. 3µL of each sample were loaded dropwise in a nitrocellulose membrane (Bio-Rad). The membrane was blocked with 5% BSA in TBS-T for 1h at RT and then successively incubated with antibody anti-Atx3 A11 (1:1000) (1h at RT), antibody anti-OC (1:50000) (ON at 4°C) and antibody anti-Atx3 1H9 (1:10000) (ON at 4°C) and corresponding secondary antibodies: anti-rabbit-HRP (1:10000) (1h at RT) for the first two and anti-mouse-HRP (1:10000) (1h at RT) for the last one. A list of the primary antibodies and the corresponding secondary antibodies is displayed in the "Reagents" section. The process for each immunoblot was cyclic and repeated for each pair of primary and secondary antibodies. The membrane was developed with ECL reagent (GE Healthcare Life Sciences) and then stripped using Restore Western Bolt Stripping Buffer (Thermo Fisher Scientific).

3.2.11. Filter retardation assay

Filter retardation assay or Membrane filter trap assay aims to ascertain aggregate's resistance to SDS. PolyQ aggregates are stable and retain their structure upon incubation with SDS [191], [192]. Although non-expanded Atx3 can aggregate in vitro, the fibrils are dissolved upon incubation with SDS at least at a concentration of 0.1% (w/v). Only expanded Atx3 aggregates into SDS-resistant aggregates. This characteristic can be exploited to understand how nanobodies modulate the aggregation pathway of Atx3. The principle is that SDS-resistant mature fibrils will not pass through the cellulose acetate membrane under vacuum, while other species of Atx3 will. Probing with the Anti-Atx3 1H9 antibody will show Atx3 retained in the membrane.

From samples of ThioT assay endpoints, 5µL were collected and diluted 40-fold in TBS with 2% (w/v) SDS. The samples were boiled at 100°C for 5 minutes. Two filter papers (BioDot SF – Bio-Rad) and the cellulose acetate membrane (pore size 0.2 µm - Whatman) were soaked in TBS buffer and then mounted on the vacuous system as in (Figure 17) (BioDot SF microfiltration apparatus – Bio-Rad), the cellulose acetate membrane on top of the filter papers. The system was closed and all wells pre-

equilibrated with TBS. The samples were loaded and filtered through the membrane with vacuum without letting the membrane dry completely. The membrane was then washed two times with TBS with 0.1% (w/v) SDS and blocked with 5% milk in TBS-T for 1h at RT (room temperature). The membrane was incubated with the primary antibody – anti-Atx3 1H9 (Millipore) (1:10000) – overnight at 4°C, followed by the secondary antibody – anti-mouse (Sigma-Aldrich) (1:10000) – for 1h at RT. Washes in the intermediate steps were done 4 times with TBS-T for 5 minutes. The membrane was developed using ECL reagent (GE Healthcare Life Sciences).

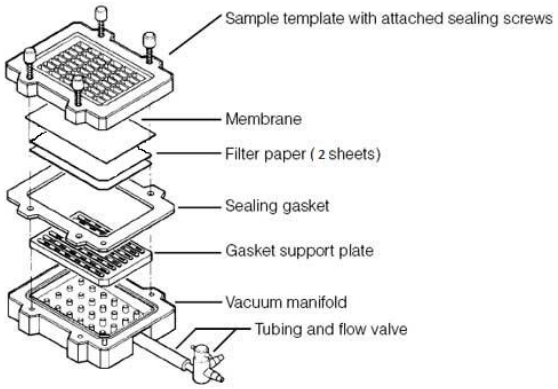

***Figure 17** - Schematic representation of the vacuum system for filter retardation assay. The experiment samples were removed from the Thioflavin-T assay aggregation plate and treated with SDS and loaded to wells of the system with a cellulose acetate membrane placed on top of filter paper.*

3.2.12. Negative Staining for Transmission Electron Microscopy

Transmission Electron Microscopy (TEM) is widely used as a technique to obtain clear images of biological molecules or entities in a quick and simple manner. Morphology is the main characteristic addressed. Proteins have a low scattering power due to their atomic composition (mainly light elements as hydrogen, carbon, nitrogen, sulphur) giving them very little or no contrast [193], [194]. To overcome this, a negative staining is applied, normally a solution of an electron-dense metal atom, to give negative contrast where theoretically there is no significant reaction between the stain and the entities under study leaving the background stained (the electron beam is scattered) and the sample unaffected (the beam passes through), giving the final image the necessary contrast [195].

A pre-treatment of the TEM grids (carbon film coated) was done through glow-discharge, to assure the sample strongly adheres and spreads through the entire grid and stays during further processing (e.g. washing). 1% (w/v) Uranyl Acetate was the negative stain used. 4 µL of sample diluted 1/5 in miliQ H_2O were deposited on the carbon side of the grid for 1 min inside a cold incubation station. Between each step, liquid excess was removed with filter paper. The processing was done stepwise in a prepared station with 3 drops of 35µL of miliQ water and 1% UA as illustrated in Figure 18. The grid was washed 3 times in water drops and promptly placed on the first drop of UA incubating for 10 seconds (second drop incubating for 10 sec and third drop

incubating for 1 min). Excess solution was removed, and the grid left to dry laying on a sheet of filter paper inside a covered petri dish, for at least 30 min at RT.

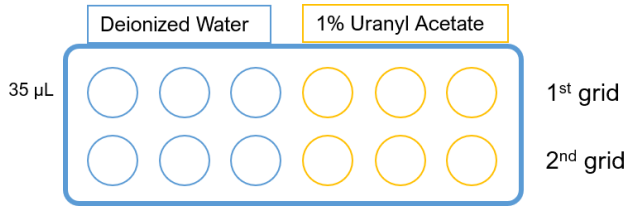

Figure 18 *- Schematics of station preparation for sample processing.*

3.2.13. Size Exclusion Chromatography for the analysis of aggregation modulation

Size Exclusion Chromatography (SEC) is a valuable qualitative and quantitative mean of analysis of potential therapeutic proteins by monitoring aggregation of proteins. The conditions under which the experiment is conducted provokes none or little change in protein conformation. This technique separates molecules based on their size, more specifically, on their hydrodynamic radius. It permits to differentiate between different species along the aggregation pathway based on their molecular weight. A protein aggregation model monitored by SEC was validated for Atx3, confirming that the formation of high-order aggregates depletes the concentration of the smaller species to levels below the detection limit in a time period of 80 hours [64]. SEC allows to address nanobody effect on modulating Atx3 oligomerization.

Proteins were thawed and Atx3 variants repurified in a Superose 12 10/300 GL pre-equilibrated with Aggregation Buffer, to change the buffer, removing the glycerol from the sample, and possible Atx3 aggregates and intermediate oligomeric species formed along the freezing and thawing process. 5 µM of Atx3 were incubated alone and with 25 µM of nanobody (ratio 1:5) in a total of 1 mL of Aggregation Buffer at 37ºC. 105 µL samples were collected over the course of 96 hours at different time points. The samples were filtered in 0.22 µm filters - Ultrafree, Millipore (2 min, 10000rpm, 4°C) and injected on a Superdex 200 Increase 5/150 GL column to analyse the evolution of the SEC profile.

3.2.14. Complex Crystallization

After purification of Atx3:NB complexes (detailed in Ataxin3:Nanobody complex method) crystallization plates were prepared using commercial crystallization kits: Morpheus, SG1, Crystal Screen Cryo and INDEX. Using robot Oryx 4 (Douglas Instruments) crystallization plates with 96 wells and 2 drops each (SWISSCI, Scientific Innovation) were prepared testing for Atx3 13Q:NB02 and Atx3 13Q:NB20 on a molar ratio of 1:2. Sitting drops were composed of 0.15 µL of complex and 0.15 µL of reservoir crystallization solution (ratio of 1:1) with 50 µL reservoir volume. All plates

were stored at 20°C. As seen in the schematics below (Figure 19), it was possible to test the same reservoir solution conditions for two different protein complexes (Atx3 13Q:NB02 was on the upper well and Atx3 13Q:NB20 on the lower well).

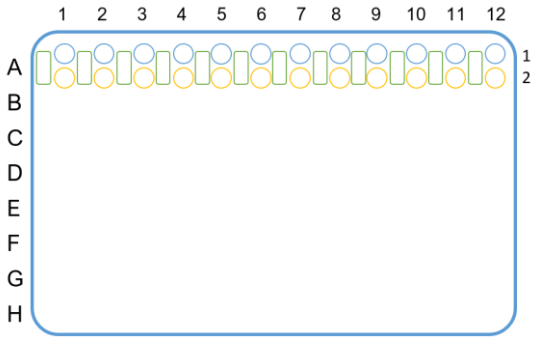

Figure 19 *- Schematics of a robot plate with 96 reservoirs and 192 wells. The pattern is shown for row A and repeats for all the other seven rows.*

When crystal hits were observed, optimization of promising crystallization conditions was attempted by varying the precipitants percentage and the pH of the Buffer (Figure 20). Manually preparing crystallization plates started by thawing the complex previously prepared or preparing a new batch and centrifugating to remove possible aggregates (10min, 4ºC, 13200 rpm). Reservoir solution was prepared by adding the desired concentrations of the components to a total of 300 µL: H_2O, Salt, Buffer and Precipitant, following this order. 1 µL of protein complex and 1 µL of reservoir solution were loaded to the wells (ratio 1:1). Plates were sealed, stored at 20°C and monitored over time using an optical microscope.

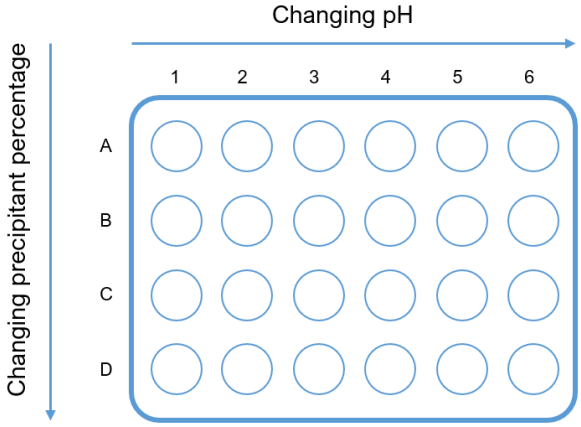

Figure 20 *- Schematic layout and approach to crystallization conditions optimization.*

3.2.15. pUASTattB-Nbs plasmids construction

3.2.15.1. Design Strategy

According to previously done experiments and collected data, nanobodies that showed the highest potential in modulating Atx3 aggregation, delaying it and preventing the formation of amyloid-like fibrils, were chosen to create vectors to transform *Drosophila m.* (Nanobody sequence cannot be revealed due to patenting and publishing reasons). PCR based cloning allows to place the Nb DNA coding sequence into the relevant vector backbone, pUASTattB (Gen Bank - EF362409.1). Primers were designed to specifically amplify the nanobody coding sequence from the standard used nanobody vectors (pMESy4) and the restriction sites of EcoRI and NotI at the 5' and 3' terminus, respectively (Figure 21).

FlyNB_EcoRI_F – GGTGGTGAATTCATGGCACAGGTGCAGCTGGT

FlyNB_NotI_R – GGTGGTGCGGCCGCCTAGGCTTCAGGTTCGTG

Figure 21 - *Primers forward and reverse for the amplification of the nanobody coding sequence.*

The cloning vector, pUASTattB, has restriction sites for the digestion with EcoRI and NotI (Figure 22).

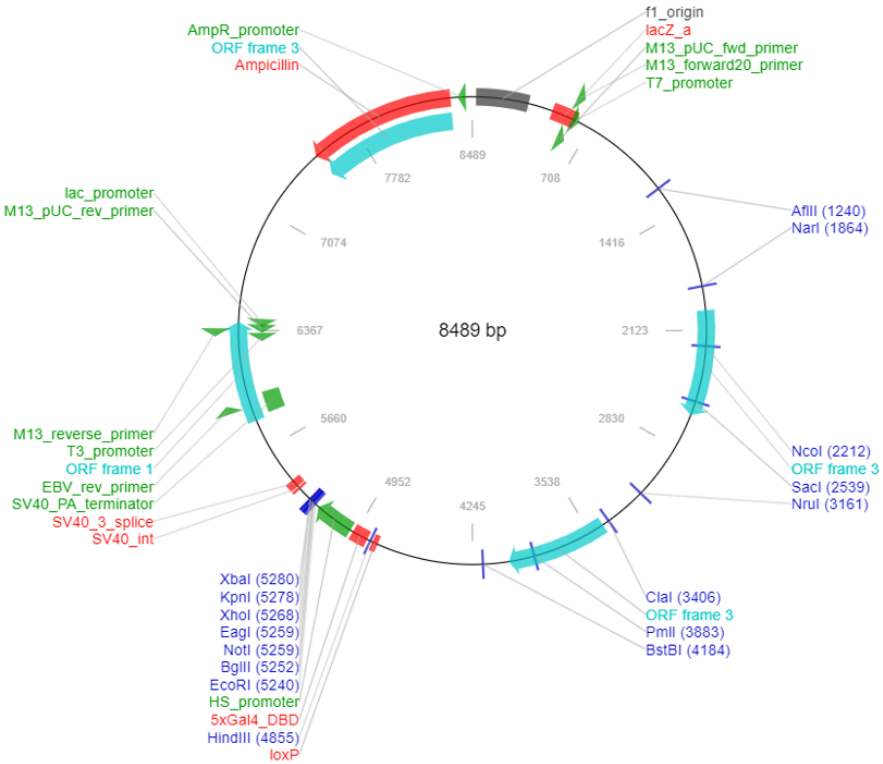

Figure 22 *- Plasmid Map of vector pUASTattB comprising the cutting sites for EcoRI and NotI.*

3.2.15.2. Amplification of Nb constructs

Amplification through Polymerase Chain Reaction (PCR) was done using the Phusion High-Fidelity DNA Polymerase. A PCR test was firstly conducted to find the optimal conditions for amplification of the Nbs sequence with a good yield analysing the products in an agarose gel. Annealing temperature was adjusted to the primers sequence. The PCR cycles utilized are presented below with corresponding values attributed to all variables (Table 5).

Table 5 *- PCR protocol for the amplification of Nb constructs*

Cycle step	Temperature	Time	Cycles
Initial denaturation	98°C	30s	1
Denaturation	98°C	10s	30
Annealing	65°C	20s	
Extension	72°C	15s	
Final extension	72°C	10 min	1
	8°C	Hold	

Phusion High-Fidelity DNA Polymerase and 5X Phusion HF Buffer (Thermo Fisher) were used. Following the instructions from the commercial protocol, all items were added as follows (Table 6):

Table 6 *- Final concentrations of the participants in the PCR amplification of Nb constructs.*

	Final concentration
5x Phusion HF Buffer	1X
10mM dNTPs	200µM
Forward primer (stock 10µM)	0.5µM
Reverse primer (stock 10µM)	0.5µM
Vector	5ng
Phusion DNA polymerase	0.02U/µL

PCR products were cleaned using a NZYTech cleaning kit (NZYGelpure-MB011) yielding clean Nb constructs. Concentration of each construct was determined by measuring the absorbance at 260 nm in the Nanodrop1000 (Thermo Fisher Scientific).

3.2.15.3. Replication of pUASTattB

Since the final carrier for the Nb constructs is the vector pUASTattB, a DNA replication was done to assure there was enough plasmid to work with, following the protocol explained above in Plasmid DNA replication/amplification (see Methods).

3.2.15.4. Digestion of Nbs and pUASattb

Double digestion conditions were evaluated at Thermo Fisher's website using the DoubleDigest Calculator. Digestion of the Nb constructs and the vector pUASTattB with EcoRI and NotI ran overnight at 37°C. The next day, the enzymes were inactivated (20min, 65°C) and the products of the enzymatic reaction were analysed in an agarose gel.

***Table 7** - Amounts utilized to digest the constructs and the vector following Thermo Fisher's recommendations.*

	µL	µL
Insert (x µg)	15	-
Vector (y µg)	-	3
Buffer O (10X)	2	5
EcoRI	1	1
NotI	0.5	0.5
miliQ H2O	1.5	41.5
Total	20	50
	NBs	Vector

3.2.15.5. Clean up enzymatic reaction products and DNA from agarose gel

Protocol for DNA purification from enzymatic reactions and DNA purification from agarose gels was followed as stated in the NZYTech cleaning kit (NZYGelpure-MB011). The final concentration was measured in the Nanodrop1000 (Abs at 260nm).

3.2.15.6. DNA Ligation

The Nb inserts were inserted in the pUASTattB vector using T4 DNA ligase (Thermo Fisher -EL0011). Following Thermo Fisher's protocol, 50 ng of vector were used and the rest of the reagents as follows (Table 8). A ratio of 1:3 was chosen and the amount needed of Nbs calculated in (http://www.insilico.uni-duesseldorf.de/Lig_Input.html).

***Table** 8 - Reaction mixture for DNA insert ligation into Vector DNA using T4 DNA ligase.*

Linear Vector DNA	20-100 ng
Vector : Insert DNA ratio	1:3
10X T4 DNA Ligase Buffer	2 µL
T4 DNA Ligase	1 U
H2O	to 20 µL

Calculations to determine how much of the Nbs inserts was needed to add, were done in an online calculator [196]. The program calculates the best vector:insert ratio based on:

$$\frac{\text{ng of vector} \times \text{kb size of insert}}{\text{kb size of vector}} \times \text{molar ratio of } \frac{\text{insert}}{\text{vector}} = \text{ng of insert}$$

DNA ligation was tried out two different times with different reaction times: 2 hours at 22°C or overnight at 16°C.

3.2.15.7. Cell transformation

After establishing the final plasmid (pUASTattB with Nb insert), DH5α cells were transformed with the plasmid (see protocol detailed in Methods) and the vector harvested from the cells for: 1 – sequencing, to confirm that ligation was done successfully and the Nbs nucleotide sequence suffered no mutagenesis during amplification and 2 – cutting and analysing in agarose gel, to confirm the presence of both the carrier and the insert, for each Nb.

3.2.16. Agarose Gel analysis

This technique is used for the separation and analysis of DNA fragments by size in an agarose matrix. The gel can be then viewed with stain under UV light and the DNA fragments can be excised, cleaned, and saved from the gel with relative ease. The percentage of agarose in the gel depends on the range of sizes of the fragments we are aiming to separate and analyse.

***Table** 9 – Percentage of agarose in the gel according to the fragment size being studied (Left). TAE buffer composition (Right).*

Fragment size (bp)	% Agarose (in TAE)
1-23.000	0.6
800-10.000	0.8
400-8.000	1
300-7.000	1.2
200-4.000	1.5
100-3.000	2

TAE 50X	TAE 1X
2M Tris acetate	40mM Tris acetate
0.05M EDTA	1mM EDTA
pH 8.2-8.4	

Agarose was weighed and added to 50mL of TAE 1X. The mixture was heated and dissolved. Red Safe stain was used as an alternative to the traditional ethidium bromide (1.2 µL per 50mL of TAE 1X). Electrophoresis was made in Buffer TAE 1X, 100V per gel of 0.8% to 1.2%. Samples were prepared by adding 1 volume of 6x ORANGE DNA loading dye (Thermo Fisher #R0631) to 5 volumes of DNA sample. 5µL of DNA ladder GeneRuler 1kb plus (Thermo Fisher) were used. The gel was visualized under UV light and an image was generated using ChemiDoc™ XRS (Bio-Rad).

3.2.17. Sequencing

DNA Sequencing was done to confirm DNA ligation products and can also be routinely done to confirm the nucleotide sequences we are working with, to assure the sequence remains unaltered.

Following the protocol from LIGHTRUN – GATC Biotech, 5µL of the appropriate primer (5 pmol/µL) were added to 5 µL of template DNA (80-100 ng/µL of plasmid) in a 1.5 mL tube and samples were shipped for sequencing.

3.2.18. Drosophila maintenance

Fly stocks were maintained on standard culture medium (To 7.5L: 62.5g agar, 500g corn flour, 62.5 g soy flour, 112.5 g yeast, 125 g malt extract, 210 mL molasses, 6.25 g Nipagin, 5 mL phosphoric acid and 45.5 mL propionic acid, in autoclaved water), at 18ºC. Fly crosses were performed on an enriched medium (To 7.5 L: 56.3 g agar, 375 g wheat flour, 750 g yeast, 750 g sugar, 6.25 g Nipagin + ethanol, 37.5mL propionic acid, in autoclaved water with liquid yeast). Fly crosses were maintained in bottles or vials at 25ºC, or 29ºC whenever experiments required highest expression levels of GAL4 protein.

All fly stocks used in this work were propagated on standard food and maintained at 25ºC and 29ºC; The composition of the fly food is presented below in Table 10.

Table 10 - Composition of the fly food

Food for stock maintenance		
Components	**V_f=7.5L**	**T (ºC)**
H_2O	3.25L	70
Agar	62.5g	80-85
Corn flour	500g	99
Soya flour	62.5g	
Yeast	112.5g	
Malte extract	125g	
Molasses	210mL	
Nipagin + EtOH	6.25g	51
Phosphoric acid	2.5mL	
Propionic acid	45.5mL	

Food for crosses		
Components	**V_f=7.5L**	**T (ºC)**
Sugar	750g	110
Yeast	750g	
Agar	56.3g	
Cornmeal	375g	
Propionic acid	37.5mL	65
Nipagin	188mL	

Chapter 4

Results and Discussion

4.1. Expression and purification of Atx3 variants and Nanobodies

The purity and homogeneity of a protein sample is crucial for various biochemical and biophysical studies. Carefully purifying the proteins, will assure that the follow-up characterization of protein structure and function reports to the isolated protein and not to additional contaminants. Large quantities of pure protein are needed for crystallization when seeking to obtain a 3D structure through X-Ray Diffraction. The purification strategy is based on the fractionation of the initial sample using various biochemical and biophysical properties to be able to separate our target protein from all other unwanted components. It is assumed that in optimized processes, protein activity is not lost. When fractionating, contaminants are removed, and fractions can be enriched with the protein of interest.

The Nbs carry an amino acid sequence that leads them to the bacterial periplasm (between the inner and outer membranes), whose contents can be easily obtained upon osmotic shock. Because the periplasmatic space does not have a significant number of host proteins, Nbs will be enriched in the overexpressed protein content less contaminants will be present. Additionally, the Nbs possess a histidine tag to allow binding to the nickel ions present in the chromatography columns used for purification. Even though there may be other naturally occurring proteins in the expression host cells with histidines, they are probably hidden in the 3D structure, and will not bind strongly to the nickel affinity chromatography columns. In the case of Atx3, which also integrates a histidine tail, it is necessary to lyse the cells because the overexpressed protein remains in the cell cytoplasm. The lysate contains several proteins and that is why a two-step elution with imidazole is done to first remove the low affinity binding contaminants (50mM imidazole) and then elute Atx3 (250mM imidazole).

Normal and expanded variants of Atx3 were expressed in BLS21 *E. coli* and purified by metal affinity chromatography followed by size-exclusion chromatography (SEC) as detailed above (see Methods). The protein was eluted from the Ni^{2+}-charged Histrap column with a stepwise variation of the concentration of imidazole (Figure 23A and Figure 24A). Fractions eluted with 250mM were further purified by SEC to remove remaining contaminants and possible Atx3 aggregates that normally form during the process of expression and purification. The different oligomeric species of Atx3 elute at different volumes since they have different molecular weights (Figure 23B and Figure 24B). SDS-PAGE analysis was done in parallel with samples from the different steps of the purification process to confirm purity and demonstrate that the percentage

of contaminants was consistently reduced (Figure 23D and Figure 24D). The SEC profile allowed to clearly see the formation of aggregates that occurs during the expression and purification process, as expected, since the presence of the polyQ tract potentiates aggregation.

Nanobodies NB06, NB11, NB15, NB16 and NB19 were expressed on WK6 (su-) *E. coli* cells following the protocol previously described in Methods. In contrast to Atx3, Nbs were purified with a single elution step with 300mM of imidazole in the Ni^{2+}-charged Histrap (Figure 25A, C, E and G) followed by SEC (Figure 25B, D, F and H). A large-scale purification was done for NB20, involving a SEC using a Hiprep 26/60 Sephacryl S-100 HR column (GE – Healthcare Life Science), prior to crystallization assays (Figure 25I and J). The purity of the protein samples was analysed by SDS-PAGE (Figure 25K to O). The purity of all the Nbs used in this work was analysed by SDS-PAGE gel (Figure 26).

Other Nbs had already been purified (NB03, NB06, NB07, NB12, NB13, NB14 and NB17) by the host lab and were used in the following assays.

Atx3

13Q

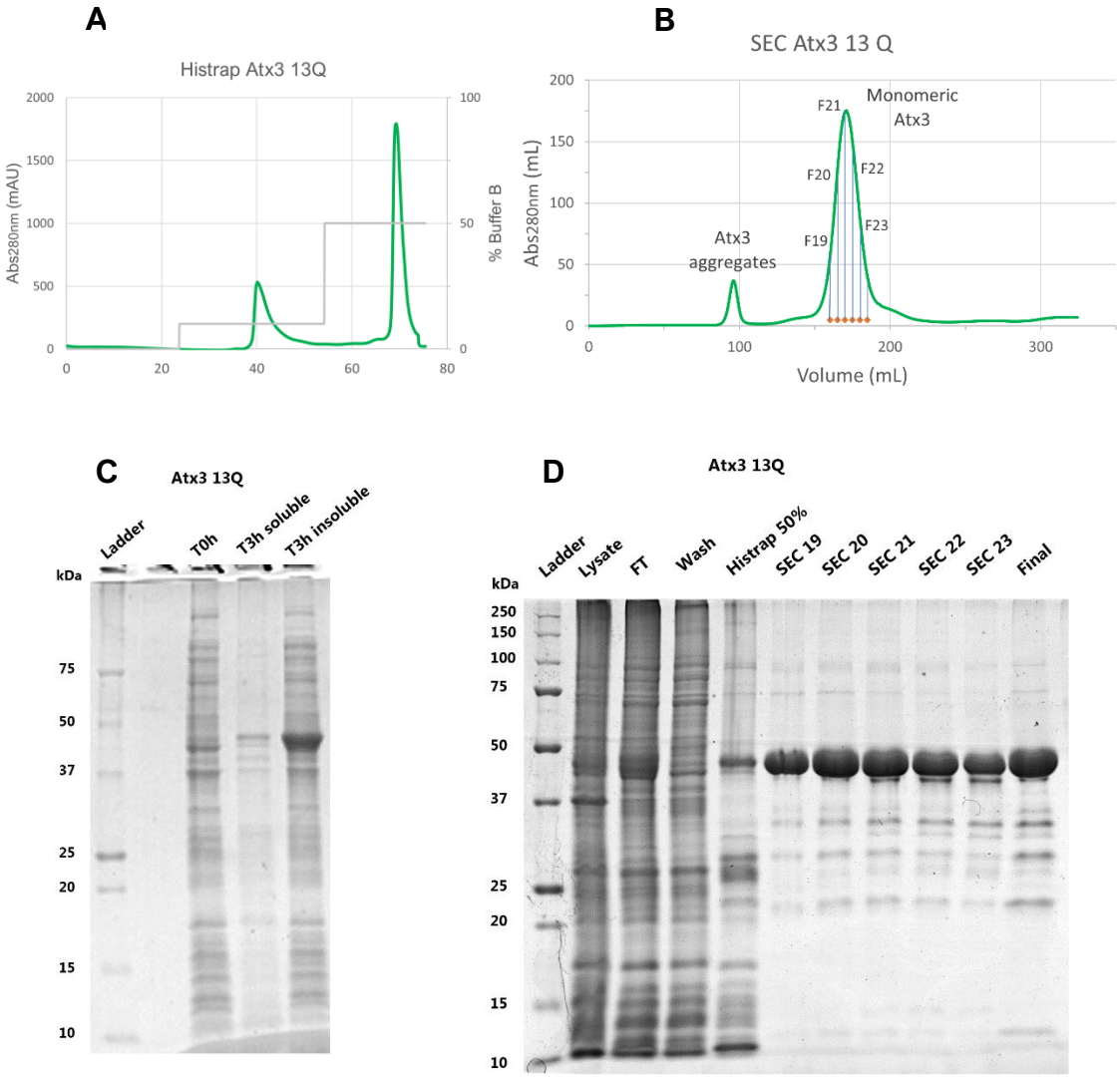

Figure 23 *– Purification process of Atx3 13Q.* ***(A)*** *Ni2+ charged Histrap Atx3 13Q elution profile with two steps, first with lower imidazole concentration (50 mM, 10% buffer B) and then with an increased concentration of imidazole (250 mM, 50% buffer B) (grey line – right axis). Protein elution was detected by monitoring the absorbance at 280 nm (left axis).* ***(B)*** *The selected fractions from the Histrap were pooled, concentrated, and injected into a size exclusion chromatography column (HiPrep 26/60 Sephacryl S-300 HR column) where the protein elution could be observed by monitoring the absorbance at 280 nm. Fractions 19 to 23, correspond to the lowest molecular weight Atx3 species, presumably monomeric.* ***(C)*** *SDS-PAGE analysis of the expression of recombinant Atx3 by E. coli. Atx3 is found on the soluble portion after expression (T3h) if lyse of the cells is successful.* ***(D)*** *SDS-PAGE was used to monitor the sample purity throughout the purification process.*

77Q

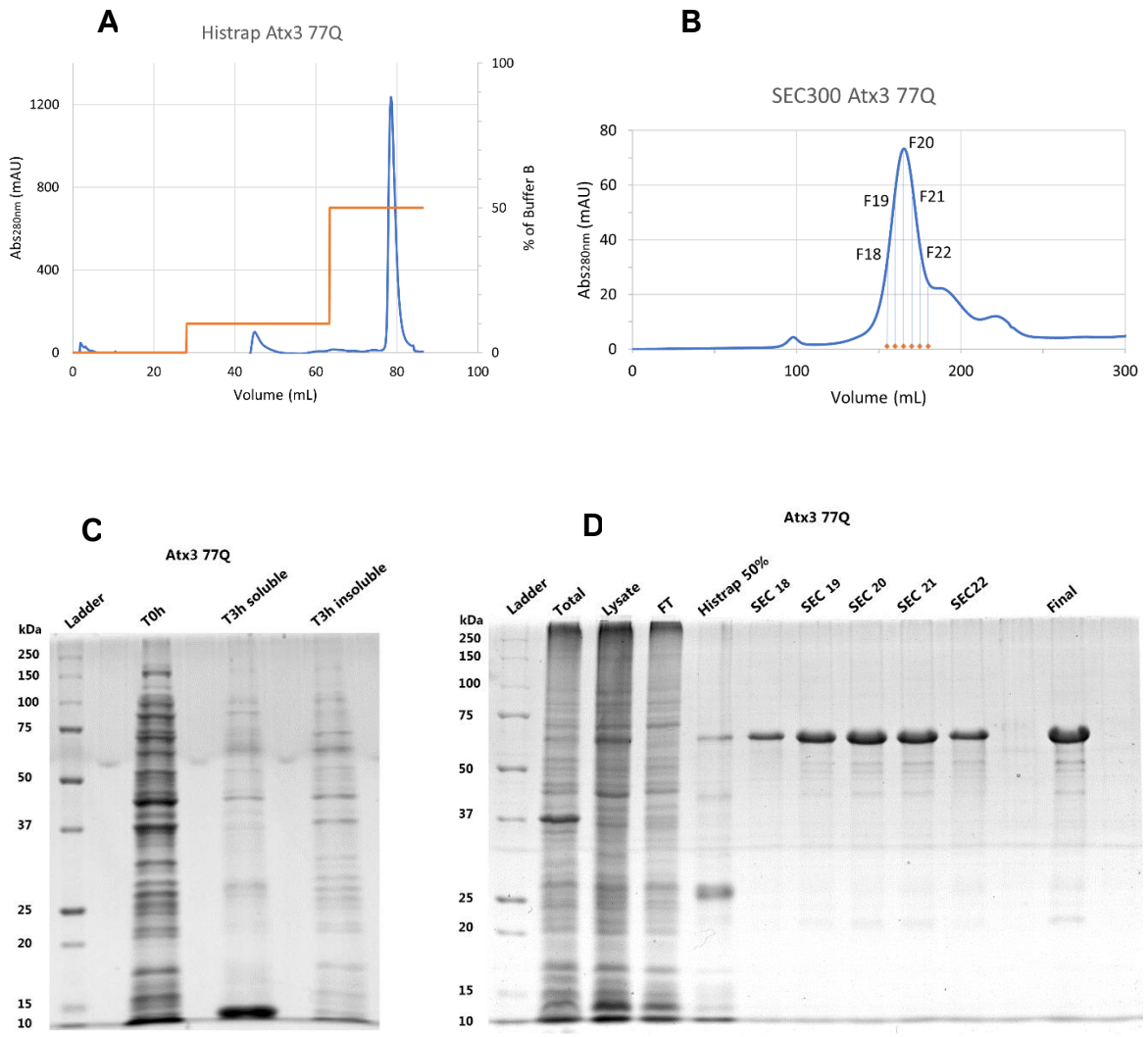

Figure 24 *– Purification process of Atx3 77Q.* ***(A)*** *Ni2+ charged Histrap Atx3 77Q elution profile with two steps, first with lower imidazole concentration (50 mM, 10% buffer B) and then with an increased concentration of imidazole (250 mM, 50% buffer B) (orange line – right axis). Protein elution was detected by monitoring the absorbance at 280 nm (left axis).* ***(B)*** *The selected fractions from the Histrap were pooled, concentrated, and injected into a size exclusion chromatography column (HiPrep 26/60 Sephacryl S-300 HR column) where the protein elution could be observed by following monitoring the absorbance at 280 nm. Fractions 19 to 23, correspond to the lowest molecular weight Atx3 species, presumably monomeric.* ***(C)*** *SDS-PAGE analysis of the expression of recombinant Atx3 by E. coli. Atx3 is found on the soluble portion after expression (T3h) if lyse of the cells is successful* ***(D)*** *SDS-PAGE was used to monitor the sample purity throughout the purification process.*

Nanobodies

NB11

A

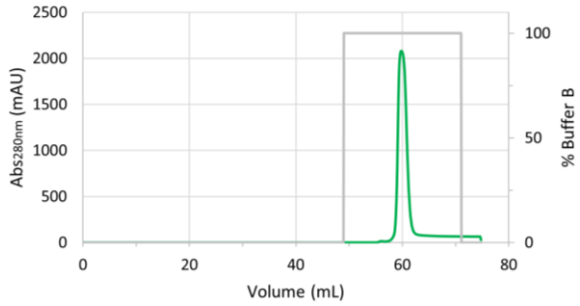

B

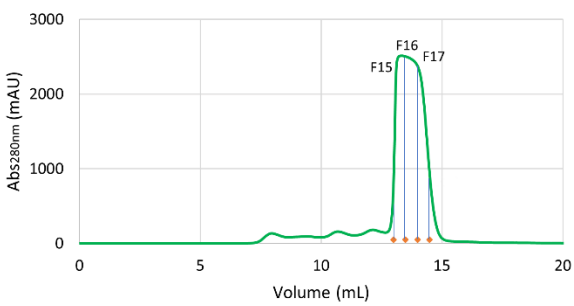

NB15

C

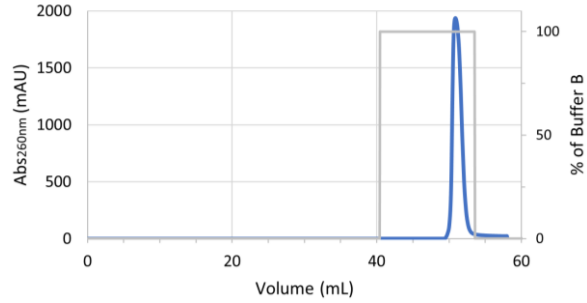

D

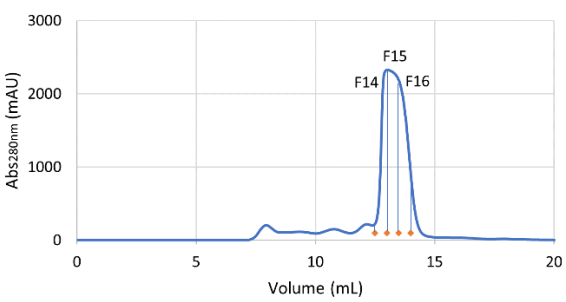

NB16

E

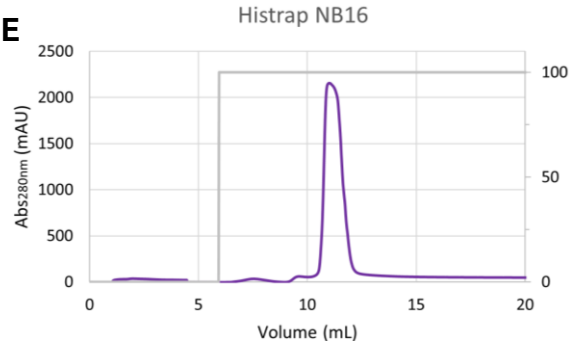

F

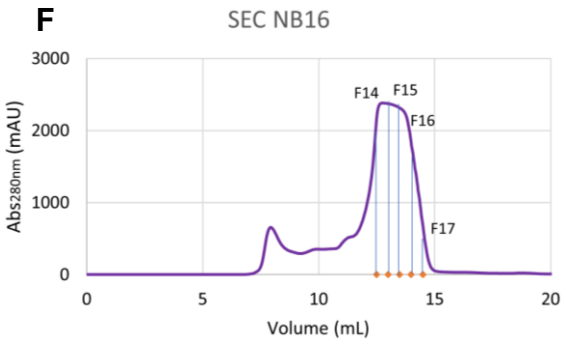

NB19

G

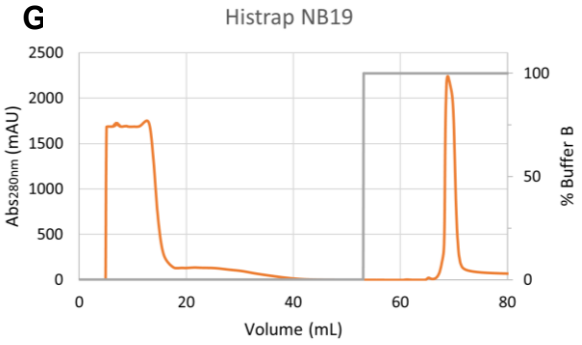

H

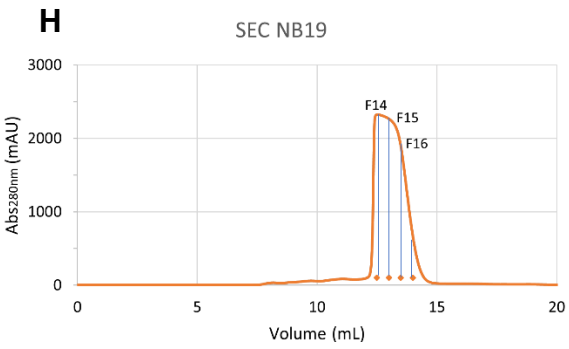

NB20

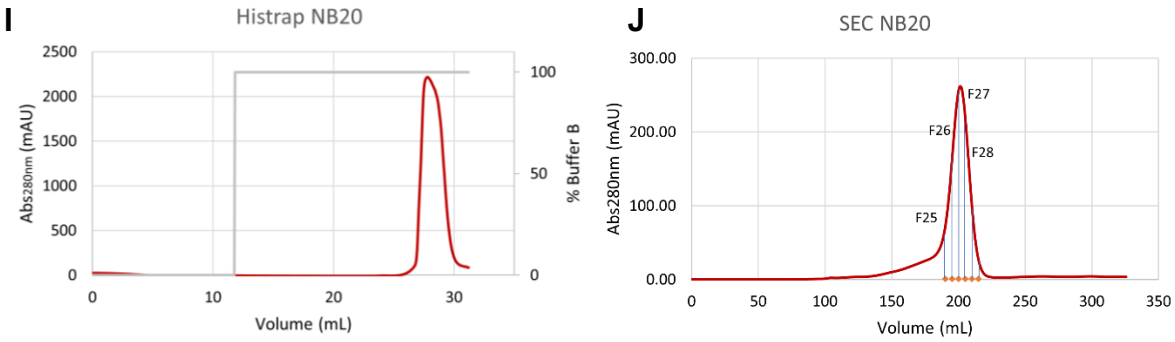
I
Histrap NB20
Abs280nm (mAU)
% Buffer B
Volume (mL)
J
SEC NB20
Abs280nm (mAU)
F25
F26
F27
F28
Volume (mL)

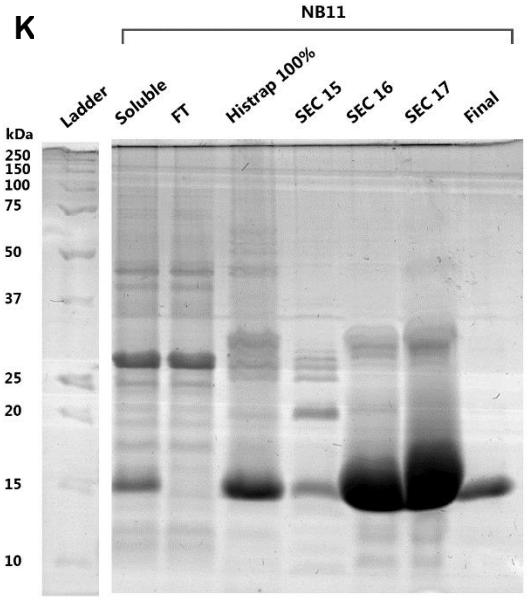
K
NB11
Ladder
Soluble
FT
Histrap 100%
SEC 15
SEC 16
SEC 17
Final
kDa
250
150
100
75
50
37
25
20
15
10

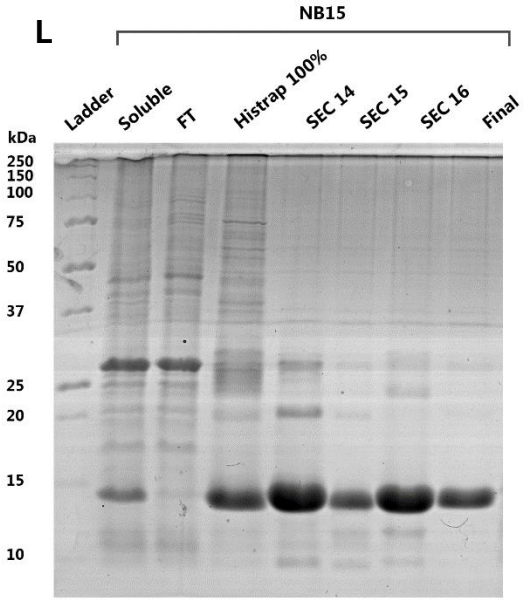
L
NB15
Ladder
Soluble
FT
Histrap 100%
SEC 14
SEC 15
SEC 16
Final
kDa
250
150
100
75
50
37
25
20
15
10

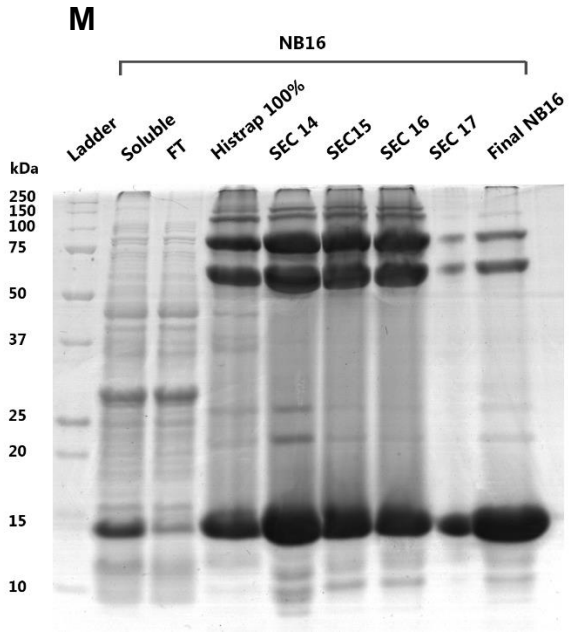
M
NB16
Ladder
Soluble
FT
Histrap 100%
SEC 14
SEC15
SEC 16
SEC 17
Final NB16
kDa
250
150
100
75
50
37
25
20
15
10

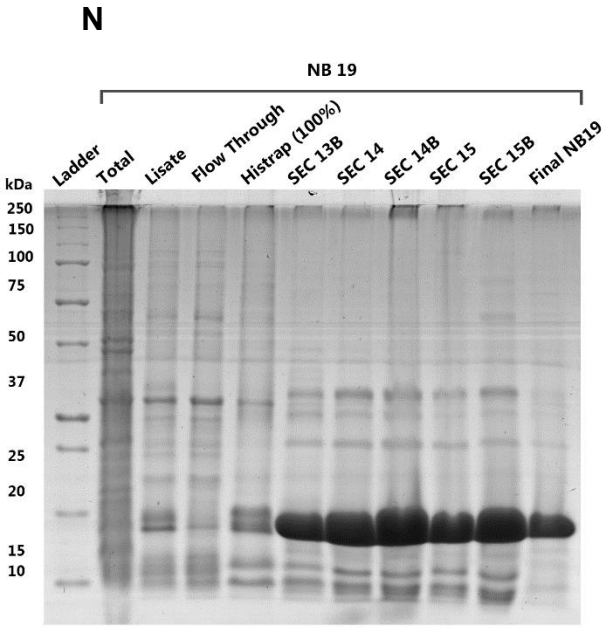
N
NB 19
Ladder
Total
Lisate
Flow Through
Histrap (100%)
SEC 13B
SEC 14
SEC 14B
SEC 15
SEC 15B
Final NB19
kDa
250
150
100
75
50
37
25
20
15
10

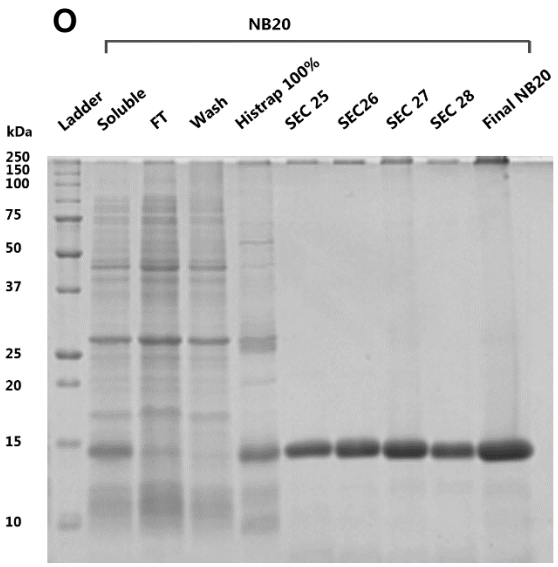

Figure 25 *– Purification process of Nbs.* ***(A, C, E, G, I)*** *- Ni2+ - charged Histrap chromatography profile showing a single elution step with 100% buffer B (300 mM Imidazole) (grey line) of Nbs NB11, NB15, NB16, NB19 and NB20, respectively.* ***(B, D, F, H)*** *- Size exclusion chromatography profile with corresponding fractions selected. Protein was detected by monitoring the absorbance at 280 nm.* ***(J)*** *– Size exclusion chromatography profile of Large-Scale purification of NB20.* ***(K to O)*** *- SDS-PAGE analysis of the purification steps of each Nb (Lysis, Flowthrough, (in some cases) Wash, Ni2+ - charged Histrap pooled fractions, SEC fractions and final concentrated protein). SEC performed with SUPERDEX 75 10/300 GL column.*

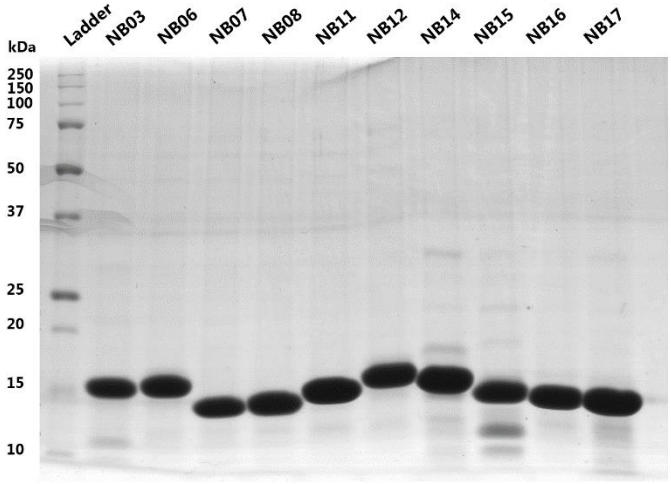

Figure 26 *– SDS-PAGE analysis of the molecular weight (MW) of the Nbs used in this work. Theoretical MWs (in Da) are as follows: NB03 - 15091.62; NB06 - 14919.55; NB07 - 13922.5; NB08 - 13881.51; NB11 - 14944.62; NB12 - 14977.58; NB14 - 15144.79; NB15 - 14072.7; NB16 - 13950.66; NB17 - 14019.55. NB13 is missing since there was no sample left from the batch used.*

4.2. Nanobodies have high thermal stability:

4.2.1. Thermal Shift Assay

The thermal stability of candidate Nbs was determined by measuring their melting temperature (Tm) in a thermal shift assay. The Tm is the temperature at which 50% of the protein is denatured. Using SYPRO Orange dye is an advantage because, due to its fluorescence properties ($\lambda_{excitation}$ 470nm, $\lambda_{emission}$ 570nm), it can be monitored in a real-time Polymerase Chain Reaction (PCR) instrument, commonly found at the laboratory, making use of these instruments to measure thermal stability. The dye binds non-specifically to hydrophobic regions of the proteins. Upon denaturation, these regions are gradually exposed allowing dye binding, leading to an increase in fluorescence readout. The T_m can readily be determined by plotting the raw data's first derivative and finding its minimum (Figure 27). Each of the results corresponds to a mean of experimental triplicates.

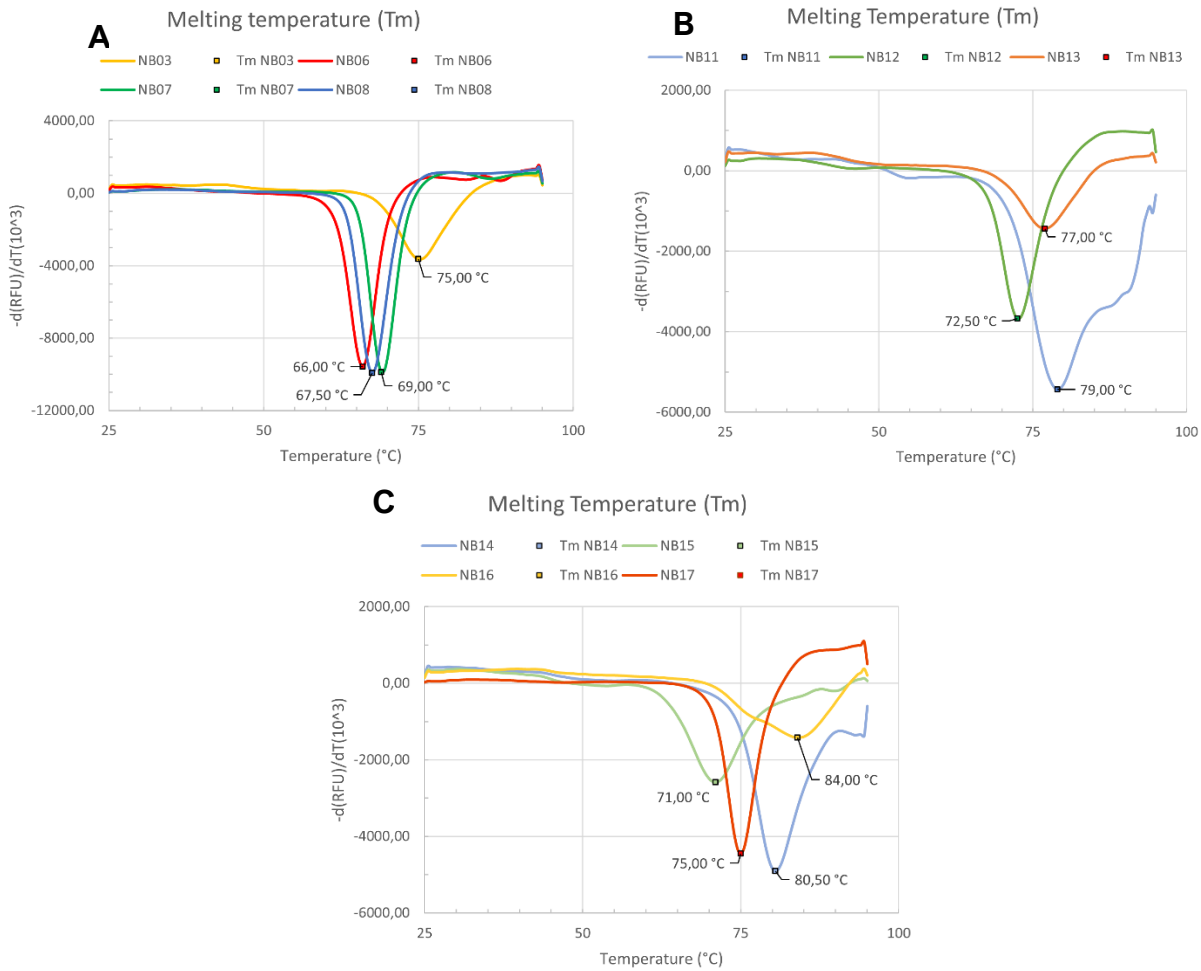

Figure 27 *- Thermal Shift Assay with NB03, NB06, NB07, NB08, NB11, NB12, NB13, NB14, NB15, NB16 and NB17. Melting temperatures were analysed by measuring the emission of SYPRO Orange fluorophore with temperature. First derivative was plotted.* ***(A)*** *NB03 – yellow line; NB06 – red line; NB07 – green line; NB08 – blue line* ***(B)*** *NB11 – light blue line; NB12 – green line; NB13 – orange line* ***(C)*** *NB14 – blue line; NB15 – green line; NB16- yellow line; NB17 – orange line.*

Overall, all nanobodies present high thermal stability, ranging from 66ºC (NB06) to 84°C (NB16), with a median of 75ºC (Table 11). This is advantageous for experimental procedures that might endure higher temperatures.

Further information could have been obtained about how interaction of the Nbs with Atx3 changes thermal stability of the complex and in what direction. However, from previous studies conducted by the host lab, with other Nbs interacting with Atx3, it seems the complex is disassembled as temperature rises and before both proteins start denaturing. Therefore, the effect in thermal stability of Atx3 in a complex with a Nb will not really be seen.

Table 11 *- Summary of melting temperatures of NB03, NB06, NB07, NB08, NB11, NB12, NB13, NB14, NB15, NB16 and NB17.*

Nanobody	Melting Temperature (°C)
NB03	75
NB06	66
NB07	67.5
NB08	69
NB11	79
NB12	72.5
NB13	77
NB14	80.5
NB15	71
NB16	84
NB17	75

4.3. Nanobodies interact with Atx3

4.3.1. Screening for Atx3:Nb complex formation by native-gel electrophoresis

Native gel analysis was performed to evaluate if nanobodies interact with Atx3, forming complexes. Upon non-denaturing conditions, the Atx3:Nb complexes migrate with different properties from the isolated proteins and a shift in gel migration is expected upon complex formation.

The native-gel analysis showed that all the tested Nbs, except NB03, form a complex with Atx3 13Q and 77Q (Figure 28). Clear band shifts are observed in the presence of NB06, NB07, NB08, NB11, NB12, NB13, NB14, NB15, NB16 and NB17.

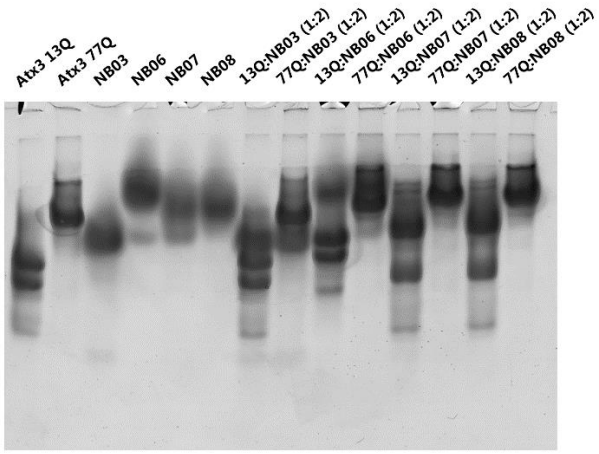

Native Gel 1

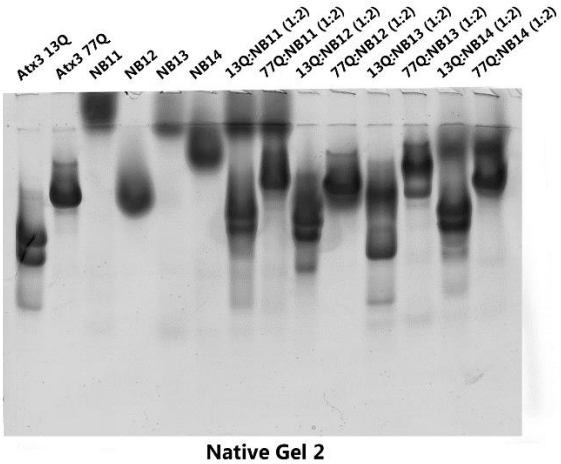

Native Gel 2

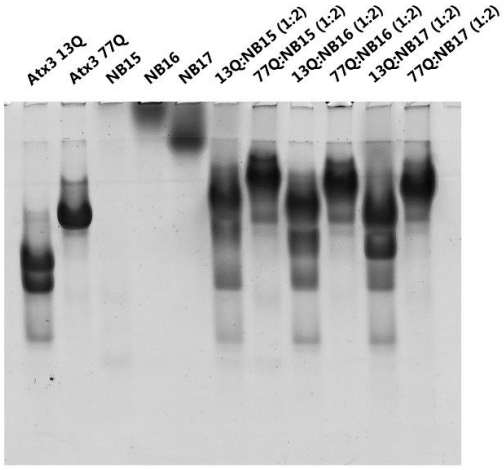

Native Gel 3

Figure 28 *- Native-polyacrylamide gel electrophoresis (Native-PAGE) analysis of purified Atx3 13Q, Atx3 77Q, Nbs and Atx3:Nb complexes followed by Blue Safe staining.* ***Native gel 1*** *shows the analysis of complex Atx3 13Q:NB03, Atx3 13Q:NB06, Atx3 13Q: NB07, Atx3 13Q:NB08, Atx3 77Q:NB03, Atx3 77Q:NB06, Atx3 77Q:NB07 and Atx3 77QNB08.* ***Native gel 2*** *shows the analysis of complex Atx3 13Q:NB11, Atx3 13Q:NB12, Atx3 13Q:NB13, Atx3 13Q:NB14, Atx3 77Q:NB11, Atx3 77Q:NB12, Atx3 77Q:NB13 and Atx3 77Q:NB14.* ***Native gel 3*** *shows the analysis of complex Atx3 13Q:NB15, Atx3 13Q:NB16, Atx3 13Q:NB17, Atx3 77Q:NB15, Atx3 77Q:NB16 and Atx3 77Q:NB17.*

4.4. Nanobodies modulate Atx3 self-assembly

To address the impact of the Nbs in the aggregation of Atx3, several experiments were conducted in parallel with the same batch of each protein. Amyloid formation was monitored by ThioT fluorescence assay and filter retardation assay. The morphology of the aggregates and fibrils was visualized by TEM, oligomeric species detected by dot-blot assay and information of the oligomerization kinetics was assessed by SEC. Before each aggregation assay, Atx3 is repurified to exchange the buffer to the aggregation buffer (without glycerol, which delays aggregation) and to remove possible Atx3 aggregates and intermediate oligomeric species in solution. A representative repurification SEC profile is presented for Atx3 13Q and Atx3 77Q where it is evident that different variants elute at different volumes due to size differences.

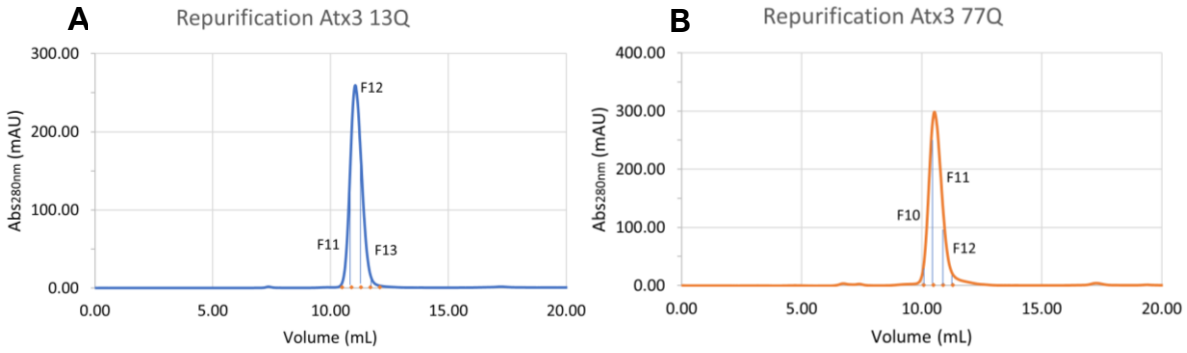

Figure 29 *– Size exclusion chromatography representative profiles of the repurification of* ***(A)*** *Atx3 13Q and* ***(B)*** *Atx3 77Q. Buffer exchange from purification Atx3 SEC buffer to Aggregation buffer. Pooled fractions are highlighted. SEC performed with SUPEROSE 12 10/300 GL column.*

4.4.1. Thioflavin T aggregation assay

Thioflavin T fluorescence is widely used to mark the presence of amyloid fibrils both *in vivo* and *in vitro*. It is however not a specific stain, spotting diverse types of fibrillar and non-fibrillar multimeric assemblies. Studies found that it is not only the conformation adopted by ThioT upon binding to amyloid fibrils that results in an enhancement of fluorescence, but other conformations caused by binding to different biomolecules may lead to this augmentation as well [197]. This is just something that should always be considered when analysing results and designing this type of experiment.

An Atx3 aggregation assay monitored by ThioT was conducted to analyse the influence of Nbs in the readout of fluorescence (Figure 30). The ratios between proteins and molar concentrations used are based on experimental results previously optimized for Atx3 by the host lab. Three replicates were used for each sample and the standard deviation calculated and shown in Figure 30.

Amyloid fibril formation, including for Atx3 shows sigmoidal growth kinetics [198]. Atx3 13Q and 77Q alone display a lag phase of aggregation of about 20 and 18 hours,

respectively (Figure 30). Overall, Nbs alter the kinetics of aggregation monitored by ThioT binding. All nanobodies apparently extended the lag-phase of aggregation of both variants of Atx3 to an average of ~40 hours (Figure 30). The effect of the presence of the nanobodies is stronger (reduction in fluorescence read-out) for Atx3 13Q. The maximum fluorescence is reduced for Atx3 77Q when incubated with nanobodies NB06, NB08, NB11, NB12, NB13, NB14, NB15, NB16 and NB17 (Figure 30). For the timeframe of this assay, cases where the growth kinetics reaches a plateau state, species in solution are theoretically in equilibrium. From a decrease in the maximum of fluorescence it can be proposed that concentration of fibrils is lower, or that a degradation of the protein is occurring, although other species might be present in higher concentrations, in comparison with the control. NB15 and NB13 are the Nbs which have a more significant effect on Atx3 aggregation monitored by ThioT fluorescence for Atx3 13Q and Atx3 77Q, respectively. Generally, these preliminary conclusions are subjected to repetition ensuring all proteins used are pure and monomeric upon incubation. Additionally, nanobodies alone should also be monitored as a control to understand the effect they have in the fluorescence read-out.

4.4.2. Filter retardation assay

To address how Nbs impede or delay the formation of Atx3 77Q mature SDS-resistant amyloid fibrils, a filter retardation assay was conducted utilizing the endpoint samples from the ThioT aggregation assay. As explained, this assay allows to retain the Atx3 77Q SDS-resistant aggregates in the membrane, while soluble species pass through the 0.22 μm pore of the cellulose acetate membrane [199].

Although there are fewer SDS-insoluble aggregates in the presence of nanobodies NB07 and NB13, these do not impede the formation of mature fibrils at the endpoint of aggregation (110 hours) (Figure 31). The triplicate lines for NB07 are not equal but it is possible to see there are some insoluble SDS fibrils present. Nanobodies NB06, NB11, NB12, NB14, NB15 and NB16 delay the formation of mature fibrils or stabilize other protein species impeding the formation of mature amyloid-like fibrils (Figure 31). Nanobodies NB08 and NB17 demonstrate a significant reduction in SDS-insoluble species (Figure 31). A, B and C correspond to experimental triplicates (Figure 31).

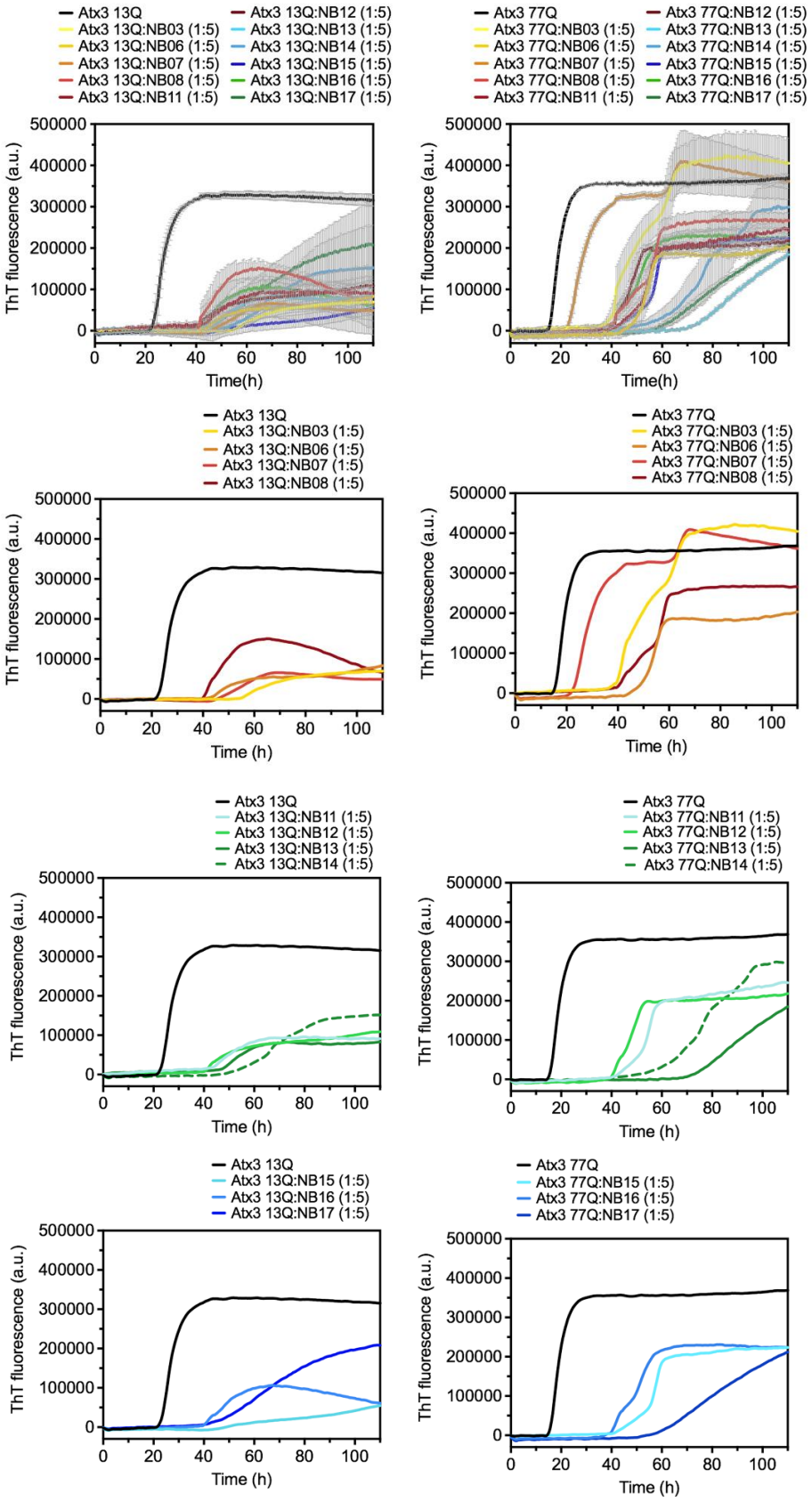

Figure 30 *- Thioflavin T aggregation assay results. The plots display the modulation of Atx3 variants' aggregation by NB03, NB06, NB07, NB08, NB11, NB12, NB13, NB14, NB15, NB16 and NB17 visualized by a ThT assay. The negative controls for Atx3 variants alone are shown. The labels indicate the samples analysed are shown above the corresponding graphic. Standard deviation is shown in the first two plots. The following plots were obtained by means of triplicates. Ratio of 1:5 (Atx3:NB).*

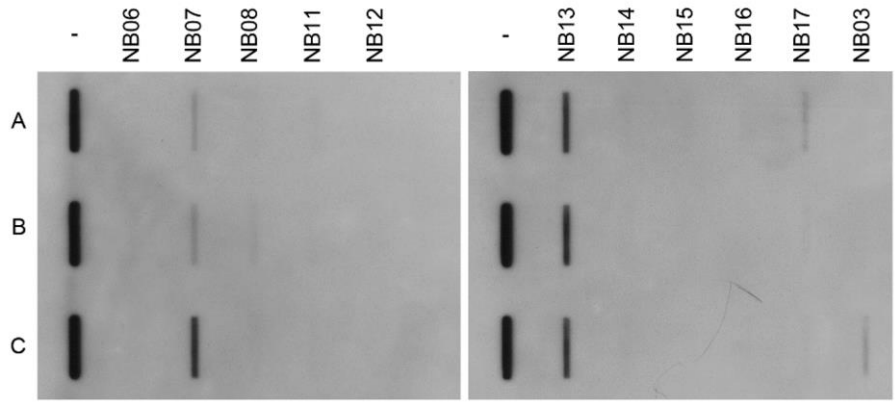

Figure 31 *- Filter retardation assay results to address nanobody influence in the formation of SDS-resistant mature amyloid-fibrils of Atx3 77Q. Nbs analysed are NB03, NB06, NB07, NB08, NB11, NB12, NB13, NB14, NB15, NB16 and NB17. Control for Atx3 77Q alone is labelled as (-). The signal is obtained by recognition of total protein in the membrane by antibody 1H9. A, B and C correspond to experimental triplicates.*

4.4.3. Dot-Blot assay

To evaluate what protein species were present at the endpoint of the aggregation assay in the presence of Nbs when compared to the control, an immunoblotting analysis was performed. As explained above (see Methods), this immunoblotting was done with antibodies that theoretically bind different oligomeric species that usually occur and are present at different times in the process of aggregation ultimately resulting in the formation of mature amyloid fibrils. Anti-Amyloid Oligomer A11 antibody (A11) recognizes specific conformational oligomers, that have been corelated to toxicity [189], [190]. Anti-Amyloid Fibrils OC antibody (OC) recognizes generic epitopes present in many amyloid fibrils and protofibrils (fibrillar oligomers), but not in native proteins or prefibrillar oligomers. Finally, Anti-Atx3 1H9 antibody (1H9) binds to the epitope at E214-L233 residues of Atx3, meaning it is useful to qualitatively establish the amount and presence of Atx3 in a sample (loading control).

Regarding A11 antibody, in the control, for both variants of Atx3 there are a considerate number of A11 positive species (Figure 32). Apparently, NB17 has no effect in the formation of oligomeric species recognized by A11 in both Atx3 variants. Normally, species recognized by A11 seem to be the more toxic species for other amyloidogenic proteins, however, this has not been confirmed for Atx3. NB06, NB11, NB12, NB15 and NB16 apparently inhibit the formation of Atx3 A11-positive species (Figure 32). These are the same Nbs that delayed the aggregation in the previous ThioT assay (Figure 30). NB13 and NB14 are peculiar, since they prevent the formation of A11-positive species only for non-expanded Atx3 and expanded Atx3, respectively. NB13 prolonged the lag-phase of aggregation of Atx3 77Q up to 70 hours in the ThioT assay (Figure 30). NB14 could be particularly interesting for future studies since it could modulate the aggregation of the expanded form of Atx3 with less impact on the behaviour of normal Atx3, since we do not yet know if interfering with the normal Atx3 will have negative results (in a cellular model or organism and ultimately the patient) by tempering with protein function. One should note that the overlap between the Nb

binding sites and the A11-binding sites could also result in a decrease of the A11 binding.

Not much can be concluded from the anti-amyloid fibrils OC antibody membrane probing, since it seems that not all A11 antibody was removed and may be impeding OC binding. Another reason may be that the binding of Nbs to Atx3 prevented antibody recognition of Atx3 by OC. Noting even that the same secondary antibody was used, there might still be some reading in the second probing of A11's activity. The same happens for the third probing, with anti-Atx3 1H9 antibody, where some Nbs may compete with the 1H9 antibody binding site to Atx3 and have higher affinity for Atx3. Additionally, there is the possibility of removal of protein sample from the membrane. 1H9 antibody would have allowed to detect the presence of Atx3.

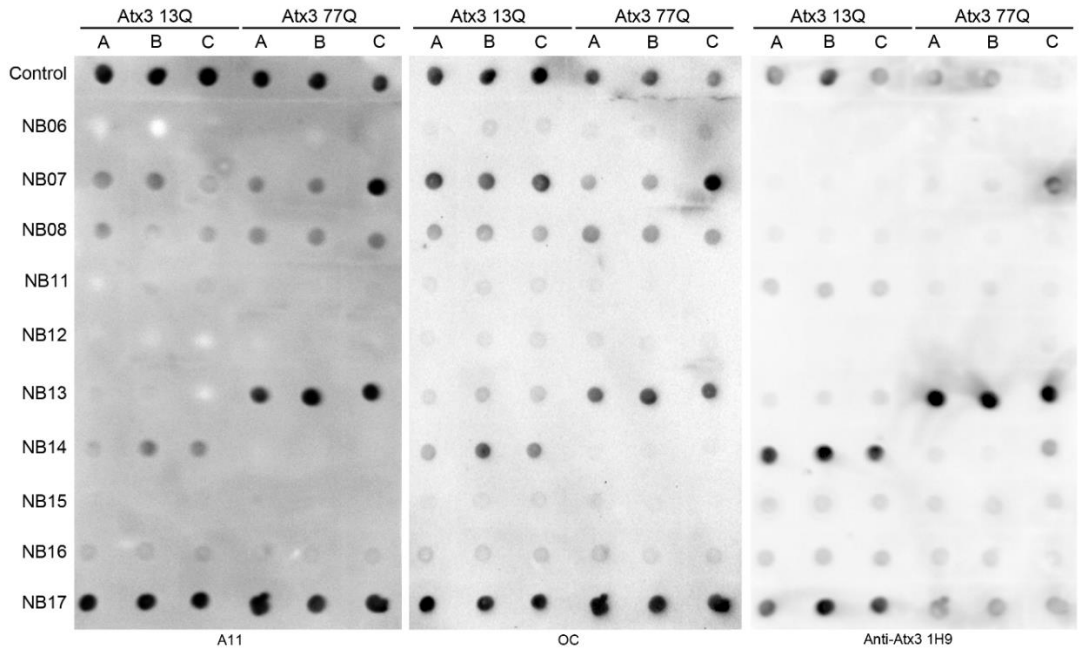

Figure 32 - Dot Blot assay results. The endpoint samples of ThT assay were used. Probing was done successively with Anti-Amyloid Oligomer A11 Antibody (that recognizes oligomeric species) followed by Anti-Amyloid Fibrils OC Antibody (that recognizes amyloid fibrils/protofibrils) and finally Anti-Atx3 1H9 Antibody (that recognizes the total Atx3 protein loaded). A, B and C are the three replicates of each condition as in the ThioT assay.

When making a correlation between ThioT results and dot-blot results it can be observed that when aggregation process reached the plateau phase, there was no longer an increase in the number of amyloid fibrils that bind to ThioT (Figure 30) but there were still A11-positive oligomeric species present (Figure 32). Further questions to address, would be at what point do the A11-positive species appear and if nanobodies cause a significative delay in the aggregation process: are they maintaining the presence and abundance of these species that may end up being more toxic than mature aggregates?

As explained, some issues may have happened in this assay, which makes it difficult to withdraw solid conclusions from the results obtained: two technical problems, one being the possibility of the washing and stripping steps removing part of the protein from the membrane and another in which not all A11 antibody (which was the first

probed antibody) was removed; it can also be that interaction between the Nbs and Atx3 impeded the interaction with OC and 1H9 antibodies. This assay would need to be repeated possibly doing the assay in two separate membranes, one for A11 and 1H9 control and another for OC and 1H9 control.

4.4.4. Transmission Electron Microscopy

To understand if nanobodies would change the morphology of the protein species formed during the elapsed aggregation time, TEM images of the endpoint (110 elapsed hours) samples from the ThioT aggregation assay were produced (Figure 33).

From the controls the formation of amyloid-like fibrils is observed for Atx3 77Q and the formation of protofibrils for Atx3 13Q. Mature fibrils were still observed in the presence of NB13 and NB07 with Atx3 77Q, results that go in line with the filter retardation experiment results (Figure 33). The overall morphology of the protofibrils changes in the presence of NB06 for both variants, when compared to the control. Even though mature fibrils are present for Atx3 77Q in the presence of NB07, the Nb seems to alter the morphology of the species when interacting with Atx3 13Q. In all other nanobodies, the process of aggregation seems to be delayed and that is also reflected in the morphology of the species observed by TEM, where the apparent size and number of fibrils is reduced. No mature fibrils of Atx3 77Q were observed for NB06, NB08, NB11, NB12, NB14, NB15, NB16 and NB17 indicating they might indeed delay the aggregation process.

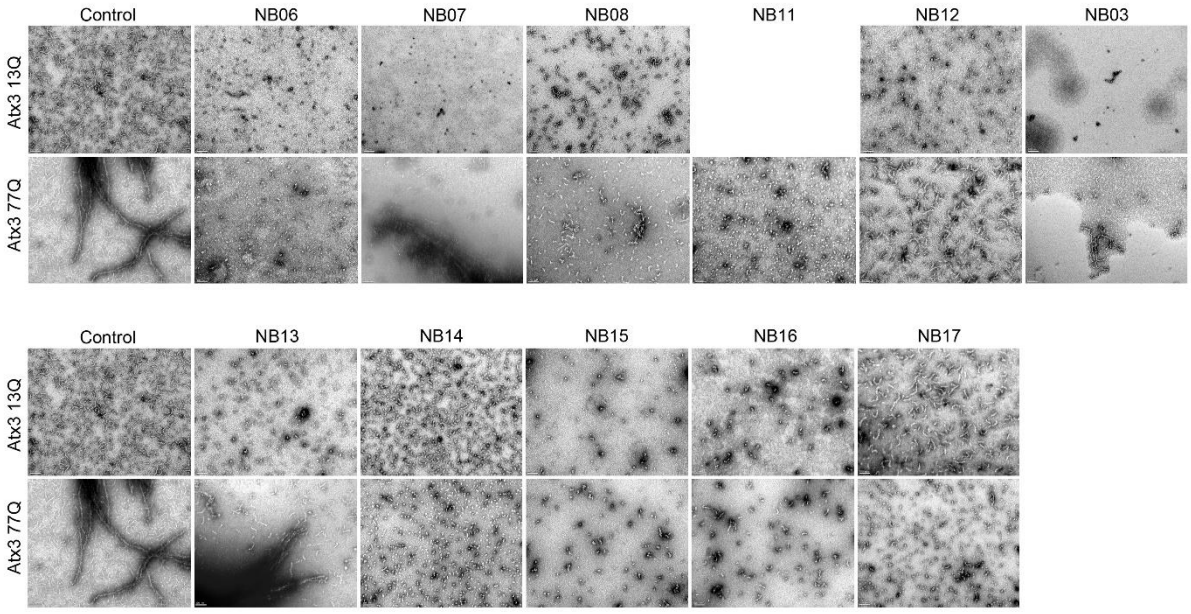

Figure 33 *- Transmission Electron microscopy images of Atx3 13Q and 77Q alone and incubated with the several Nbs, corresponding to the endpoint samples collected from the ThioT aggregation assay. 100000X magnification.*

An overall view of the results obtained are summarized in Table 12, regarding most important features of Nbs relative to Atx3 77Q.

4.4.5. Size exclusion Chromatography

Size exclusion chromatography (SEC) allows for a time-course analysis of the aggregation of Atx3 and to investigate how this process is modified in the presence of Nbs. A protein aggregation model monitored by SEC was validated for Atx3, confirming that the formation of high-order aggregates depletes the concentration of smaller species to levels below detection limit in a time period of 80 hours [64].

To complement all previous assays, monitoring of aggregation through SEC was performed according to the previously explained method (see Methods**)**, incubating Atx3 13Q and 77Q with NB06 and NB15. Due to protein degradation, corresponding SEC profiles were altered from normal protein behaviour, making it impossible to complete this assay (data not shown). SDS-PAGE analysis done with samples from the time-points evaluated (0h, 17h, 47h, 68h and 90h) shows gradual protein degradation of all samples (Atx3 13Q, Atx3 13Q:NB06, Atx3 13Q:NB15, Atx3 77Q, Atx3 77Q:NB06 and Atx3 77Q:NB15) and how Nbs may stabilize the protein for a longer period (Figure 34). This experiment needs to be repeated, including NB16.

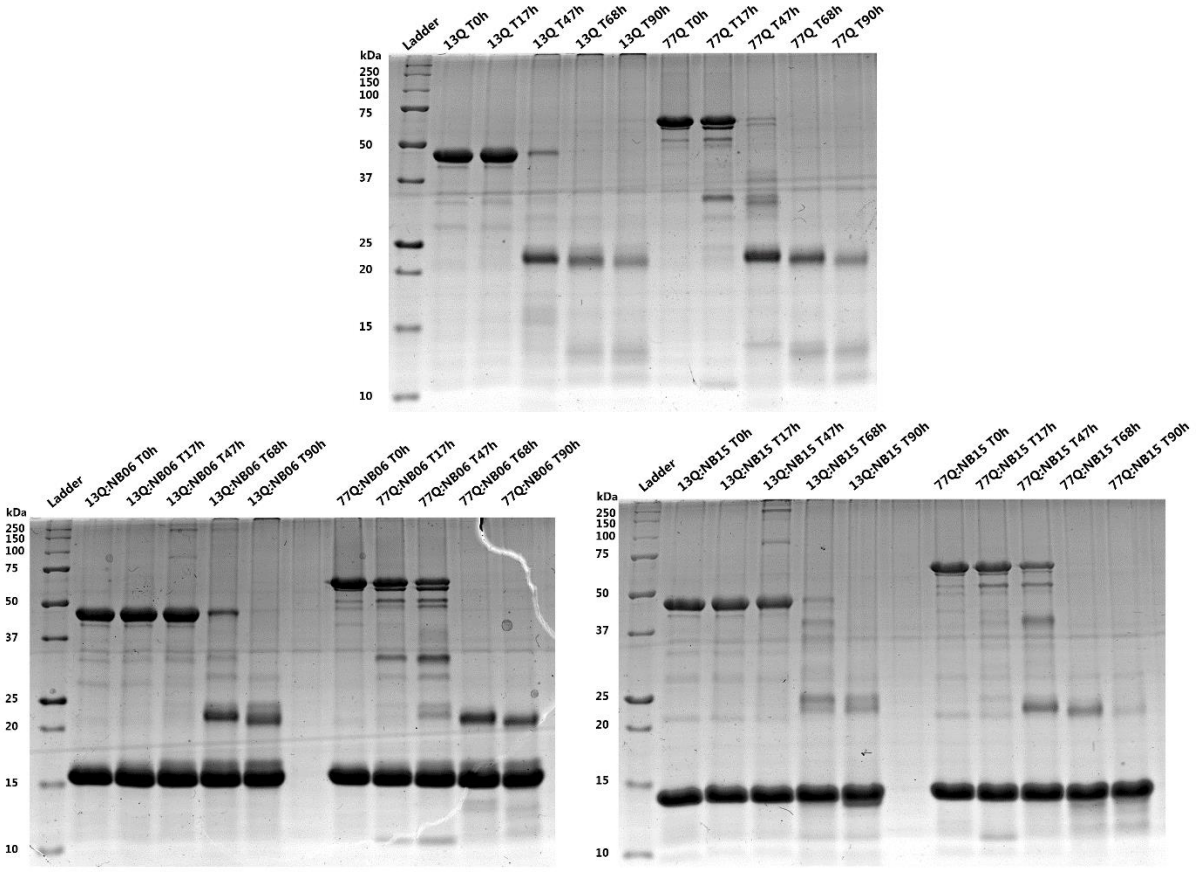

Figure 34 *– SDS-PAGE analysis of the time-course analysis by size exclusion chromatography of the aggregation of Atx3. The top-left gel shows Atx3 13Q and Atx3 77Q purity and integrity over the course of 90 hours. The top-right gel shows the purity and integrity of Atx3 13Q and Atx3 77Q incubated with NB06 over the course of 90 hours. The bottom gel shows the purity and integrity of Atx3 13Q and Atx3 77Q incubated with NB15 over the course of 90 hours. SEC performed with SUPERDEX 200 increase 5/150 GL column.*

Table 12 *– Summarized results of Nb effect on the aggregation of Atx3 77Q, at the endpoint of aggregation. It is addressed the extension of the lag-phase and reduction of the maximum fluorescence registered by the ThioT assay; A11 antibody-positive species; apparent reduction in the number of fibrils.*

	Lag-phase extension	Reduced max. fluorescence	A11-positive	(apparent) Reduction of the amount of fibrils
NB06	✔	✔		✔
NB07			✔	
NB08	✔	✔	✔	✔
NB11	✔	✔		✔
NB12	✔	✔		✔
NB13	✔	✔	✔	
NB14	✔	✔		✔
NB15	✔	✔		✔
NB16	✔	✔		✔
NB17	✔	✔	✔	✔

4.5. Impact of Atx3:Nb molar ratio on Atx3 aggregation dynamics

To understand how the molar ratio of Atx3:Nb affected the Nbs' influence in the aggregation, the NB11, NB15 and NB16 that delayed aggregation and abolished the formation of A11-positive species were chosen. The same assays (ThioT aggregation assay, filter retardation assay, dot-blot assay and TEM images) were therefore performed incubating Nbs with Atx3 77Q, using the same protein batches.

4.5.1. Thioflavin T aggregation assay

Once again, all nanobodies prolonged the lag-phase of the aggregation kinetics (Figure 35). NB11, NB15 and NB16 delayed the aggregation of Atx3 77Q at a molar ratio of 1:5, 5μM Atx3 to 25μM Nb, and 1:10, 5μM Atx3 to 50μM Nb. The molar ratio of 1:2, 5μM Atx3 to 10μM Nb, for all tested Nbs initially extended the lag-phase, delaying the aggregation process, but was not capable of impeding the formation of amyloid-like fibrils. At a molar ratio of 1:10 no major difference from the fluorescence profile with the molar ratio of 1:5 was observed, but one could argue that there is a small difference verified for NB16. At a molar ratio of 1:2 the maximum ThioT fluorescence is increased for NB11 and NB16. Maybe the Nbs contribute to the formation of other structures that also allow ThioT binding, enhancing its fluorescence above the maximum verified for 77Q alone. The Nb controls presented in grey, show that nanobodies alone do not adopt any structure that allows binding of ThioT and enhancement of fluorescence (Figure 35).

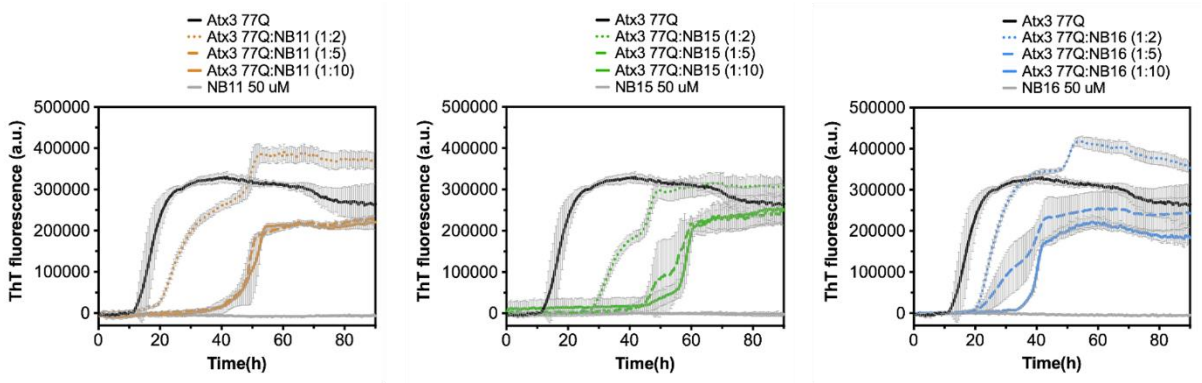

Figure 35 *- Thioflavin T aggregation assay results. Aggregation process monitored by Thioflavin T fluorescence of Atx3 17Q alone and incubated with NB11, NB15 and NB16. A molar ratio of Atx3:NB of (1:2), (1:5) and (1:10) is evaluated. Negative controls are present for the Nbs alone (grey line).*

4.5.2. Filter retardation assay

As previously shown, all the nanobodies selected impeded or delayed the formation of mature SDS-resistant fibrils over the course of circa 90 hours. No SDS-insoluble aggregates were formed in the presence of NB11, NB15 and NB16 for the time evaluated (Figure 36). Controls for NB11, NB15 and NB16 were also present to assure nanobodies do not aggregate into a structure that becomes SDS-insoluble and contribute to the signal we are reading (Figure 36).

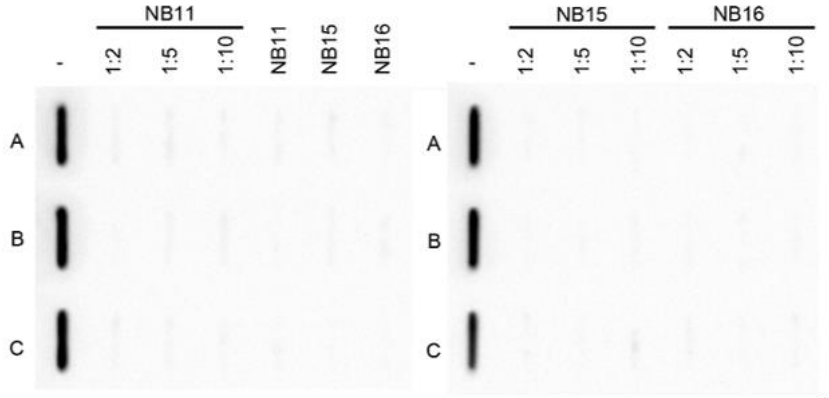

Figure 36 *- Filter retardation assay results to address the influence of different Atx3:nanobody molar ratios in the formation of SDS-resistant mature amyloid-fibrils of Atx3 77Q. Nbs analysed are NB11, NB15 and NB16. Control for Atx3 77Q alone is labelled as (-). The signal is obtained by recognition of total protein in the membrane by antibody 1H9. Negative controls are present for NB11, NB15 and NB16.*

4.5.3. Dot-Blot Assay

The different molar ratios between Atx3 and Nb were investigated through a dot-blot assay as well. Once again, the problems explained above may be present in these assays.

It appears that NB11 was the only one that did not clearly reduce the formation of OC-positive species although a clear decrease could be observed for higher NB11 concentrations (Figure 37). NB16 is the only nanobody in which a gradually higher molar ratio seems to work unlike the others, having the molar ratio of 1:2 less A11 and

OC positive species. However, one can see from the control that NB16 binds non-specifically to A11 and OC, suggesting that its effect on the development of Atx3 A11 and OC positive species might not be relevant. Curiously, as previously seen, the anti-Atx3 1H9 antibody does not recognize most of the spots containing Atx3 in complex with different Nbs. (Figure 37). This suggests that either the Atx3-bound nanobody may prevent 1H9 binding, or membrane stripping might have been too harsh and removed part of the blotted protein.

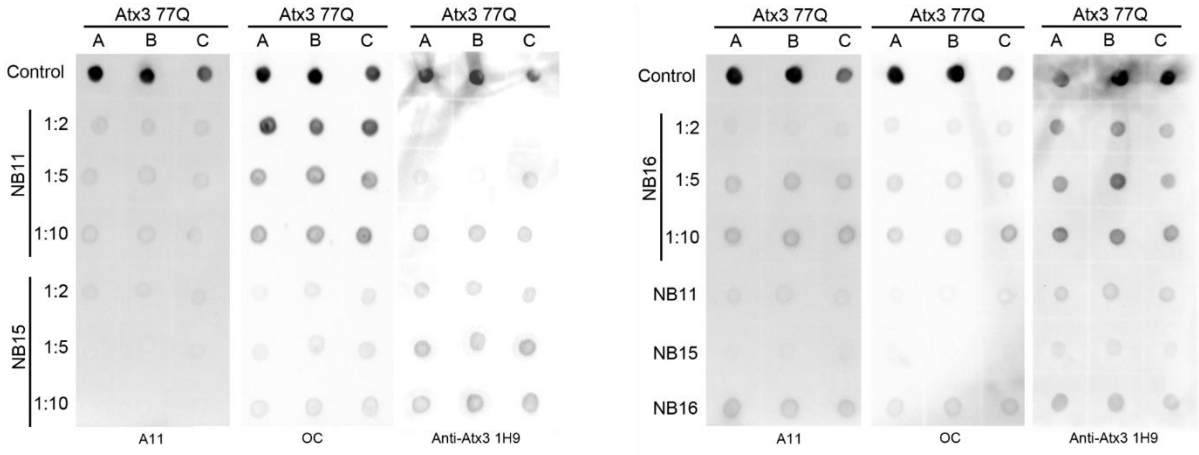

Figure 37 *- Dot Blot assay results for the study of the effect of different Atx3:Nb molar ratios (1:2), (1:5) and (1:10) on the aggregation of Atx3 77Q. The endpoint samples of the corresponding ThioT assay were used. Probing was done successively with Anti-Amyloid Oligomer A11 Antibody (that recognizes oligomeric species) followed by Anti-Amyloid Fibrils OC Antibody (that recognizes amyloid fibrils/protofibrils) and finally Anti-Atx3 1H9 Antibody (that recognizes the total Atx3 protein loaded). A, B and C are the three replicates of each condition as in the ThioT assay.*

4.5.4. Transmission Electron Microscopy

Problems with the grids' preparation occurred and no quality images were obtained. This experiment needs to be repeated.

4.6. Crystallization may be aided by nanobodies

In the limited time of this research project, it was possible to optimize conditions for the crystallization of Atx3:Nb complexes that had already been identified by the host lab and showed promising micro-crystals or larger crystals, as seen in the case of Atx3 13Q:NB19 complex. Additionally, new crystallization plates were produced using two new Nbs as chaperones: NB02 and NB20. From these plates, an optimization of some wells with microcrystals was also performed.

Atx3 13Q:NB19

As explained, the host lab had prepared multiple crystallization plates, using commercial crystallization kits to obtain crystals from the complex of Atx3 13Q with NB19. Plates were numbered in order, the first created by the host lab being #1. Plates were observed (#83, #84, #85, #86, #87 and #88) under a microscope and photographs were taken to follow crystal growth. Crystals' optimization was done for

plate #83 and #84 using the MORPHEUS (Molecular Dimensions) and Crystal Screen Cryo (Hampton Research) crystallization kits, respectively. In the table below (Table 13) the layout of the conditions where microcrystals or crystals were found is presented (See Appendix I.).

***Table 13** - Crystallization conditions of plates #83 and #84 from MORPHEUS and Crystal Screen Cryo commercial crystallization kits, respectively, for Atx3 13Q:NB19.*

Crystal Screen Cryo			
	Salt or Ligands	Buffer	Precipitant
#84 C10	None	0.07M Sodium acetate trihydrate pH 4.6	1.4M Sodium formate

MORPHEUS			
	Salt or Ligands	Buffer	Precipitant
#83 E3	0.12M Ethylene glycols	0.1M Buffer System 1 pH 6.5	50% v/v Precipitant Mix 3
#83 C10	0.09M NPS	0.1M Buffer System 3 pH 8.5	50% v/v Precipitant Mix 2
#83 B11	0.09M Halogens	0.1M Buffer System 3 pH 8.5	50% v/v Precipitant Mix 3

An example of the optimization done for all the chosen conditions is shown in Table 14 specifically for the #83 C10 conditions. A pH range of the buffer and a percentage range of precipitant was done (for Buffer System 1 the pH range was 6.0, 6.2, 6.5, 6.5, 6.7, 7.0). Plates were numbered, #101, #102, #103 and #104 following the order presented in Table 13.

***Table 14** – Schematics of the optimization of MORPHEUS condition #83 C10 - 0.09M NPS, 0.1M Buffer System 3 pH 8.5, 50% v/v Precipitant Mix 2. A variation in the buffer's pH and in precipitant's percentage is explored.*

			Buffer pH					
			1	2	3	4	5	6
			8	8.2	8.5	8.5	8.7	9
Precipitant %	A	47%						
	B	50%						
	C	50%						
	D	53%						

The Atx3 13Q:NB19 complex was prepared by the above explained purification method (see Methods) where Atx3 is firstly repurified. The final concentration of the complex used in crystallization was 19.5 mg/mL. SEC profile of Atx3 13Q:NB19 complex purification is shown below.

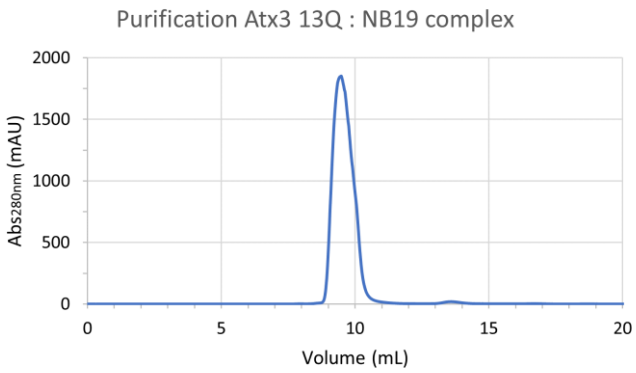

Figure 38 *– SEC profile of the purification of the Atx3 13Q:NB19 complex in complex repurification buffer (See in reagents).*

Atx3 13Q:NB02 and Atx3 13Q:NB20

Crystallization plates were prepared with Oryx 4 Robot for Atx3 13Q:NB02 and Atx3 13Q:NB20 on a molar ratio of 1:2, using the commercial screens Morpheus, SG1, Crystal Screen Cryo and INDEX. Sitting drops were composed of 0.15 µL of complex and 0.15 µL of reservoir crystallization solution (ratio of 1:1) with 50 µL reservoir volume. To correctly create the Atx3:Nb (1:2) ratio, the mass concentration is converted to the molar concentration (molarity) (Figure 39).

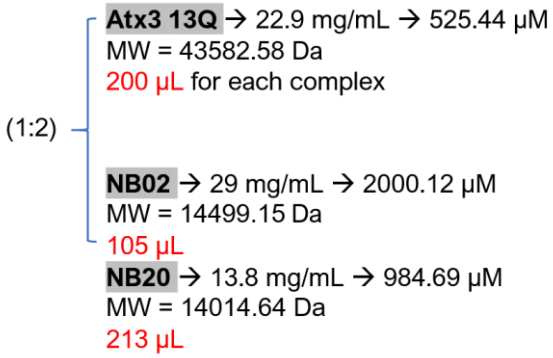

Figure 39 *- Mass concentration conversion to molarity to correctly prepare 1:2 ratios of Atx3:Nb.*

The complexes were purified and the SEC profiles are shown below (Figure 40). Protein concentration of the pooled and concentrated samples was measured at the Nanodrop at 260 nm. Final concentrations were 18.7 mg/mL for Atx3 13Q:NB02 and 18.1 mg/mL for Atx3 13Q:NB20, and both complexes were diluted to 17 mg/mL prior to crystallization assays. The remaining complex solution was frozen at -80°C.

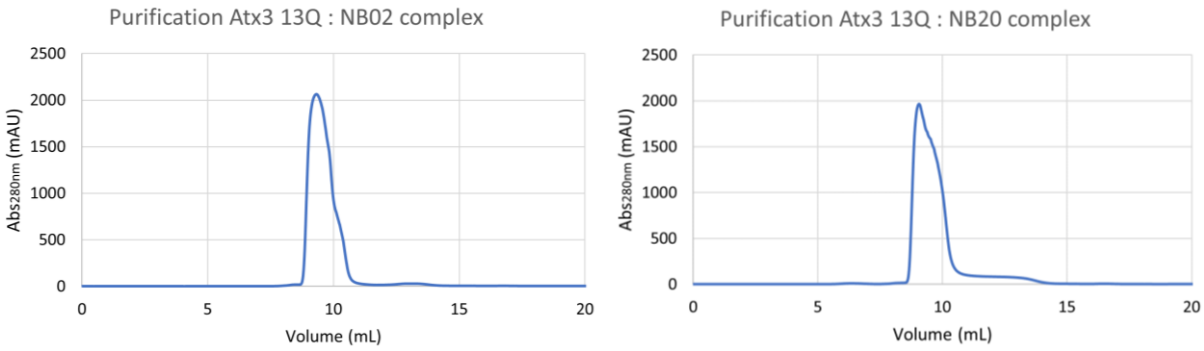

Figure 40 *- SEC profiles of the purification of Atx3 13Q in complex with NB02 and NB20.*

Plates were numbered and prepared with corresponding kits as shown in Table 15 by the robot.

#105	Up Atx3 13Q : NB02 (1:2)	MORPHEUS
	Down Atx3 13Q : NB20 (1:2)	
#106	Up Atx3 13Q : NB02 (1:2)	CRYO
	Down Atx3 13Q : NB20 (1:2)	
#107	Up Atx3 13Q : NB02 (1:2)	INDEX
	Down Atx3 13Q : NB20 (1:2)	
#108	Up Atx3 13Q : NB02 (1:2)	SG1
	Down Atx3 13Q : NB20 (1:2)	

Plates were routinely monitored searching for crystals and reporting the progression of what was seen under the microscope. From plates #105, #106 and #108, some conditions were optimized since microcrystals were observed, as illustrated in Figure 41.

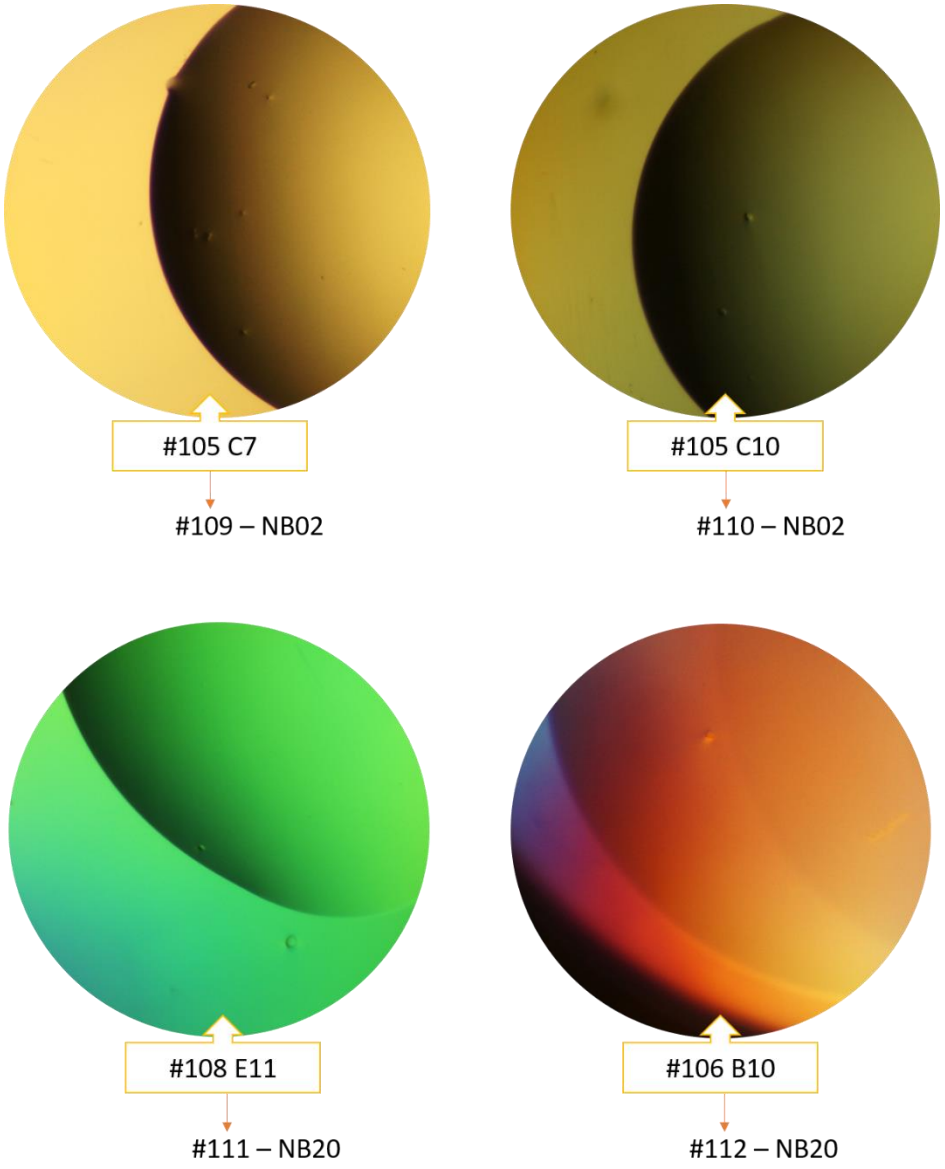

Figure 41 *- Microscopic images of crystallization drops corresponding to the conditions optimized. Specifically MORPHEUS C7 and C10 upper wells and Crystal Screen Cryo and SG1 B10 and E11 lower wells, respectively. 100X magnification.*

***Table 15** - Optimized #109, #110, #111 and #112 plates mean salt or ligand, buffer and precipitant conditions from which a variation is done.*

MORPHEUS				
	Salt or Ligands	Buffer	Precipitant	
#109	0.9M NPS	Buffer 2 pH 7.5	50% v/v Precipitant Mix 3	
#110	0.9M NPS	Buffer 3 pH 8.5	50% v/v Precipitant Mix 2	

SG1				
#111	2M sodium formate	0.1M sodium acetate pH 4.5		

Crystal Screen Cryo				
#112	0.17M sodium acetate	0.085M Tris HCl pH 8.5	25.5% PEG 4K	15% v/v Glycerol

Optimizations of these preliminary crystallization conditions were done thawing the previously prepared Atx3 13Q:NB02 and Atx3 13Q:NB20 complexes, exploring variations in pH and different concentrations of precipitant, as illustrated in Figure 42.

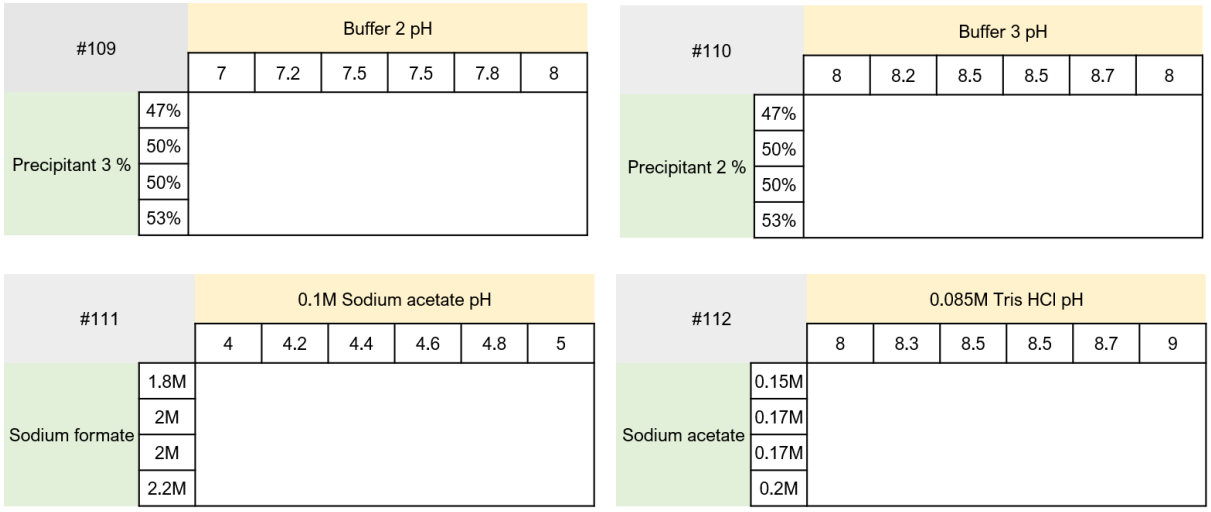

***Figure 42** – Schematics of the optimization of MORPHEUS condition C7 and C10 (#109 and #110, respectively), SG1 condition E11 (#111) and Cryo Screen Cryo condition B10 (#112). A range of pH of the buffer, different precipitant percentage and salt molar concentration is explored.*

So far, no crystals have been observed in any of the plates prepared at the time of study, but continuous monitoring will be carried out.

4.7. A MJD Drosophila m. model was successfully reproduced

Drosophila m. genetically transformed to establish a MJD fly model were kindly provided by our external collaborator, Prof. Sokol V. Todi ([200]–[203]). Several other studies have been published where this model had a clear degenerative phenotype, constituting a good MJD model [183], [184]. All Atx3 variants are human and contain three UIMs. A list of the transgenic lines produced is shown in Table 16.

Table 16 *- Genotype of all the flies prepared by Sokol Todi's team. These flies do not express any protein but carry the necessary information for further crossing. Atx3 80Q is composed of glutamines coded by different codons (CAG and CAA), sequentially.*

w-	sqh-Gal4	+
w-	+	attp2 landing site
w-	Sp/Cyo	Sb/Tm3(Ser)
w-	UAS-Atx3Q22-His6	+
yw	Sp/Cyo	UAS-Atx3Q77-(CAG)-No Tag
w-	+	UAS-Atx3Q80(CAGCAA)-HA

GMR-Gal4 and ELAV-Gal4 female flies were crossed with each of the other male lines to produce a wild-type line, a landing-site control line, a normal Atx3 expressing line (22Q) and two pathological lines expressing Atx3 with 77 or 80 glutamine repeats. For the rest of the document these lines will be addressed to as GMR or ELAV: Gal4-OR-R, Gal4-attp2, Gal4-22Q, Gal4-77Q and Gal4-80Q, respectively.

Offspring flies were maintained for 23 days at 25°C and 29°C, in which evolutions and differences in phenotype and lifespan were registered and images of the adult retina at intermediate time-points were taken (Figure 43, Figure 44 and Figure 45).

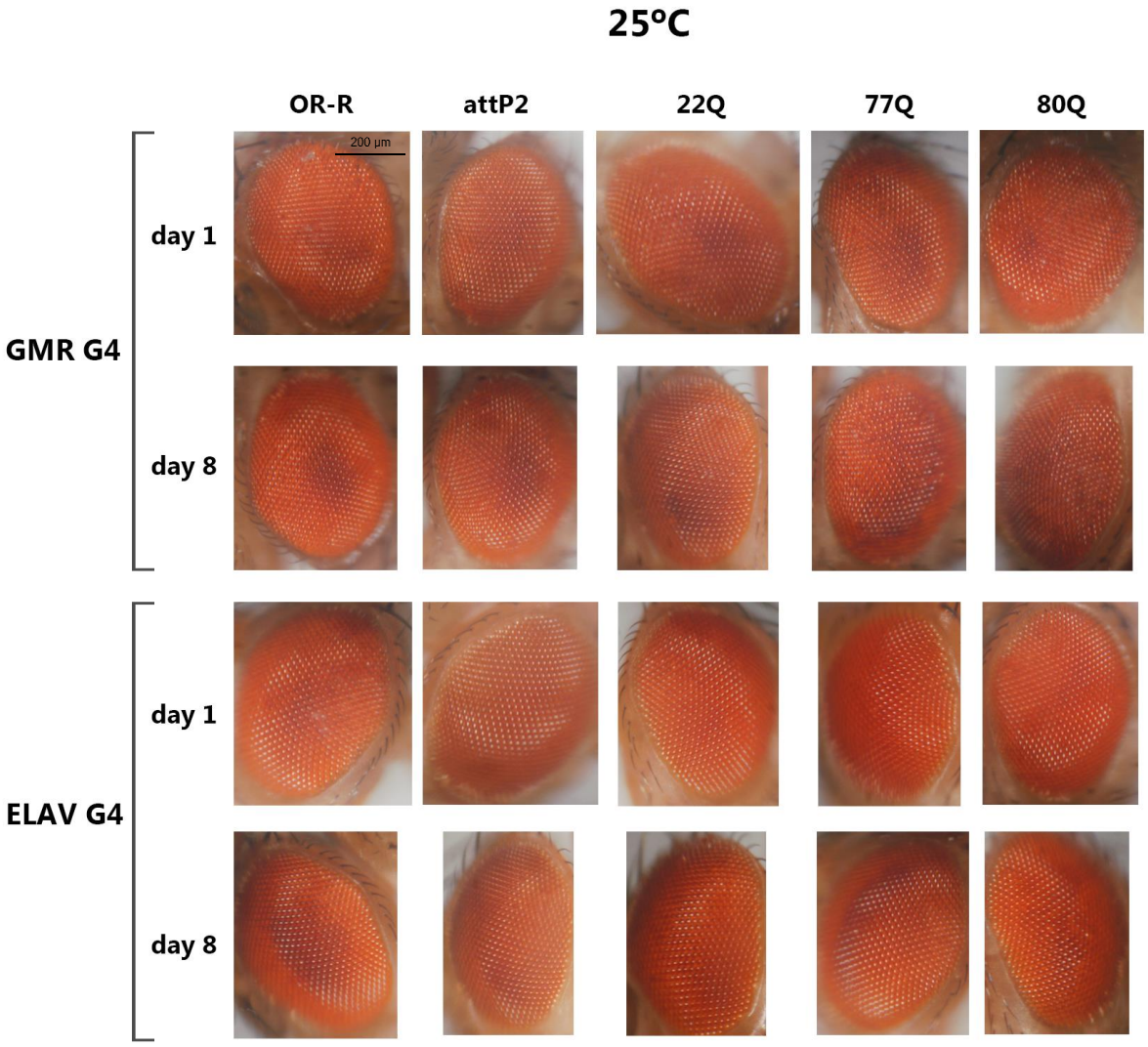

Figure 43 *- Drosophila m. panel with representative images of the adult retina of the different GMR and ELAV lines (OR-R, attP2, 22Q, 77Q and 80Q) under study, growing at 25ºC.*

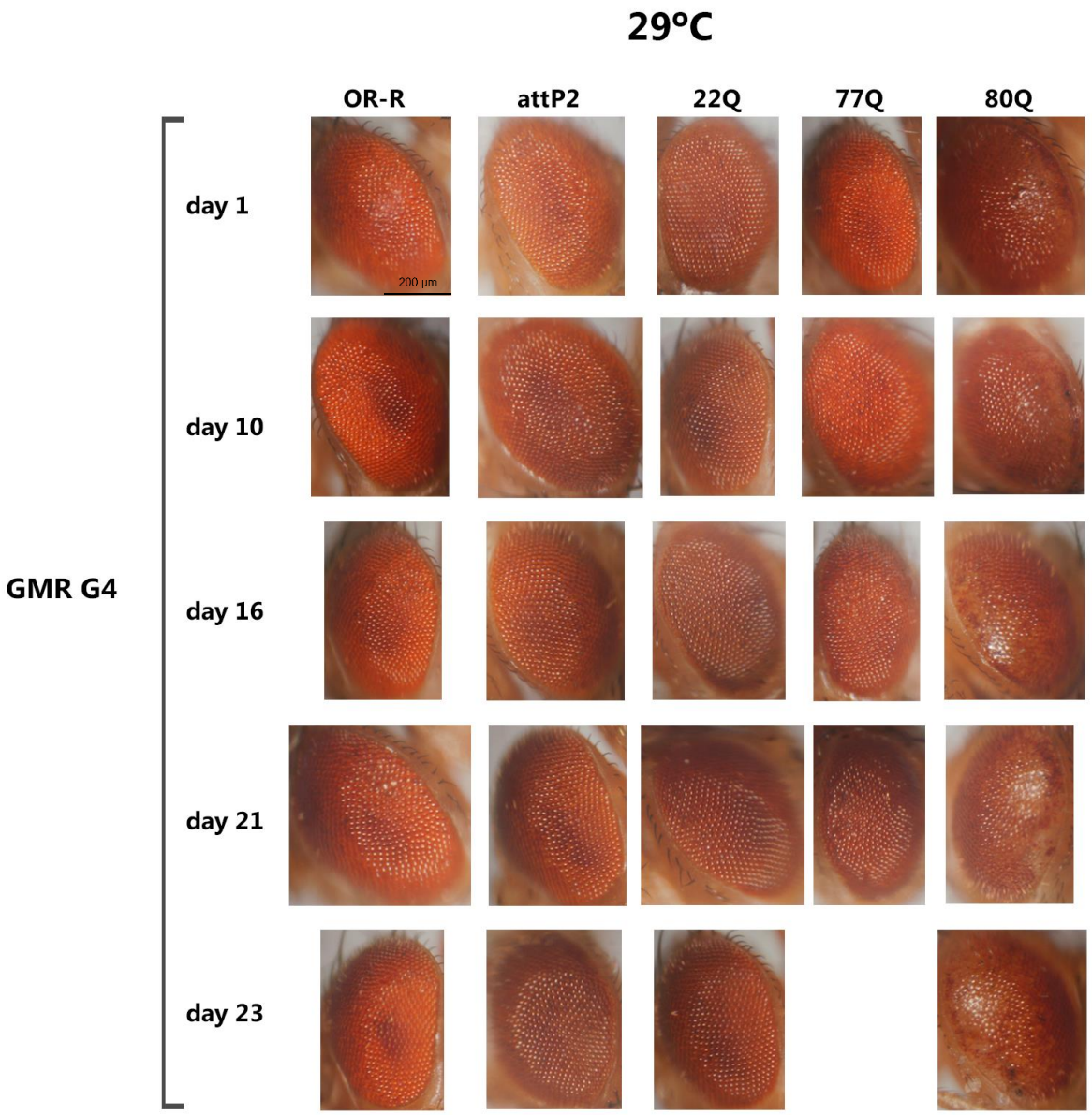

Figure 44 *- Drosophila m. panel with representative images of the adult retina of the different GMR lines (OR-R, attP2, 22Q, 77Q and 80Q) under study, growing at 29°C.*

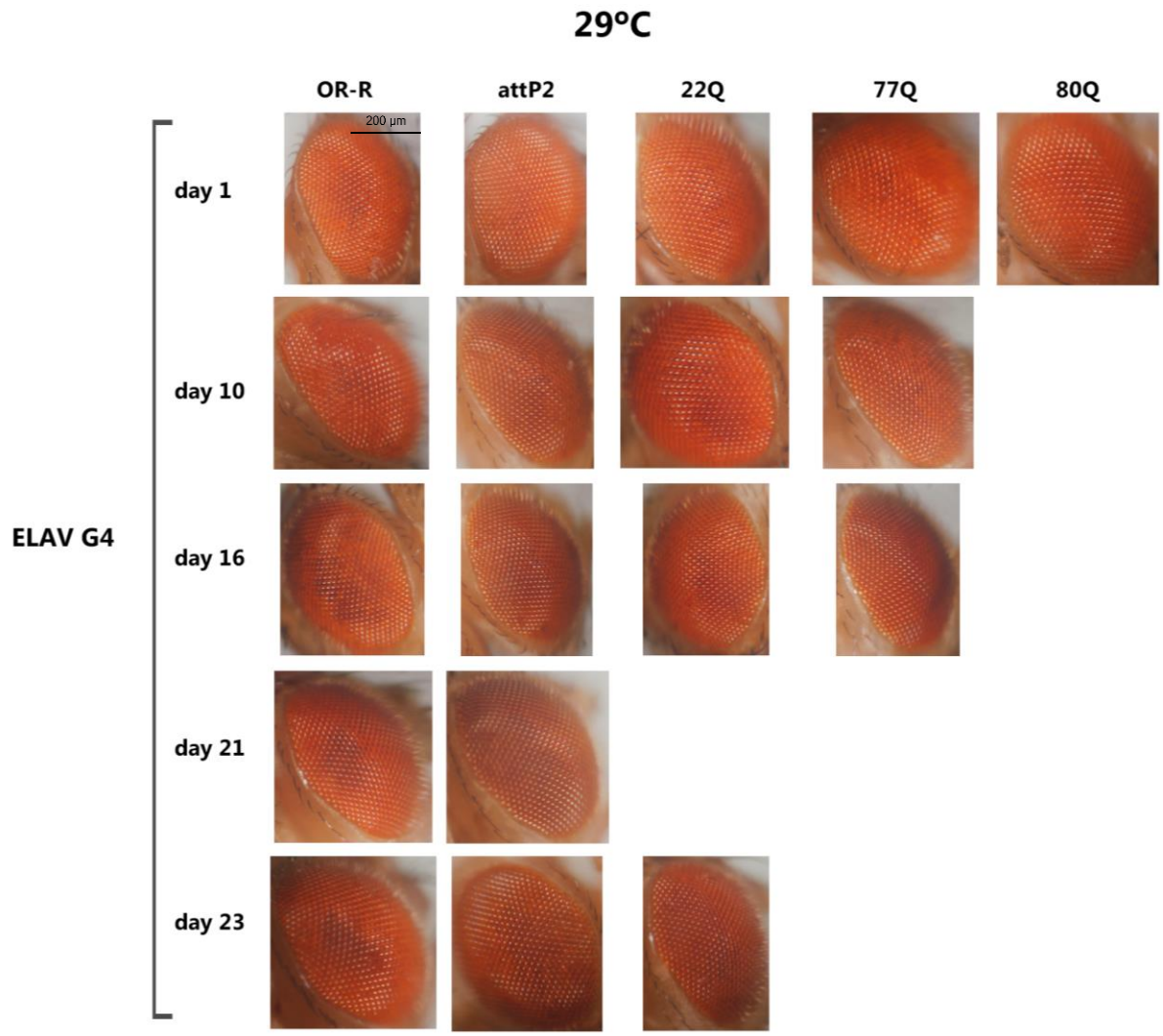

Figure 45 *- Drosophila m. panel with representative images of the adult retina of the different ELAV lines (OR-R, attP2, 22Q, 77Q and 80Q) under study, growing at 29°C.*

It was evident that flies did not develop a clear distinctive phenotype growing at 25°C and for that reason, no follow-up photographs were taken after day 8. In fact, loss of the pseudo pupil was observed for GMR-Gal4-77Q and GMR-Gal4-80Q lines, but it was not enough to reproduce a MJD fly model that showed a strong distinctive phenotype from the wildtype. However, for flies growing at 29°C a clear degenerative phenotype with loss of pigment was observed for GMR-Gal4-80Q flies (Figure 44). GMR-Gal4-77Q flies also showed loss of the pseudo pupil and visible degeneration in some cases (Figure 44). For the ELAV-Gal4 lines growing at 29°C, no degenerative phenotype was observed in the external retina, however, the lifespan of ELAV-Gal4-77Q and ELAV-Gal4-80Q lines was around 10 days, suggesting that the pan-neural expression of expanded Atx3, including in motor neurons is probably the cause of this lifespan reduction. In upcoming experiments, where these lines are again produced (It is not possible to maintain fly stocks with these genotypes) a climbing assay would help assess motor dysfunction and a count of flies for each condition should be made to quantitively appraise lifespan.

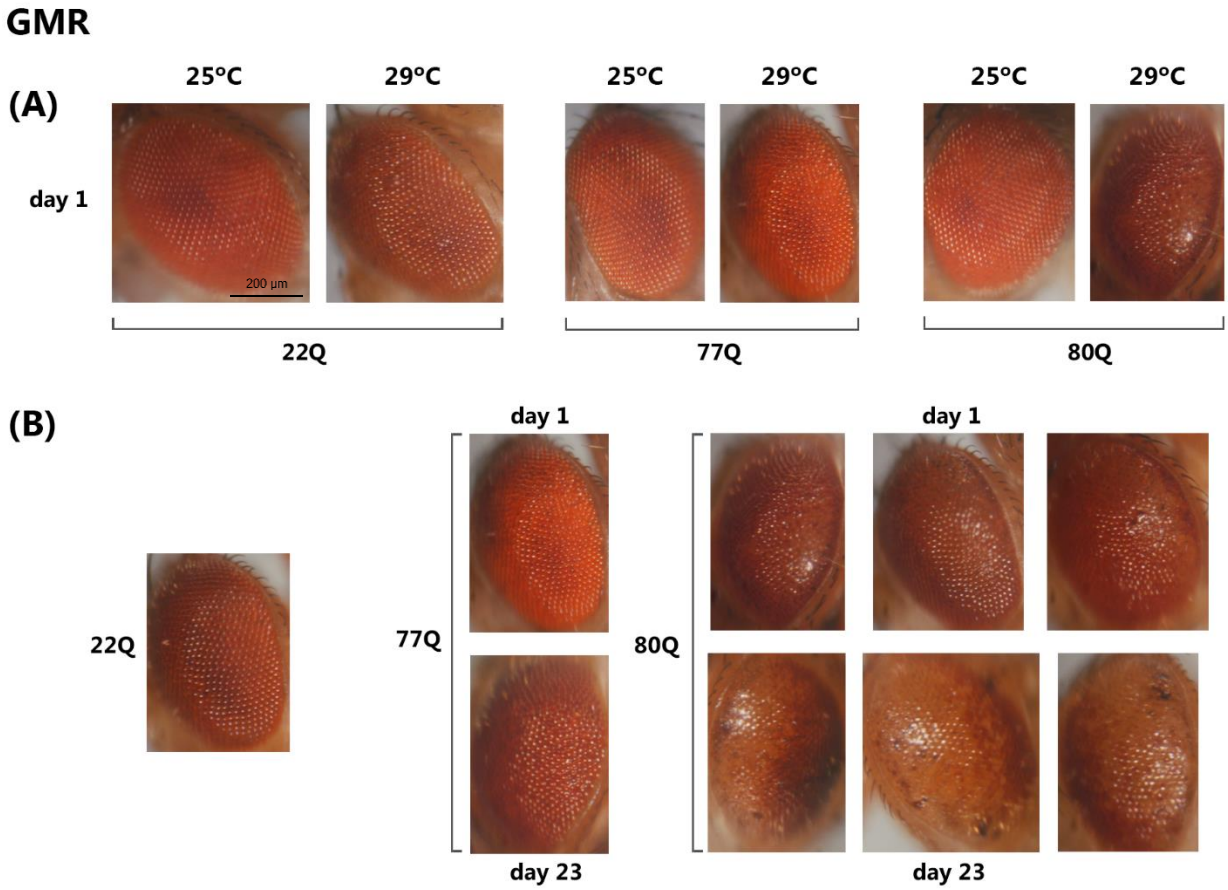

Figure 46 – (A) *Comparison between GMR 22Q, 77Q and 80Q phenotypes of flies growing at 25°C and 29°C (day 1)* ***(B)*** *Evolution and comparison of phenotype between GMR 22Q, 77Q and 80Q lines (day 1 and day 23 for the last two lines).*

A strong MJD fly model, with distinctive and rapidly identifiable characteristics was reproduced, establishing a platform for the study of the ability of Nbs to protect against degeneration and act as neuroprotective agents.

Although it was not possible to proceed with the experimental plan in the time defined for the project, the pUASTattB-Nb vectors necessary to genetically modify *Drosophila m.* embryos, carrying the coding sequence for the Nbs, were prepared as described in the following sections.

4.8. pUASTattB-Nbs plasmids construction

PCR based cloning was the technique used to place the DNA Nb coding sequence into the relevant pUASTattb vector backbone. The schematic of the process is illustrated in Figure 47.

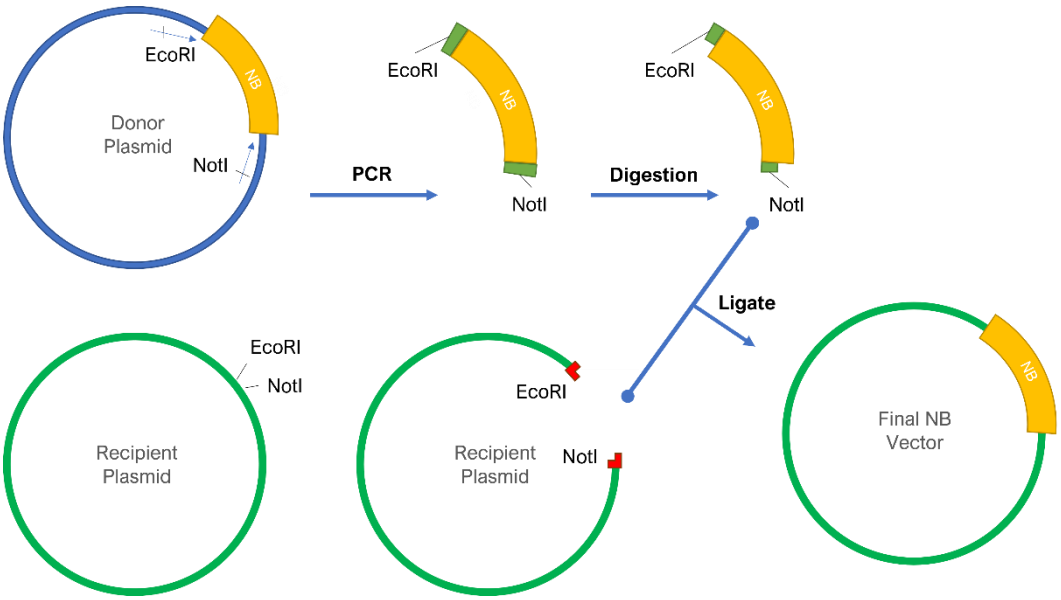

Figure 47 *– Schematics of PCR cloning steps. Insertion of the Nb construct in the pUASTattB vector.*

4.8.1. Amplification of Nb constructs

Amplification through Polymerase Chain Reaction (PCR) was done with Phusion enzyme with optimized conditions following (see Methods). PCR products were cleaned, quantified in the NanoDrop 100 by measuring Abs at 260nm (Figure 48A) and analysed by agarose gel electrophoresis to confirm the fragment size (Figure 48B). NB01, NB02, NB05, NB19 and NB20 have 396, 411, 396, 390, 402 base pairs, respectively.

A

PCR clean NB plasmids	
Concentration	ng/µL
NB01	253.8
NB02	237.2
NB05	242.8
B19	251
NB20	228.5

B

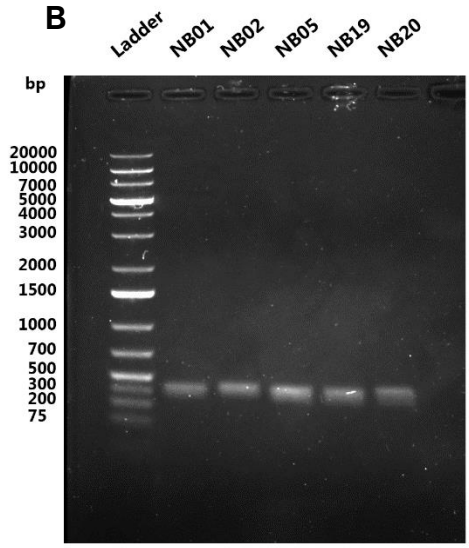

Figure 48 *– **(A)** Nb constructs concentration after cleaning the PCR products **(B)** Agarose gel analysis of the Nb constructs.*

4.8.2. Replication of pUASTattB

Replication of the vector pUASTattB was done to assure there was enough plasmid to work with as detailed above (see Methods). The final concentration yielded was 49.2 ng/µL for the Miniprep and 366.9 ng/µL for the Midiprep.

4.8.3. Digestion of Nbs and pUASTattB

Both the Nb constructs and the pUASTattB were digested with EcoRI and NotI following the explained protocol and the rational previously presented (see Methods). Products of the enzymatic digestion were analysed by agarose gel electrophoresis to confirm the presence and size of the Nb fragments and of the vector pUASTattB (Figure 49A). DNA purification of the Nb fragments and of the double digested vector pUASTattB (band excised from the agarose gel (240 mg)) was performed. The final concentration was measured and yielded the values reported in Figure 49B.

A

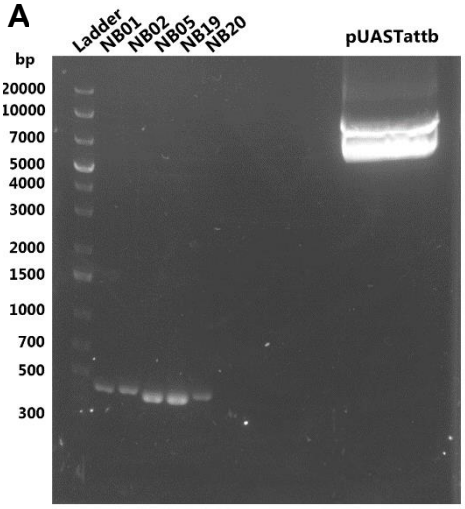

B

Concentration	ng/µL
enzymatic digestion NBs	
NB01	99.1
NB02	86.2
NB05	98.7
NB19	112.5
NB20	104.6
excised agarose band	
Vector	26.3
Vector (eluted again)	22

Figure 49 *– **(A)** Agarose gel analysis of the products of Nb construct and pUASTattB vector digestion with EcoRI and NotI **(B)** Concentration of cleaned digested NB constructs and cleaned vector from excised agarose band.*

The two bands that appear in the agarose gel for the pUASTattB vector may be a result of the presence of digested vector and non-digested vector or only one of the enzymes having cut the vector. DNA precipitation in ethanol of the vector pUASTattB was done aiming to increase the concentration but resulted in a final concentration of 22 ng/µL.

4.8.4. DNA Ligation and cell transformation

DNA ligation was tested both for 2 hours at 22°C and overnight at 16°C, following the protocol explained above (see Methods).

DH5α competent cells were transformed with the resulting plasmids from ligation (pUAST-attB-NB). The negative control for these procedures is the cell transformation with the pUAST-attB vector alone, which remains linear upon digestion and ligation, not yielding any colonies. By transforming cells with the plasmids from the first tested ligation option, 2 hours at 22ºC, colonies grew in the control. This suggests the vector was either not well cut by the restriction enzymes or some remained circular.

Digestion of the vector alone was performed to understand if both enzymes were cutting the vector. The digested plasmid contains 8470 bp. Even though the bands do not seem to correspond to the correct and expected size of the vector (8470 bp), both enzymes are cutting since the bands are all at the same level (Figure 50).

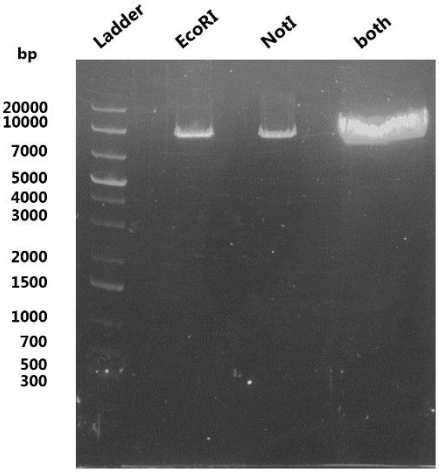

Figure 50 *– Agarose gel analysis of pUASTattB vector digestion with EcoRI and NotI together and separately.*

The band on the right was excised (400mg) and DNA purification of the vector was carried out yielding a final concentration of 37.1 ng/µL. DNA precipitation in ethanol was done to try to rise the concentration of the sample and improve the absorbance readout parameters, finishing with 41 ng/µL but improving the 260/280 and 260/230 absorbance parameters. This vector was used to perform ligation ON at 16ºC.

DH5α competent cells were then transformed with all the plasmids from ligation conducted ON at 16ºC. In this case, no colonies grew in the negative control. A midiprep protocol was conducted using positive clones of each transformation which yielded pUASTattB-NB plasmids with the concentrations presented in Table 17.

Table 17 - Final plasmid pUAST-attB-NB concentrations.

	ng/µL
pUAST-attB-NB01	584
pUAST-attB-NB02	685
pUAST-attB-NB05	712
pUAST-attB-NB19	496
pUAST-attB-NB20	503.8

The DNA ligation was confirmed by digesting the plasmid with EcoRI and NotI and analysing it in agarose gel and the DNA sequence was confirmed by nucleotide sequencing. From the agarose gel it was clear that Nbs inserts were present, but the bands did not correspond to the correct Nb fragment size (Figure 51). Some technical problem with the preparation of the agarose gel or with the DNA electrophoresis may have happened, given that sequencing the plasmids showed an optimal score of comparison between the theoretical sequences and the prepared plasmids (a nucleotide BLAST was conducted online with the results sent from the company who does the sequencing).

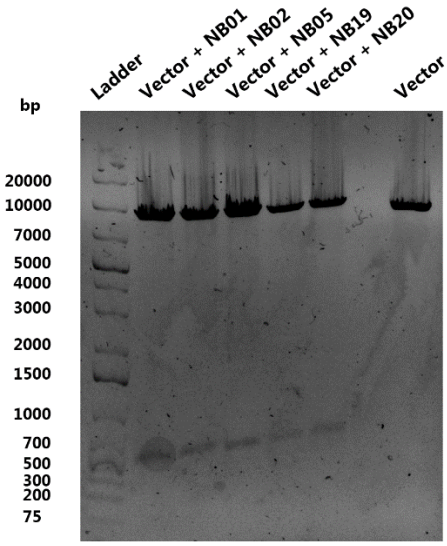

Figure 51 *- Agarose gel analysis confirming the DNA ligation of the vector and the Nb inserts.*

The pUAST-attB-NB plasmids were sent to CONGENTO (PT, https://congento.org/) and fly lines were generated using the site-specific pHiC31 integration system. The use of the PhiC31 system guarantees equivalent expression levels for all UAS-Nbs transgenes, enabling phenotype comparison among selected Nbs.

Once receiving the UAS-Nb fly lines, the following procedures would have been carried out:

- The GMR-Gal4 driver is used to co-express Atx3(77Q and 80Q) and the selected Nbs in the fly retina (genotype: GMR-Gal4; UAS-Atx3(80Q); UAS-NB). The impact in the morphology of the retina in 1-day old adult flies is evaluated.
- Nanobodies are scored as strong, mild or no suppressors of Atx3(80Q) phenotype, according to their ability to restore retina morphology on Atx3(80Q)-expressing flies.
- The ELAV-Gal4 driver is also used to co-express Atx3 and the selected Nbs. The impact of Nbs in lifespan and climbing assay performance of adult-flies (done with flies of different ages) is evaluated.
- Nanobodies are scored in the same way, according to their ability to improve lifetime and motor capabilities.

Chapter 5

Conclusions and future perspectives

The global analysis of the results of the multiple lab experiments performed in the scope of this work, allows to draw some conclusions and to propose future lines of work.

The experiments do not allow to qualitatively conclude whether there is a reduction in the number of fibrils. For Atx3 77Q it can be stated there is an alteration in the process of fibril maturation where NB06, NB08, NB11, NB12, NB14, NB15, NB16 and NB17 delay or prevent the formation of amyloid-like fibrils. In the case of Atx3 13Q there is an apparent reduction in the number of fibrils and fibril size (evaluated by TEM) when incubated with NB06, NB07, NB13 and NB15.

It is not understanded yet if preventing the maturation of fibrils into amyloid-like fibrils will be beneficial or harmful in the scenario of the disease. Intermediate fibrillar species and oligomeric species may end up being more toxic than mature fibrils. The protein is known to have several functions in the cell. In knock-out models, organisms survive, but when Atx3 expression is reduced, cells become more susceptible to stress. The consequences of removing or blocking the protein are not yet known. Nanobodies may have a serious negative effect. It remains to be decided if anything can be concluded or stated regarding the potential of Nbs as therapeutic agents without knowing the pathogenesis mechanisms and toxic species. Studies *in vivo*, in *Drosophila m.* using Nbs will be important to conduct as they will give us phenotypic results.

Further questions should be addressed: when is the right time to administer the Nbs? Does it make more sense to design Nbs to delay the onset of disease or to delay disease progression in patients already with symptoms? It may be too late to administer the Nbs when the disease has already manifested and produce a significant effect. Would it even be possible to achieve an improvement of symptoms on patients with advanced MJD? Overall, the therapeutic Nb agent should be as innocuous as possible, not affecting the function of the native protein.

Even though we chose NB11, NB15 and NB16 to evaluate the impact of Atx3:Nb molar ratio on Atx3 aggregation dynamics, other Nbs may also be an option to study. The chosen Nbs were the ones that most significantly delayed the aggregation and prevented the appearance of A11-positive species, which are correlated with toxicity, according to literature. Examples of other options are NB13 and NB14, that presented some interesting features. Both NB13 and NB14 delayed aggregation. Additionally, NB13 prevented the formation of A11-positive species and reduced the apparent amount of fibrils and oligomeric species, only for Atx3 13Q. Mature fibrils were

observed in TEM images of Atx3 77Q with NB13. NB14 was the other way around, it prevented the formation of A11-positive species and reduced the apparent amount of fibrils and oligomeric species, only for Atx3 77Q. No mature fibrils were observed at the endpoint of aggregation. NB06, NB12 and NB17 showed similar results as the chosen Nbs but were not included due to time restrictions.

From the Nbs characterized *de novo* (NB11, NB15 and NB16), at least two should be characterized with more detail (with Dynamic Light Scattering, Isothermal Titration Calorimetry and SEC assays, for example) to confirm they are good candidates for the *Drosophila m*. studies proposed.

Studies in a MJD model of primary cortical neuronal cells may also be conducted to obtain higher level information about the Nbs potential as therapeutical agents.

In vitro cellular studies that state A11-positive species are more toxic are studies where initially probed species marked as A-11 positive are incubated with cells. It is not known how these species change once they are incubated with the cells. The only thing we can say is that protein species marked at time 0h as positive for A11 have a toxic effect, more toxic than when incubating the cells with mature fibrils. These experiments were not yet done for Atx3.

Nanobody engineering approaches will serve to improve circulation time and to introduce the ability of Nbs to bind specific receptors. To facilitate blood brain barrier penetrance and to lead Nbs to their targeted sites in the brain more easily and allow interaction of specific cellular populations.

Appendix

I.

Table 18 *- Mixes of additives used in Morpheus.*

Mix name	Composition	Catalogue Number (100 & 250mL)
Halogens	0.3M Sodium fluoride; 0.3M Sodium bromide; 0.3M Sodium iodide	MD2-100(250)-71
NPS†	0.3M Sodium nitrate, 0.3 Sodium phosphate dibasic, 0.3M Ammonium sulfate	MD2-100(250)-72
Ethylene glycols	0.3M Diethylene glycol; 0.3M Triethylene glycol; 0.3M Tetraethylene glycol; 0.3M Pentaethylene glycol	MD2-100(250)-74

Table 19 *- Buffer systems used in Morpheus.*

Mix name	Conc.	pH @ 20°C	Composition	Catalogue Number (100 & 250mL)
Buffer System 1	1.0M	6.5	Imidazole; MES monohydrate (acid)	MD2-100(250)-100
Buffer System 2	1.0M	7.5	Sodium HEPES; MOPS (acid)	MD2-100(250)-101
Buffer System 3	1.0M	8.5	Tris (base); BICINE	MD2-100(250)-102

Table 20 *- Mixes of Precipitants used in Morpheus.*

Mix name	Old Mix Name	Composition	Catalogue Number (100 & 250mL)
Precipitant Mix 1	P500MME_P20K	40% v/v PEG 500* MME; 20 % w/v PEG 20000	MD2-100(250)-81
Precipitant Mix 2	EDO_P8K	40% v/v Ethylene glycol; 20 % w/v PEG 8000	MD2-100(250)-82
Precipitant Mix 3	GOL_P4K	40% v/v Glycerol; 20% w/v PEG 4000	MD2-100(250)-83
Precipitant Mix 4	MPD_P1K_P3350	25% v/v MPD; 25% PEG 1000; 25% w/v PEG 3350	MD2-100(250)-84

II.

Table 21 *- Nanobody and Atx3 variants details – theoretical isoelectric point, molecular weight, extinction coefficient and Abs 0.1% (=1g/L) correction value.*

NB	Code	Theoretical pI	MW (Da)	Ext. coefficient	Abs 0.1% (=1g/L)
NB01	CA11570	8.63	14155.7	21555	1.523
NB02	CA11599	8.66	14499.15	18575	1.281
NB03	CA11609	6.3	15091.62	32555	2.157
NB05	*CA11574*	7.18	14080.63	20065	1.425
NB06	*CA11578*	7.82	14919.55	33015	2.213
NB07	CA11573	6.57	13922.57	24075	1.729
NB08	CA11572	6.57	13881.51	24075	1.734
NB11	*CA11575*	8.98	14944.62	28545	1.910
NB12	*CA11577*	7.0	14977.58	33015	2.204
NB13	CA11543	6.64	14036.59	20065	1.429
NB14	CA11576	8.59	15144.79	30035	1.983
NB15	CA11564	9.03	14072.7	20065	1.426
NB16	CA11565	9.03	13950.66	18575	1.331
NB17	CA11568	8.64	14019.55	25565	1.824
NB19	CA111593	8.63	13968.57	21555	1.534
NB20	CA111594	8.02	14014.64	18575	1.325

Atx3 variants	ID code	Theoretical pI	MW (Da)	Ext. coefficient	Abs 0.1% (=1g/L)
13Q		4.86	43582.5	31650	0.726
77Q		4.9	51882	31650	0.61

References

[1] W. J. Woods, S. D. Klingemann, and J. R. Guydish, “Nigro-spino-dentatal Degeneration with Nuclear Ophthalmoplegia A Unique and Partially Treatable Clinico-pathological Entity,” *J. Psychoactive Drugs*, vol. 34, no. 1, pp. 17–24, 2002, doi: 10.1080/02791072.2002.10399932.

[2] R. N. Rosenberg, W. L. Nyhan, C. Bay, and P. Shore, “Autosomal dominant striatonigral degeneration: A ctinical, pathologic, and biochemical study of a new genetic disorder,” *Neurology*, vol. 26, no. 8, pp. 703–714, 1976, doi: 10.1212/wnl.26.8.703.

[3] A. Romanul, “Azorean Disease of the Nervous System,” *N. Engl. J. Med.*, vol. 297, no. 13, pp. 729–730, 1977, doi: 10.1056/nejm197709292971318.

[4] L. Ruano, C. Melo, M. C. Silva, and P. Coutinho, “The global epidemiology of hereditary ataxia and spastic paraplegia: A systematic review of prevalence studies,” *Neuroepidemiology*, vol. 42, no. 3, pp. 174–183, 2014, doi: 10.1159/000358801.

[5] T. Li *et al.*, “Is the high frequency of machado-joseph disease in China due to new mutational orignis?,” *Front. Genet.*, vol. 10, no. FEB, pp. 1–8, 2019, doi: 10.3389/fgene.2018.00740.

[6] P. Maciel *et al.*, “Improvement in the molecular diagnosis of Machado-Joseph disease,” *Arch. Neurol.*, vol. 58, no. 11, pp. 1821–1827, 2001, doi: 10.1001/archneur.58.11.1821.

[7] C. Bettencourt, C. Santos, T. Kay, J. Vasconcelos, and M. Lima, “Analysis of segregation patterns in Machado-Joseph disease pedigrees,” *J. Hum. Genet.*, vol. 53, no. 10, pp. 920–923, 2008, doi: 10.1007/s10038-008-0330-y.

[8] Y. Kawaguchi *et al.*, “CAG expansions in a novel gene for Machado-Joseph disease at chromosome 14q32.1,” *Nat. Genet.*, vol. 8, no. 3, pp. 221–228, 1994, doi: 10.1038/ng1194-221.

[9] R. M. De Castilhos *et al.*, “Spinocerebellar ataxias in Brazil - Frequencies and modulating effects of related genes,” *Cerebellum*, vol. 13, no. 1, pp. 17–28, 2014, doi: 10.1007/s12311-013-0510-y.

[10] M. Lima *et al.*, “Population genetics of wild-type CAG repeats in the Machado-Joseph Disease gene in Portugal,” *Hum. Hered.*, vol. 60, no. 3, pp. 156–163, 2005, doi: 10.1159/000090035.

[11] Y. Takiyama, K. Sakoe, I. Nakano, and M. Nishizawa, “Machado-Joseph disease: Cerebellar ataxia and autonomic dysfunction in a patient with the shortest known expanded allele (56 CAG repeat units) of the MJD1 gene,” *Neurology*, vol. 49, no. 2, pp. 604–606, 1997, doi: 10.1212/WNL.49.2.604.

[12] I. N. Van Schaik, G. J. Jöbsis, M. Vermeulen, H. Keizers, P. A. Bolhuis, and M. De Visser, “Machado-Joseph disease presenting as severe asymmetric proximal neuropathy,” *J. Neurol. Neurosurg. Psychiatry*, vol. 63, no. 4, pp. 534–536, 1997, doi: 10.1136/jnnp.63.4.534.

[13] A. Bitsch, T. Kuhlmann, C. Stadelmann, H. Lassmann, C. Lucchinetti, and W. Brück, “A longitudinal MRI study of histopathologically defined hypointense multiple sclerosis lesions,” *Ann. Neurol.*, vol. 49, no. 6, pp. 793–796, 2001, doi: 10.1002/ana.1053.

[14] C. A. Matos, L. P. de Almeida, and C. Nóbrega, “Machado–Joseph disease/spinocerebellar ataxia type 3: lessons from disease pathogenesis and clues into therapy,” *J. Neurochem.*, vol. 148, no. 1, pp. 8–28, 2019, doi: 10.1111/jnc.14541.

[15] J. D. Brook *et al.*, “Molecular basis of myotonic dystrophy: Expansion of a trinucleotide (CTG) repeat at the 3′ end of a transcript encoding a protein kinase family member,” *Cell*, vol. 68, no. 4, pp. 799–808, 1992, doi: 10.1016/0092-8674(92)90154-5.

[16] S. Kiesewetter *et al.*, “© 199 3 Nature Publishing Group http://www.nature.com/naturegenetics,” *Nat. Genet.*, vol. 3, pp. 73–96, 1993.

[17] M. E. MacDonald *et al.*, “A novel gene containing a trinucleotide repeat that is expanded and unstable on Huntington’s disease chromosomes,” *Cell*, vol. 72, no. 6, pp. 971–983, 1993, doi: 10.1016/0092-8674(93)90585-E.

[18] R. Koide *et al.*, “Unstable expansion of CAG repeat in hereditary dentatorubral–pallidoluysian atrophy (DRPLA),” *Nat. Genet.*, vol. 6, no. 1, pp. 9–13, 1994, doi: 10.1038/ng0194-9.

[19] S. M. Pulst *et al.*, “Moderate expansion of a normally biallelic trinucleotide repeat in spinooerebellar ataxia type,” *Nat. Genet.*, vol. 14, no. 3, pp. 269–276, 1996, doi: 10.1038/ng1196-269.

[20] M. Mendez, L. Green, J. Corvalan, X. Jia, C. Maynard-Currie, and A. Jakobovits, “© 199 7 Nature Publishing Group http://www.nature.com/naturegenetics,” *Nat. Genet.*, vol. 15, pp. 57–61, 1997.

[21] A. Silva, A. V. de Almeida, and S. Macedo-Ribeiro, “Polyglutamine expansion diseases: More than simple repeats,” *J. Struct. Biol.*, vol. 201, no. 2, pp. 139–154, 2018, doi: 10.1016/j.jsb.2017.09.006.
[22] J. R. Gatchel and H. Y. Zoghbi, “Diseases of unstable repeat expansion: mechanisms and common principles,” *Nat. Rev. Genet.*, vol. 6, no. 10, pp. 743–755, 2005, doi: 10.1038/nrg1691.
[23] H. Y. Zoghbi and H. T. Orr, “Glutamine Repeats and Neurodegeneration,” *Annu. Rev. Neurosci.*, vol. 23, pp. 217–247, 2000, [Online]. Available: http://www.ncbi.nlm.nih.gov/pubmed/10845064.
[24] M. do C. Costa and H. L. Paulson, “Toward understanding Machado-Joseph disease,” *Prog. Neurobiol.*, vol. 97, no. 2, pp. 239–257, 2012, doi: 10.1016/j.pneurobio.2011.11.006.
[25] C. A. Matos, S. de Macedo-Ribeiro, and A. L. Carvalho, “Polyglutamine diseases: The special case of ataxin-3 and Machado-Joseph disease,” *Prog. Neurobiol.*, vol. 95, no. 1, pp. 26–48, 2011, doi: 10.1016/j.pneurobio.2011.06.007.
[26] C. Bettencourt, “The APOE ε2 Allele Increases the Risk of Earlier Age at Onset in Machado-Joseph Disease,” *Arch. Neurol.*, vol. 68, no. 12, p. 1580, Dec. 2011, doi: 10.1001/archneurol.2011.636.
[27] L. B. Jardim, M. L. Pereira, I. Silveira, A. Ferro, J. Sequeiros, and R. Giugliani, “Neurologic Findings in Machado-Joseph Disease,” *Arch. Neurol.*, vol. 58, no. 6, p. 899, 2001, doi: 10.1001/archneur.58.6.899.
[28] L. Jardim *et al.*, “Searching for modulating effects of SCA2, SCA6 and DRPLA CAG tracts on the Machado-Joseph disease (SCA3) phenotype,” *Acta Neurol. Scand.*, vol. 107, no. 3, pp. 211–214, 2003, doi: 10.1034/j.1600-0404.2003.00046.x.
[29] N. Wan, Z. Chen, L. Wan, B. Tang, and H. Jiang, “MR Imaging of SCA3/MJD,” *Front. Neurosci.*, vol. 14, no. August, pp. 1–16, 2020, doi: 10.3389/fnins.2020.00749.
[30] C. Kieling, P. R. Prestes, M. L. Saraiva-Pereira, and L. B. Jardim, “Survival estimates for patients with Machado-Joseph disease (SCA3),” *Clin. Genet.*, vol. 72, no. 6, pp. 543–545, 2007, doi: 10.1111/j.1399-0004.2007.00910.x.
[31] D. R. Carvalho, A. La Rocque-Ferreira, I. M. Rizzo, E. U. Imamura, and C. E. Speck-Martins, “Homozygosity Enhances Severity in Spinocerebellar Ataxia Type 3,” *Pediatr. Neurol.*, vol. 38, no. 4, pp. 296–299, 2008, doi: 10.1016/j.pediatrneurol.2007.12.006.
[32] T. Klockgether *et al.*, “The natural history of degenerative ataxia: A retrospective study in 466 patients,” *Brain*, vol. 121, no. 4, pp. 589–600, 1998, doi: 10.1093/brain/121.4.589.
[33] H. L. Paulson, V. G. Shakkottai, H. B. Clark, and H. T. Orr, “Polyglutamine spinocerebellar ataxias-from genes to potential treatments,” *Nat. Rev. Neurosci.*, vol. 18, no. 10, pp. 613–626, 2017, doi: 10.1038/nrn.2017.92.
[34] H. T. Orr and H. Y. Zoghbi, “Trinucleotide repeat disorders,” *Annu. Rev. Neurosci.*, vol. 30, pp. 575–621, 2007, doi: 10.1146/annurev.neuro.29.051605.113042.
[35] H. Shanshan, Z. Suiqiang, L. Xiao-Jiang, and L. Shihua, “The Expanding Clinical Universe of Polyglutamine Disease,” *Neuroscientist*, vol. 176, no. 1, pp. 139–148, 2019, doi: 10.1177/1073858418822993.
[36] G. Nicastro, R. P. Menon, L. Masino, P. P. Knowles, N. Q. McDonald, and A. Pastore, “The solution structure of the Josephin domain of ataxin-3: Structural determinants for molecular recognition,” *Proc. Natl. Acad. Sci. U. S. A.*, vol. 102, no. 30, pp. 10493–10498, 2005, doi: 10.1073/pnas.0501732102.
[37] J. Goto *et al.*, “Machado-Joseph disease gene products carrying different carboxyl termini,” *Neurosci. Res.*, vol. 28, no. 4, pp. 373–377, 1997, doi: 10.1016/S0168-0102(97)00056-4.
[38] T. Schmidt *et al.*, “An isoform of ataxin-3 accumulates in the nucleus of neuronal cells in affected brain regions of SCA3 patients,” *Brain Pathol.*, vol. 8, no. 4, pp. 669–679, 1998, doi: 10.1111/j.1750-3639.1998.tb00193.x.
[39] A. Sicorello, G. Kelly, A. Oregioni, J. Nováček, V. Sklenář, and A. Pastore, “The Structural Properties in Solution of the Intrinsically Mixed Folded Protein Ataxin-3,” *Biophys. J.*, vol. 115, no. 1, pp. 59–71, 2018, doi: 10.1016/j.bpj.2018.05.029.
[40] A. X. Song *et al.*, “Structural transformation of the tandem ubiquitin-interacting motifs in ataxin-3 and their cooperative interactions with ubiquitin chains,” *PLoS One*, vol. 5, no. 10, 2010, doi: 10.1371/journal.pone.0013202.
[41] T. D. Grant *et al.*, “Small angle X-ray scattering as a complementary tool for high-throughput structural studies,” *Biopolymers*, vol. 95, no. 8, pp. 517–530, 2011, doi: 10.1002/bip.21630.
[42] M. Bonanomi *et al.*, “Interactions of ataxin-3 with its molecular partners in the protein machinery

that sorts protein aggregates to the aggresome," *Int. J. Biochem. Cell Biol.*, vol. 51, no. 1, pp. 58–64, 2014, doi: 10.1016/j.biocel.2014.03.015.
[43] M. G. G. Contessotto *et al.*, "The Machado-Joseph disease-associated expanded form of ataxin-3: Overexpression, purification, and preliminary biophysical and structural characterization," *Protein Expr. Purif.*, vol. 152, no. July, pp. 40–45, 2018, doi: 10.1016/j.pep.2018.07.005.
[44] P. M. A. Antony *et al.*, "Identification and functional dissection of localization signals within ataxin-3," *Neurobiol. Dis.*, vol. 36, no. 2, pp. 280–292, 2009, doi: 10.1016/j.nbd.2009.07.020.
[45] M. Albrecht, M. Golatta, U. Wüllner, and T. Lengauer, "Structural and functional analysis of ataxin-2 and ataxin-3," *Eur. J. Biochem.*, vol. 271, no. 15, pp. 3155–3170, 2004, doi: 10.1111/j.1432-1033.2004.04245.x.
[46] S. Macedo-Ribeiro, L. Cortes, P. Maciel, and A. L. Carvalho, "Nucleocytoplasmic shuttling activity of ataxin-3," *PLoS One*, vol. 4, no. 6, 2009, doi: 10.1371/journal.pone.0005834.
[47] D. Tait *et al.*, "Ataxin-3 is transported into the nucleus and associates with the nuclear matrix," *Hum. Mol. Genet.*, vol. 7, no. 6, pp. 991–997, 1998, doi: 10.1093/hmg/7.6.991.
[48] A. L. Lau, T. R. Kumar, K. Nishimori, J. Bonadio, and M. M. Matzuk, "Activin βC and βE Genes Are Not Essential for Mouse Liver Growth, Differentiation, and Regeneration," *Mol. Cell. Biol.*, vol. 20, no. 16, pp. 6127–6137, 2000, doi: 10.1128/mcb.20.16.6127-6137.2000.
[49] K. M. Scaglione *et al.*, "Ube2w and Ataxin-3 Coordinately Regulate the Ubiquitin Ligase CHIP," *Mol. Cell*, vol. 43, no. 4, pp. 599–612, 2011, doi: 10.1016/j.molcel.2011.05.036.
[50] A. Ciechanover and A. Hershko, "The ubiquitin system," *Annu. Rev. Biochem.*, vol. 458, no. 7237, p. 421, 1998, doi: 10.1038/458421a.
[51] M. Y. Sherman and A. L. Goldberg, "Cellular defenses against unfolded proteins: A cell biologist thinks about neurodegenerative diseases," *Neuron*, vol. 29, no. 1, pp. 15–32, 2001, doi: 10.1016/S0896-6273(01)00177-5.
[52] A. Ferro *et al.*, "NEDD8: A new ataxin-3 interactor," *Biochim. Biophys. Acta - Mol. Cell Res.*, vol. 1773, no. 11, pp. 1619–1627, 2007, doi: 10.1016/j.bbamcr.2007.07.012.
[53] N. R. Jana *et al.*, "Co-chaperone CHIP associates with expanded polyglutamine protein and promotes their degradation by proteasomes," *J. Biol. Chem.*, vol. 280, no. 12, pp. 11635–11640, 2005, doi: 10.1074/jbc.M412042200.
[54] A. Chatterjee *et al.*, "The Role of the Mammalian DNA End-processing Enzyme Polynucleotide Kinase 3'-Phosphatase in Spinocerebellar Ataxia Type 3 Pathogenesis," *PLoS Genet.*, vol. 11, no. 1, pp. 1–21, 2015, doi: 10.1371/journal.pgen.1004749.
[55] Y. Tu *et al.*, "Ataxin-3 promotes genome integrity by stabilizing Chk1," *Nucleic Acids Res.*, vol. 45, no. 8, pp. 4532–4549, 2017, doi: 10.1093/nar/gkx095.
[56] A. M. Ellisdon, M. C. Pearce, and S. P. Bottomley, "Mechanisms of Ataxin-3 Misfolding and Fibril Formation: Kinetic Analysis of a Disease-associated Polyglutamine Protein," *J. Mol. Biol.*, vol. 368, no. 2, pp. 595–605, 2007, doi: 10.1016/j.jmb.2007.02.058.
[57] A. M. Ellisdon, B. Thomas, and S. P. Bottomley, "The two-stage pathway of ataxin-3 fibrillogenesis involves a polyglutamine-independent step," *J. Biol. Chem.*, vol. 281, no. 25, pp. 16888–16896, 2006, doi: 10.1074/jbc.M601470200.
[58] H. M. Saunders, V. A. Hughes, R. Cappai, and S. P. Bottomley, "Conformational Behavior and Aggregation of Ataxin-3 in SDS," *PLoS One*, vol. 8, no. 7, pp. 1–10, 2013, doi: 10.1371/journal.pone.0069416.
[59] C. A. Scarff, B. Almeida, J. Fraga, S. Macedo-Ribeiro, S. E. Radford, and A. E. Ashcroft, "Examination of ataxin-3 (atx-3) aggregation by structural mass spectrometry techniques: A rationale for expedited aggregation upon polyglutamine (polyQ) expansion," *Mol. Cell. Proteomics*, vol. 14, no. 5, pp. 1241–1253, 2015, doi: 10.1074/mcp.M114.044610.
[60] L. Gales *et al.*, "Towards a structural understanding of the fibrillization pathway in Machado-Joseph's disease: Trapping early oligomers of non-expanded ataxin-3," *J. Mol. Biol.*, vol. 353, no. 3, pp. 642–654, 2005, doi: 10.1016/j.jmb.2005.08.061.
[61] P. Fernandez-Funez *et al.*, "Identification of genes that modify ataxin-1-induced neurodegeneration," *Nature*, vol. 408, no. 6808, pp. 101–106, 2000, doi: 10.1038/35040584.
[62] C. De Chiara, R. P. Menon, F. Dal Piaz, L. Calder, and A. Pastore, "Polyglutamine is not all: The functional role of the AXH domain in the ataxin-1 protein," *J. Mol. Biol.*, vol. 354, no. 4, pp. 883–893, 2005, doi: 10.1016/j.jmb.2005.09.083.
[63] L. Masino, G. Nicastro, R. P. Menon, F. D. Piaz, L. Calder, and A. Pastore, "Characterization of the structure and the amyloidogenic properties of the Josephin domain of the polyglutamine-

containing protein ataxin-3," *J. Mol. Biol.*, vol. 344, no. 4, pp. 1021–1035, 2004, doi: 10.1016/j.jmb.2004.09.065.
[64] A. Silva, B. Almeida, J. S. Fraga, P. Taboada, P. M. Martins, and S. Macedo-Ribeiro, "Distribution of Amyloid-Like and Oligomeric Species from Protein Aggregation Kinetics," *Angew. Chemie - Int. Ed.*, vol. 56, no. 45, pp. 14042–14045, 2017, doi: 10.1002/anie.201707345.
[65] A. Natalello *et al.*, "A major role for side-chain polyglutamine hydrogen bonding in irreversible ataxin-3 aggregation," *PLoS One*, vol. 6, no. 4, 2011, doi: 10.1371/journal.pone.0018789.
[66] A. E. Bevivino and P. J. Loll, "An expanded glutamine repeat destabilizes native ataxin-3 structure and mediates formation of parallel β-fibrils," *Proc. Natl. Acad. Sci. U. S. A.*, vol. 98, no. 21, pp. 11955–11960, 2001, doi: 10.1073/pnas.211305198.
[67] M. K. M. Chow, J. P. MacKay, J. C. Whisstock, M. J. Scanlon, and S. P. Bottomley, "Structural and functional analysis of the Josephin domain of the polyglutamine protein ataxin-3," *Biochem. Biophys. Res. Commun.*, vol. 322, no. 2, pp. 387–394, 2004, doi: 10.1016/j.bbrc.2004.07.131.
[68] A. P. Lieberman, V. G. Shakkottai, and R. L. Albin, "Polyglutamine Repeats in Neurodegenerative Diseases," *Annu. Rev. Pathol. Mech. Dis.*, vol. 14, no. July, pp. 1–27, 2019, doi: 10.1146/annurev-pathmechdis-012418-012857.
[69] J. M. Warrick *et al.*, "Ataxin-3 suppresses polyglutamine neurodegeneration in Drosophila by a ubiquitin-associated mechanism," *Mol. Cell*, vol. 18, no. 1, pp. 37–48, 2005, doi: 10.1016/j.molcel.2005.02.030.
[70] H. R. Brignull, F. E. Moore, S. J. Tang, and R. I. Morimoto, "Polyglutamine proteins at the pathogenic threshold display neuron-specific aggregation in a pan-neuronal Caenorhabditis elegans model," *J. Neurosci.*, vol. 26, no. 29, pp. 7597–7606, 2006, doi: 10.1523/JNEUROSCI.0990-06.2006.
[71] A. J. Williams and H. L. Paulson, "Polyglutamine neurodegeneration: protein misfolding revisited," *Trends Neurosci.*, vol. 31, no. 10, pp. 521–528, 2008, doi: 10.1016/j.tins.2008.07.004.
[72] U. Rüb *et al.*, "Spinocerebellar ataxia type 3 (SCA3): Thalamic neurodegeneration occurs independently from thalamic ataxin-3 immunopositive neuronal intranuclear inclusions," *Brain Pathol.*, vol. 16, no. 3, pp. 218–227, 2006, doi: 10.1111/j.1750-3639.2006.00022.x.
[73] M. Hsieh, H. F. Tsai, and W. H. Chang, "HSP27 and cell death in spinocerebellar ataxia type 3," *Cerebellum*, vol. 4, no. 1, pp. 31–36, 2005, doi: 10.1080/14734220410026248.
[74] P. Lajoie and E. L. Snapp, "Formation and toxicity of soluble polyglutamine oligomers in living cells," *PLoS One*, vol. 5, no. 12, 2010, doi: 10.1371/journal.pone.0015245.
[75] E. J. Slow *et al.*, "Absence of behavioral abnormalities and neurodegeneration in vivo despite widespread neuronal huntingtin inclusions," *Proc. Natl. Acad. Sci. U. S. A.*, vol. 102, no. 32, pp. 11402–11407, 2005, doi: 10.1073/pnas.0503634102.
[76] M. Arrasate, S. Mitra, E. S. Schweitzer, M. R. Segal, and S. Finkbeiner, "Inclusion body formation reduces levels of mutant huntingtin and the risk of neuronal death," *Nature*, vol. 431, no. 7010, pp. 805–810, 2004, doi: 10.1038/nature02998.
[77] M. Watanabe *et al.*, "Huntingin acts in," *Cell*, vol. 168, no. 1–2, pp. 295-310.e19, 2017.
[78] C. De Jonghe *et al.*, "Aberrant splicing in the presenilin-1 intron 4 mutation causes presenile Alzheimer's disease by increased Aβ42 secretion," *Hum. Mol. Genet.*, vol. 8, no. 8, pp. 1529–1540, 1999, doi: 10.1093/hmg/8.8.1529.
[79] L. Cartegni and A. R. Krainer, "Disruption of an SF2/ASF-dependent exonic splicing enhancer in SMN2 causes spinal muscular atrophy in the absence of SMN," *Nat. Genet.*, vol. 30, no. 4, pp. 377–384, 2002, doi: 10.1038/ng854.
[80] I. D'Souza *et al.*, "Missense and silent tau gene mutations cause frontotemporal dementia with parkinsonism-chromosome 17 type, by affecting multiple alternative RNA splicing regulatory elements," *Proc. Natl. Acad. Sci. U. S. A.*, vol. 96, no. 10, pp. 5598–5603, 1999, doi: 10.1073/pnas.96.10.5598.
[81] T. Takahashi, S. Kikuchi, S. Katada, Y. Nagai, M. Nishizawa, and O. Onodera, "Soluble polyglutamine oligomers formed prior to inclusion body formation are cytotoxic," *Hum. Mol. Genet.*, vol. 17, no. 3, pp. 345–356, 2008, doi: 10.1093/hmg/ddm311.
[82] P. Koch *et al.*, "Excitation-induced ataxin-3 aggregation in neurons from patients with Machado-Joseph disease," *Nature*, vol. 480, no. 7378, pp. 543–546, 2011, doi: 10.1038/nature10671.
[83] S. J. Shoesmith Berke, F. A. Flores Schmied, E. R. Brunt, L. M. Ellerby, and H. L. Paulson, "Caspase-mediated proteolysis of the polyglutamine disease protein ataxin-3," *J. Neurochem.*, vol. 89, no. 4, pp. 908–918, 2004, doi: 10.1111/j.1471-4159.2004.02369.x.

[84] A. Haacke, S. A. Broadley, R. Boteva, N. Tzvetkov, F. U. Hartl, and P. Breuer, “Proteolytic cleavage of polyglutamine-expanded ataxin-3 is critical for aggregation and sequestration of non-expanded ataxin-3,” *Hum. Mol. Genet.*, vol. 15, no. 4, pp. 555–568, 2006, doi: 10.1093/hmg/ddi472.

[85] J. Hübener *et al.*, “Calpain-mediated ataxin-3 cleavage in the molecular pathogenesis of spinocerebellar ataxia type 3 (SCA3),” *Hum. Mol. Genet.*, vol. 22, no. 3, pp. 508–518, 2013, doi: 10.1093/hmg/dds449.

[86] A. Teixeira-Castro *et al.*, “Neuron-specific proteotoxicity of mutant ataxin-3 in C. elegans: Rescue by the DAF-16 and HSF-1 pathways,” *Hum. Mol. Genet.*, vol. 20, no. 15, pp. 2996–3009, 2011, doi: 10.1093/hmg/ddr203.

[87] H. Ikeda, M. Yamaguchi, S. Sugai, Y. Aze, S. Narumiya, and A. Kakizuka, “Expanded polyglutamine in the machado-joseph disease protein induces cell death in vitro and in vivo,” *Nat. Genet.*, vol. 13, no. 2, pp. 196–202, 1996, doi: 10.1038/ng0696-196.

[88] D. Goti *et al.*, “A mutant ataxin-3 putative-cleavage fragment in brains of Machado-Joseph disease patients and transgenic mice is cytotoxic above a critical concentration,” *J. Neurosci.*, vol. 24, no. 45, pp. 10266–10279, 2004, doi: 10.1523/JNEUROSCI.2734-04.2004.

[89] M. J. Friedman *et al.*, “Polyglutamine domain modulates the TBP-TFIIB interaction: Implications for its normal function and neurodegeneration,” *Nat. Neurosci.*, vol. 10, no. 12, pp. 1519–1528, 2007, doi: 10.1038/nn2011.

[90] H. Adachi *et al.*, “CHIP overexpression reduces mutant androgen receptor protein and ameliorates phenotypes of the spinal and bulbar muscular atrophy transgenic mouse model,” *J. Neurosci.*, vol. 27, no. 19, pp. 5115–5126, 2007, doi: 10.1523/JNEUROSCI.1242-07.2007.

[91] L. B. Li, Z. Yu, X. Teng, and N. M. Bonini, “RNA toxicity is a component of ataxin-3 degeneration in Drosophila,” *Nature*, vol. 453, no. 7198, pp. 1107–1111, 2008, doi: 10.1038/nature06909.

[92] C. J. McLeod, L. V. O’Keefe, and R. I. Richards, “The pathogenic agent in Drosophila models of ‘polyglutamine’ diseases,” *Hum. Mol. Genet.*, vol. 14, no. 8, pp. 1041–1048, 2005, doi: 10.1093/hmg/ddi096.

[93] Y. C. Yu, C. L. Kuo, W. L. Cheng, C. S. Liu, and M. Hsieh, “Decreased antioxidant enzyme activity and increased mitochondrial DNA damage in cellular models of Machado-Joseph disease,” *J. Neurosci. Res.*, vol. 87, no. 8, pp. 1884–1891, 2009, doi: 10.1002/jnr.22011.

[94] N. Kazachkova *et al.*, “Patterns of mitochondrial DNA damage in blood and brain tissues of a transgenic mouse model of machado-joseph disease,” *Neurodegener. Dis.*, vol. 11, no. 4, pp. 206–214, 2013, doi: 10.1159/000339207.

[95] M. N. Laço, C. R. Oliveira, H. L. Paulson, and A. C. Rego, “Compromised mitochondrial complex II in models of Machado-Joseph disease,” *Biochim. Biophys. Acta - Mol. Basis Dis.*, vol. 1822, no. 2, pp. 139–149, 2012, doi: 10.1016/j.bbadis.2011.10.010.

[96] J. Emerit, M. Edeas, and F. Bricaire, “Neurodegenerative diseases and oxidative stress,” *Biomed. Pharmacother.*, vol. 58, no. 1, pp. 39–46, 2004, doi: 10.1016/j.biopha.2003.11.004.

[97] S. Muyldermans, “Nanobodies: Natural single-domain antibodies,” *Annu. Rev. Biochem.*, vol. 82, pp. 775–797, 2013, doi: 10.1146/annurev-biochem-063011-092449.

[98] C. Hamers-Casterman *et al.*, “Naturally occurring antibodies devoid of light chains,” *Nature*, vol. 363, no. 6428, pp. 446–448, 1993, doi: 10.1038/363446a0.

[99] M. M. Harmsen and H. J. De Haard, “Properties, production, and applications of camelid single-domain antibody fragments,” *Appl. Microbiol. Biotechnol.*, vol. 77, no. 1, pp. 13–22, 2007, doi: 10.1007/s00253-007-1142-2.

[100] R. J. Hoey, H. Eom, and J. R. Horn, “Structure and development of single domain antibodies as modules for therapeutics and diagnostics,” *Exp. Biol. Med.*, vol. 244, no. 17, pp. 1568–1576, 2019, doi: 10.1177/1535370219881129.

[101] V. K. Nguyen, R. Hamers, L. Wyns, and S. Muyldermans, “Camel heavy-chain antibodies: Diverse germline V(H)H and specific mechanisms enlarge the antigen-binding repertoire,” *EMBO J.*, vol. 19, no. 5, pp. 921–930, 2000, doi: 10.1093/emboj/19.5.921.

[102] J. Govaert *et al.*, “Dual beneficial effect of interloop disulfide bond for single domain antibody fragments,” *J. Biol. Chem.*, vol. 287, no. 3, pp. 1970–1979, 2012, doi: 10.1074/jbc.M111.242818.

[103] F. Koch-Nolte *et al.*, “ Single domain antibodies from llama effectively and specifically block T cell ecto-ADP-ribosyltransferase ART2.2 in vivo ,” *FASEB J.*, vol. 21, no. 13, pp. 3490–3498, 2007, doi: 10.1096/fj.07-8661com.

[104] R. Van Der Linden *et al.*, “Induction of immune responses and molecular cloning of the heavy

chain antibody repertoire of Lama glama," *J. Immunol. Methods*, vol. 240, no. 1–2, pp. 185–195, 2000, doi: 10.1016/S0022-1759(00)00188-5.
[105] M. Lauwereys *et al.*, "Potent enzyme inhibitors derived from dromedary heavy-chain antibodies," *EMBO J.*, vol. 17, no. 13, pp. 3512–3520, 1998, doi: 10.1093/emboj/17.13.3512.
[106] V. K. Nguyen, A. Desmyter, and S. Muyldermans, "Functional heavy-chain antibodies in Camelidae," *Adv. Immunol.*, vol. 79, pp. 261–296, 2001, doi: 10.1016/S0065-2776(01)79006-2.
[107] S. Muyldermans, "A guide to: generation and design of nanobodies," *FEBS J.*, vol. 288, no. 7, pp. 2084–2102, 2021, doi: 10.1111/febs.15515.
[108] S. Sidhu and C. Geyer, *Phage display in biotechnology and drug discovery*. CRC Press, Boca Raton, 2015.
[109] A. Frenzel, T. Schirrmann, and M. Hust, "Phage display-derived human antibodies in clinical development and therapy," *MAbs*, vol. 8, no. 7, pp. 1177–1194, 2016, doi: 10.1080/19420862.2016.1212149.
[110] B. N. Lim, C. F. Chin, Y. S. Choong, A. Ismail, and T. S. Lim, "Generation of a naïve human single chain variable fragment (scFv) library for the identification of monoclonal scFv against Salmonella Typhi Hemolysin e antigen," *Toxicon*, vol. 117, pp. 94–101, 2016, doi: 10.1016/j.toxicon.2016.04.032.
[111] D. Ponsel, J. Neugebauer, K. Ladetzki-Baehs, and K. Tissot, "High affinity, developability and functional size: The holy grail of combinatorial antibody library generation," *Molecules*, vol. 16, no. 5, pp. 3675–3700, 2011, doi: 10.3390/molecules16053675.
[112] S. Miersch and S. S. Sidhu, "Synthetic antibodies: Concepts, potential and practical considerations," *Methods*, vol. 57, no. 4, pp. 486–498, 2012, doi: 10.1016/j.ymeth.2012.06.012.
[113] A. Ismaili, M. Jalali-Javaran, M. J. Rasaee, F. Rahbarizadeh, M. Forouzandeh-Moghadam, and H. R. Memari, "Production and characterization of anti-(mucin MUC1) single-domain antibody in tobacco (Nicotiana tabacum cultivar Xanthi)," *Biotechnol. Appl. Biochem.*, vol. 47, no. 1, p. 11, 2007, doi: 10.1042/ba20060071.
[114] L. G. J. Frenken, J. G. M. Hessing, C. A. M. J. J. Van Den Hondel, and C. T. Verrips, "Recent advances in the large-scale production of antibody fragments using lower eukaryotic microorganisms," *Res. Immunol.*, vol. 149, no. 6, pp. 589–599, 1998, doi: 10.1016/S0923-2494(98)80011-4.
[115] L. G. J. Frenken *et al.*, "Isolation of antigen specific Llama V(HH) antibody fragments and their high level secretion by Saccharomyces cerevisiae," *J. Biotechnol.*, vol. 78, no. 1, pp. 11–21, 2000, doi: 10.1016/S0168-1656(99)00228-X.
[116] M. Arbabi-Ghahroudi, J. Tanha, and R. MacKenzie, "Prokaryotic expression of antibodies," *Cancer Metastasis Rev.*, vol. 24, no. 4, pp. 501–519, 2005, doi: 10.1007/s10555-005-6193-1.
[117] M. Graille *et al.*, "Crystal structure of a Staphylococcus aureus protein a domain complexed with the Fab fragment of a human IgM antibody: Structural basis for recognition of B-cell receptors and superantigen activity," *Proc. Natl. Acad. Sci. U. S. A.*, vol. 97, no. 10, pp. 5399–5404, 2000, doi: 10.1073/pnas.97.10.5399.
[118] V. Salema and L. Á. Fernández, "High yield purification of nanobodies from the periplasm of E. coli as fusions with the maltose binding protein," *Protein Expr. Purif.*, vol. 91, no. 1, pp. 42–48, 2013, doi: 10.1016/j.pep.2013.07.001.
[119] M. Dumoulin *et al.*, "Single-domain antibody fragments with high conformational stability," *Protein Sci.*, vol. 11, no. 3, pp. 500–515, 2009, doi: 10.1110/ps.34602.
[120] G. Hussack, T. Hirama, W. Ding, R. MacKenzie, and J. Tanha, "Engineered single-domain antibodies with high protease resistance and thermal stability," *PLoS One*, vol. 6, no. 11, 2011, doi: 10.1371/journal.pone.0028218.
[121] D. Saerens, K. Conrath, J. Govaert, and S. Muyldermans, "Disulfide Bond Introduction for General Stabilization of Immunoglobulin Heavy-Chain Variable Domains," *J. Mol. Biol.*, vol. 377, no. 2, pp. 478–488, 2008, doi: 10.1016/j.jmb.2008.01.022.
[122] Y. Hagihara, S. Mine, and K. Uegaki, "Stabilization of an immunoglobulin fold domain by an engineered disulfide bond at the buried hydrophobic region," *J. Biol. Chem.*, vol. 282, no. 50, pp. 36489–36495, 2007, doi: 10.1074/jbc.M707078200.
[123] M. M. Harmsen, C. B. Van Solt, A. M. Van Zijderveld-Van Bemmel, T. A. Niewold, and F. G. Van Zijderveld, "Selection and optimization of proteolytically stable llama single-domain antibody fragments for oral immunotherapy," *Appl. Microbiol. Biotechnol.*, vol. 72, no. 3, pp. 544–551, 2006, doi: 10.1007/s00253-005-0300-7.

[124] J. Davies and L. Riechmann, “Affinity improvement of single antibody VH domains: Residues in all three hypervariable regions affect antigen binding,” *Immunotechnology*, vol. 2, no. 3, pp. 169–179, 1996, doi: 10.1016/S1380-2933(96)00045-0.
[125] C. Zhou, S. Emadi, M. R. Sierks, and A. Messer, “A human single-chain Fv intrabody blocks aberrant cellular effects of overexpressed α-synuclein,” *Mol. Ther.*, vol. 10, no. 6, pp. 1023–1031, 2004, doi: 10.1016/j.ymthe.2004.08.019.
[126] A. Messer and J. McLear, “The therapeutic potential of intrabodies in neurologic disorders: Focus on huntington and Parkinson diseases,” *BioDrugs*, vol. 20, no. 6, pp. 327–333, 2006, doi: 10.2165/00063030-200620060-00002.
[127] A. Cardinale and S. Biocca, “The potential of intracellular antibodies for therapeutic targeting of protein-misfolding diseases,” *Trends Mol. Med.*, vol. 14, no. 9, pp. 373–380, 2008, doi: 10.1016/j.molmed.2008.07.004.
[128] A. Messer and D. C. Butler, “Optimizing intracellular antibodies (intrabodies/nanobodies) to treat neurodegenerative disorders,” *Neurobiol. Dis.*, vol. 134, no. July 2019, p. 104619, 2020, doi: 10.1016/j.nbd.2019.104619.
[129] M. Van Roy *et al.*, “The preclinical pharmacology of the high affinity anti-IL-6R Nanobody® ALX-0061 supports its clinical development in rheumatoid arthritis,” *Arthritis Res. Ther.*, vol. 17, no. 1, 2015, doi: 10.1186/s13075-015-0651-0.
[130] T. Chanier and P. Chames, “Nanobody Engineering: Toward Next Generation Immunotherapies and Immunoimaging of Cancer,” *Antibodies*, vol. 8, no. 1, p. 13, 2019, doi: 10.3390/antib8010013.
[131] C. Zhang, R. M. Ötjengerdes, J. Roewe, R. Mejias, and A. L. J. Marschall, “Applying Antibodies Inside Cells: Principles and Recent Advances in Neurobiology, Virology and Oncology,” *BioDrugs*, vol. 34, no. 4, pp. 435–462, 2020, doi: 10.1007/s40259-020-00419-w.
[132] Y. Duhoo *et al.*, “Camelid nanobodies used as crystallization chaperones for different constructs of PorM, a component of the type IX secretion system from Porphyromonas gingivalis,” *Acta Crystallogr. Sect. Struct. Biol. Commun.*, vol. 73, no. 5, pp. 286–293, 2017, doi: 10.1107/S2053230X17005969.
[133] D. Prole and C. Taylor, “A genetically-encoded toolkit of functionalized nanobodies against fluorescent proteins for visualizing and manipulating intracellular signalling,” *bioRxiv*, p. 544700, 2019, doi: 10.1101/544700.
[134] M. A. de Beer and B. N. G. Giepmans, “Nanobody-Based Probes for Subcellular Protein Identification and Visualization,” *Front. Cell. Neurosci.*, vol. 14, no. November, pp. 1–16, 2020, doi: 10.3389/fncel.2020.573278.
[135] C. Leow, K. Fischer, C. Leow, Q. Cheng, C. Chuah, and J. McCarthy, “Single Domain Antibodies as New Biomarker Detectors,” *Diagnostics*, vol. 7, no. 4, p. 52, 2017, doi: 10.3390/diagnostics7040052.
[136] I. Van Audenhove and J. Gettemans, “Nanobodies as Versatile Tools to Understand, Diagnose, Visualize and Treat Cancer,” *EBioMedicine*, vol. 8, pp. 40–48, 2016, doi: 10.1016/j.ebiom.2016.04.028.
[137] K. Buelens, G. Hassanzadeh-Ghassabeh, S. Muyldermans, A. Gils, and P. J. Declerck, “Generation and characterization of inhibitory nanobodies towards thrombin activatable fibrinolysis inhibitor,” *J. Thromb. Haemost.*, vol. 8, no. 6, pp. 1302–1312, 2010, doi: 10.1111/j.1538-7836.2010.03816.x.
[138] T. De Meyer, S. Muyldermans, and A. Depicker, “Nanobody-based products as research and diagnostic tools,” *Trends Biotechnol.*, vol. 32, no. 5, pp. 263–270, 2014, doi: 10.1016/j.tibtech.2014.03.001.
[139] L. Huang, S. Muyldermans, and D. Saerens, “Nanobodies®: Proficient tools in diagnostics,” *Expert Rev. Mol. Diagn.*, vol. 10, no. 6, pp. 777–785, 2010, doi: 10.1586/erm.10.62.
[140] Y. J. Yu and R. J. Watts, “Developing Therapeutic Antibodies for Neurodegenerative Disease,” *Neurotherapeutics*, vol. 10, no. 3, pp. 459–472, 2013, doi: 10.1007/s13311-013-0187-4.
[141] A. L. Southwell and P. H. Patterson, “Antibody therapy in neurodegenerative disease,” *Rev. Neurosci.*, vol. 21, no. 4, pp. 273–287, 2010, doi: 10.1515/REVNEURO.2010.21.4.273.
[142] M. Kijanka, B. Dorresteijn, S. Oliveira, and P. M. P. Van Bergen En Henegouwen, “Nanobody-based cancer therapy of solid tumors,” *Nanomedicine*, vol. 10, no. 1, pp. 161–174, 2015, doi: 10.2217/nnm.14.178.
[143] R. Chakravarty, S. Goel, and W. Cai, “Nanobody: The ‘magic bullet’ for molecular imaging?,”

Theranostics, vol. 4, no. 4, pp. 386–398, 2014, doi: 10.7150/thno.8006.
[144] A. L. Robertson, M. A. Bate, A. M. Buckle, and S. P. Bottomley, "The rate of polyQ-mediated aggregation is dramatically affected by the number and location of surrounding domains," *J. Mol. Biol.*, vol. 413, no. 4, pp. 879–887, 2011, doi: 10.1016/j.jmb.2011.09.014.
[145] S. Gupta, S. Jie, and D. W. Colby, "Protein misfolding detected early in pathogenesis of transgenic mouse model of huntington disease using amyloid seeding assay," *J. Biol. Chem.*, vol. 287, no. 13, pp. 9982–9989, 2012, doi: 10.1074/jbc.M111.305417.
[146] A. Khoshnan, J. Ko, and P. H. Patterson, "Effects of intracellular expression of anti-huntingtin antibodies of various specificities on mutant huntingtin aggregation and toxicity," *Proc. Natl. Acad. Sci. U. S. A.*, vol. 99, no. 2, pp. 1002–1007, 2002, doi: 10.1073/pnas.022631799.
[147] E. Kvam, B. L. Nannenga, M. S. Wang, Z. Jia, M. R. Sierks, and A. Messer, "Conformational targeting of fibrillar polyglutamine proteins in live cells escalates aggregation and cytotoxicity," *PLoS One*, vol. 4, no. 5, 2009, doi: 10.1371/journal.pone.0005727.
[148] A. Desmyter *et al.*, "Three camelid VHH domains in complex with porcine pancreatic α-amylase: Inhibition and versatility of binding topology," *J. Biol. Chem.*, vol. 277, no. 26, pp. 23645–23650, 2002, doi: 10.1074/jbc.M202327200.
[149] A. Desmyter, K. Decanniere, S. Muyldermans, and L. Wyns, "Antigen Specificity and High Affinity Binding Provided by One Single Loop of a Camel Single-domain Antibody," *J. Biol. Chem.*, vol. 276, no. 28, pp. 26285–26290, 2001, doi: 10.1074/jbc.M102107200.
[150] B. Traenkle, P. D. Kaiser, and U. Rothbauer, "Nanobody Platform for Determination of Protein Structure, Application of," *Encycl. Anal. Chem.*, pp. 1–14, 2016, doi: 10.1002/9780470027318.a9548.
[151] K. Decanniere, A. Desmyter, M. Lauwereys, M. A. Ghahroudi, S. Muyldermans, and L. Wyns, "A single-domain antibody fragment in complex with RNase A: Non-canonical loop structures and nanomolar affinity using two CDR loops," *Structure*, vol. 7, no. 4, pp. 361–370, 1999, doi: 10.1016/S0969-2126(99)80049-5.
[152] J. M. Thomas, "Centenary: The birth of X-ray crystallography," *Nature*, vol. 491, no. 7423, pp. 186–187, 2012, doi: 10.1038/491186a.
[153] A. McPherson, "A brief history of protein crystal growth," *J. Cryst. Growth*, vol. 110, no. 1–2, pp. 1–10, 1991, doi: 10.1016/0022-0248(91)90859-4.
[154] N. Asherie, "Protein crystallization and phase diagrams," *Methods*, vol. 34, no. 3, pp. 266–272, 2004, doi: 10.1016/j.ymeth.2004.03.028.
[155] R. Boistelle, J. P. Astier, G. Marchis-Mouren, V. Desseaux, and R. Haser, "Solubility, phase transition, kinetic ripening and growth rates of porcine pancreatic α-amylase isoenzymes," *J. Cryst. Growth*, vol. 123, no. 1–2, pp. 109–120, 1992, doi: 10.1016/0022-0248(92)90015-B.
[156] A. R. Feeling-Taylor, R. Michael Banish, R. E. Hirsch, and P. G. Vekilov, "Miniaturized scintillation technique for protein solubility determinations," *Rev. Sci. Instrum.*, vol. 70, no. 6, pp. 2845–2849, 1999, doi: 10.1063/1.1149805.
[157] N. E. Chayen and E. Saridakis, "Protein crystallization: From purified protein to diffraction-quality crystal," *Nat. Methods*, vol. 5, no. 2, pp. 147–153, 2008, doi: 10.1038/nmeth.f.203.
[158] G. Calero, A. E. Cohen, J. R. Luft, J. Newman, and E. H. Snell, "Identifying, studying and making good use of macromolecular crystals," *Acta Crystallogr. Sect. FStructural Biol. Commun.*, vol. 70, no. 8, pp. 993–1008, 2014, doi: 10.1107/S2053230X14016574.
[159] K. Raghunathan, P. T. Harris, and D. N. Arvidson, "Trial by fire: Are the crystals macromolecules?," *Acta Crystallogr. Sect. F Struct. Biol. Cryst. Commun.*, vol. 66, no. 5, pp. 615–620, 2010, doi: 10.1107/S1744309110012078.
[160] S. Mirza, Z. Akbar, and M. S. Ahmad, "A Simple Nondestructive, Cost-Effective Method for Differentiation of Protein Crystals from Salt Crystals by Using a Natural Dye," *Cryst. Growth Des.*, vol. 19, no. 7, pp. 3612–3615, 2019, doi: 10.1021/acs.cgd.9b00528.
[161] A. McPherson and B. Cudney, "Optimization of crystallization conditions for biological macromolecules," *Acta Crystallogr. Sect. FStructural Biol. Commun.*, vol. 70, pp. 1445–1467, 2014, doi: 10.1107/S2053230X14019670.
[162] A. Desmyter *et al.*, "Viral infection modulation and neutralization by camelid nanobodies," *Proc. Natl. Acad. Sci. U. S. A.*, vol. 110, no. 15, 2013, doi: 10.1073/pnas.1301336110.
[163] V. Tereshko, S. Uysal, A. Koide, K. Margalef, S. Koide, and A. A. Kossiakoff, " Toward chaperone-assisted crystallography: Protein engineering enhancement of crystal packing and X-ray phasing capabilities of a camelid single-domain antibody (V H H) scaffold ," *Protein Sci.*, vol. 17, no. 7,

pp. 1175–1187, 2008, doi: 10.1110/ps.034892.108.
[164] M. D. Adams *et al.*, "The genome sequence of Drosophila melanogaster," *Science (80-.).*, vol. 287, no. 5461, pp. 2185–2195, 2000, doi: 10.1126/science.287.5461.2185.
[165] H. Stocker and P. Gallant, "Getting started : an overview on raising and handling Drosophila.," *Methods Mol. Biol.*, vol. 420, pp. 27–44, 2008, doi: 10.1007/978-1-59745-583-1_2.
[166] B. H. Jennings, "Drosophila-a versatile model in biology & medicine," *Mater. Today*, vol. 14, no. 5, pp. 190–195, 2011, doi: 10.1016/S1369-7021(11)70113-4.
[167] M. D. Binder, "Encyclopedia of Neuroscience, Ten-Volume Set," 2009, [Online]. Available: http://books.google.com/books?id=9o4tcgAACAAJ&pgis=1.
[168] J. B. Duffy, "GAL4 system in Drosophila: A fly geneticist's Swiss army knife," *Genesis*, vol. 34, no. 1–2, pp. 1–15, 2002, doi: 10.1002/gene.10150.
[169] a H. Brand and N. Perrimon, "Targeted gene expression as a means of altering cell fates and generating dominant phenotypes," *Development*, vol. 118, no. 2, pp. 401–15, 1993.
[170] A. Spradling and G. Rubin, "Genetic Transformation of Drosophila with Transposable Element Vectors," *Science (80-.).*, vol. 218, no. 4570, pp. 341–347, 1982, [Online]. Available: http://www.ncbi.nlm.nih.gov/pubmed/6289435%0Ahttp://www.sciencemag.org/cgi/doi/10.1126/science.6289435.
[171] J. P. Wing *et al.*, "Drosophila Morgue is an F box/ubiquitin conjugase domain protein important for grim-reaper mediated apoptosis," *Nat. Cell Biol.*, vol. 4, no. 6, pp. 451–456, 2002, doi: 10.1038/ncb800.
[172] M. C. Ellis, E. M. O'Neill, and G. M. Rubin, "Expression of Drosophila glass protein and evidence for negative regulation of its activity in non-neuronal cells by another DNA-binding protein," *Development*, vol. 119, no. 3, pp. 855–865, 1993, doi: 10.1242/dev.119.3.855.
[173] K. M. Yao and K. White, "Neural specificity of elav expression: Defining a Drosophila promoter for directing expression to the nervous system," *J. Neurochem.*, vol. 63, no. 1, pp. 41–51, 1994, doi: 10.1046/j.1471-4159.1994.63010041.x.
[174] S. Casas-tintó, M. Arnés, and S. Casas-tintó, "Drosophila enhancer-Gal4 lines show ectopic expression during development Subject Category : Subject Areas : Author for correspondence :," *R. Soc. Publ.*, vol. 4, p. 170039, 2017.
[175] S. Robinow and K. White, "Characterization and spatial distribution of the ELAV protein during Drosophila melanogaster development," *J. Neurobiol.*, vol. 22, no. 5, pp. 443–461, 1991, doi: 10.1002/neu.480220503.
[176] S. E. McGuire, G. Roman, and R. L. Davis, "Gene expression systems in Drosophila: A synthesis of time and space," *Trends Genet.*, vol. 20, no. 8, pp. 384–391, 2004, doi: 10.1016/j.tig.2004.06.012.
[177] J. Bilen and N. M. Bonini, "Drosophila as a model for human neurodegenerative disease," *Annu. Rev. Genet.*, vol. 39, pp. 153–171, 2005, doi: 10.1146/annurev.genet.39.110304.095804.
[178] K. Iijima-Ando, P. Wu, E. A. Drier, K. Iijima, and J. C. P. Yin, "cAMP-response element-binding protein and heat-shock protein 70 additively suppress polyglutamine-mediated toxicity in Drosophila," *Proc. Natl. Acad. Sci. U. S. A.*, vol. 102, no. 29, pp. 10261–10266, 2005, doi: 10.1073/pnas.0503937102.
[179] J. L. Marsh *et al.*, "Expanded polyglutamine peptides alone are intrinsically cytotoxic and cause neurodegeneration in Drosophila," *Hum. Mol. Genet.*, vol. 9, no. 1, pp. 13–25, 2000, doi: 10.1093/hmg/9.1.13.
[180] J. P. Taylor, A. A. Taye, C. Campbell, P. Kazemi-Esfarjani, K. H. Fischbeck, and K. T. Min, "Aberrant histone acetylation, altered transcription, and retinal degeneration in a Drosophila model of polyglutamine disease are rescued by CREB-binding protein," *Genes Dev.*, vol. 17, no. 12, pp. 1463–1468, 2003, doi: 10.1101/gad.1087503.
[181] G. R. Jackson *et al.*, "Polyglutamine-expanded human huntingtin transgenes induce degeneration of Drosophila photoreceptor neurons," *Neuron*, vol. 21, no. 3, pp. 633–642, 1998, doi: 10.1016/S0896-6273(00)80573-5.
[182] P. Kazemi-Esfarjani and S. Benzer, "Genetic suppression of polyglutamine toxicity in Drosophila," *Science (80-.).*, vol. 287, no. 5459, pp. 1837–1840, 2000, doi: 10.1126/science.287.5459.1837.
[183] Z. Long, B. Tang, and H. Jiang, "Alleviating neurodegeneration in Drosophila models of PolyQ diseases," *Cerebellum and Ataxias*, vol. 1, no. 1, pp. 1–10, 2014, doi: 10.1186/2053-8871-1-9.
[184] M. Cushman-Nick, N. M. Bonini, and J. Shorter, "Hsp104 Suppresses Polyglutamine-Induced

Degeneration Post Onset in a Drosophila MJD/SCA3 Model," *PLoS Genet.*, vol. 9, no. 9, 2013, doi: 10.1371/journal.pgen.1003781.
[185] Y. Nagai *et al.*, "Prevention of polyglutamine oligomerization and neurodegeneration by the peptide inhibitor QBP1 in Drosophila," *Hum. Mol. Genet.*, vol. 12, no. 11, pp. 1253–1260, 2003, doi: 10.1093/hmg/ddg144.
[186] D. E. Garfin, "One-dimensional gel electrophoresis," *Methods Enzymol.*, vol. 182, no. C, pp. 425–441, 1990, doi: 10.1016/0076-6879(90)82035-Z.
[187] H. Naiki *et al.*, "Methods in laboratory investigation. Fluorometric examination of tissue amyloid fibrils in murine senile amyloidosis: Use of the fluorescent indicator, Thioflavine T," *Lab. Investig.*, vol. 62, no. 6, pp. 768–773, 1990.
[188] C. Xue, T. Y. Lin, D. Chang, and Z. Guo, "Thioflavin T as an amyloid dye: Fibril quantification, optimal concentration and effect on aggregation," *R. Soc. Open Sci.*, vol. 4, no. 1, 2017, doi: 10.1098/rsos.160696.
[189] E. Head *et al.*, "Rabbit Anti- Amyloid Oligomer Polyclonal Antibody," *Trends Biochem. Sci.*, vol. 1, no. 800, pp. 2004–2007, 2006.
[190] M. S. Celej, R. Sarroukh, E. Goormaghtigh, G. D. Fidelio, J. M. Ruysschaert, and V. Raussens, "Toxic prefibrillar α-synuclein amyloid oligomers adopt a distinctive antiparallel β-sheet structure," *Biochem. J.*, vol. 443, no. 3, pp. 719–726, 2012, doi: 10.1042/BJ20111924.
[191] E. Scherzinger *et al.*, "Self-assembly of polyglutamine-containing huntingtin fragments into amyloid-like fibrils: Implications for Huntington's disease pathology (huntingtinglutamine repeataggregation)," *Med. Sci. Commun. by Max F. Perutz, Med. Res. Counc.*, vol. 96, no. April, pp. 4604–4609, 1999, [Online]. Available: www.pnas.org.
[192] J. Page *et al.*, "Comparison of geldanamycin (NSC-122750) and 17-allylaminogeldanamycin (NSC-330507) toxicity in rats," *Proc. Am. Assoc. Cancer Res.*, vol. 38, p. 308, 1997.
[193] H. B. Bohidar, "Physics of Proteins," *Fundam. Polym. Phys. Mol. Biophys.*, pp. 231–271, 2014, doi: 10.1017/cbo9781107415959.015.
[194] Ł. Mielańczyk, N. Matysiak, O. Klymenko, and R. Wojnicz, "Transmission Electron Microscopy of Biological Samples," *Transm. Electron Microsc. - Theory Appl.*, 2015, doi: 10.5772/60680.
[195] M. Rames, Y. Yu, and G. Ren, "Optimized negative staining: A high-throughput protocol for examining small and asymmetric protein structure by electron microscopy," *J. Vis. Exp.*, no. 90, 2014, doi: 10.3791/51087.
[196] "Ligation Calculator." http://www.insilico.uni-duesseldorf.de/Lig_Input.html.
[197] M. Biancalana and S. Koide, "Molecular mechanism of Thioflavin-T binding to amyloid fibrils," *Biochim. Biophys. Acta - Proteins Proteomics*, vol. 1804, no. 7, pp. 1405–1412, Jul. 2010, doi: 10.1016/j.bbapap.2010.04.001.
[198] P. Arosio, T. P. J. Knowles, and S. Linse, "On the lag phase in amyloid fibril formation," *Phys. Chem. Chem. Phys.*, vol. 17, no. 12, pp. 7606–7618, 2015, doi: 10.1039/c4cp05563b.
[199] O. Sin *et al.*, "Identification of an RNA Polymerase III Regulator Linked to Disease-Associated Protein Aggregation," *Mol. Cell*, vol. 65, no. 6, pp. 1096-1108.e6, 2017, doi: 10.1016/j.molcel.2017.02.022.
[200] S. L. Johnson *et al.*, "Differential toxicity of ataxin-3 isoforms in Drosophila models of Spinocerebellar Ataxia Type 3," *Neurobiol. Dis.*, vol. 132, no. July, p. 104535, 2019, doi: 10.1016/j.nbd.2019.104535.
[201] A. A. Burr, W. L. Tsou, G. Ristic, and S. V. Todi, "Using membrane-targeted green fluorescent protein to monitor neurotoxic protein-dependent degeneration of Drosophila eyes," *J. Neurosci. Res.*, vol. 92, no. 9, pp. 1100–1109, 2014, doi: 10.1002/jnr.23395.
[202] W. L. Tsou, A. A. Burr, M. Ouyang, J. R. Blount, K. M. Scaglione, and S. V. Todi, "Ubiquitination regulates the neuroprotective function of the deubiquitinase ataxin-3 in vivo," *J. Biol. Chem.*, vol. 288, no. 48, pp. 34460–34469, 2013, doi: 10.1074/jbc.M113.513903.
[203] W. L. Tsou *et al.*, "The deubiquitinase ataxin-3 requires Rad23 and DnaJ-1 for its neuroprotective role in Drosophila melanogaster," *Neurobiol. Dis.*, vol. 82, pp. 12–21, 2015, doi: 10.1016/j.nbd.2015.05.010.